Institut für Physik

Titel der Dissertation

High-latitude coupling processes between thermospheric circulation and solar wind driven magnetospheric currents and plasma convection

Dissertation
zur Erlangung des akademischen Grades
"doctor rerum naturalium"
(Dr. rer. nat.)
in der Wissenschaftsdisziplin " Physik"

eingereicht an der
Mathematisch-Naturwissenschaftlichen Fakultät
der Universität Potsdam

von
Boris E. Prokhorov

Potsdam
November 2015

Supervisors:

      Prof. Dr. Matthias Holschneider
         Dr. Matthias Förster
      Prof. Dr. Alexander A. Namgaladze

Reviewers:

      Prof. Dr. Christoph Jacobi
      Prof. Dr. Jorge L. Chau

Zusammenfassung

Die thermosphärischen Prozesse in hohen Breiten, die durch die Wechselwirkung des Sonnenwinds und des Interplanetaren Magnetfeldes (IMF) mit der Erdmagnetosphäre getrieben werden, stellen sich als stark veränderliches Geschehen in der komplexen dynamischen Plasmaumgebung der Erde dar, die das gekoppelte System der Magnetosphäre, Ionosphäre und Thermosphäre (MIT) umfaßt. Die Einflüsse des Sonnenwindes und des IMF zeigen sich als Energieübertragung in das MIT System mittels Rekonnektionsprozessen an der Magnetopause. Feldliniengerichtete Ströme (FACs) repräsentieren die energetische Kopplung zwischen der Magnetosphäre und der Ionosphäre der Erde. Das MIT System wird bestimmt durch die stark veränderlichen Sonnenwindbedingungen, insbesondere von der Stärke und Richtung des IMF.

In meiner Promotionsschrift untersuche ich die physikalischen Bedingungen des komplexen MIT System mit Hilfe eines globalen physikalisch-numerischen, dreidimensionalen, zeitabhängigen und selbstkonsistenten Modells, dem Upper Atmosphere Model (UAM). Das UAM beschreibt das Verhalten der Thermosphäre, Ionosphäre, Plasmasphäre und der inneren Magnetosphäre in einem Höhenbereich zwischen 80 (60) km und 15 Erdradien sowie die elektrodynamische Verkopplung des gesamten MIT Systems.

In der vorliegenden Arbeit habe ich mehrere Varianten der elektrodynamischen Kopplung in hohen Breiten entwickelt und analysiert, die die FACs innerhalb des UAM in ihrer Abhängigkeit vom IMF darstellen. Für Testzwecke wurden diese Varianten auf eine Reihe von numerischen Simulationen des gekoppelten MIT Systems unter verschiedenen Bedingungen hinsichtlich Jahreszeit, geomagnetischer Aktivität, Sonnenwind- und IMF-Parametern angewandt. Darüberhinaus wurden diese Varianten des IMF-abhängigen theoretischen Modells entsprechenden globalen empirischen Modellen gegenübergestellt. Modellergebnisse wurden außerdem mit einigen wichtigen von Satelliten gemessenen Thermosphärenparametern, wie dem Neutralwind und der Massendichte verglichen. Die UAM Modelvarianten mit IMF-Abhängigkeit zeigen eine gute Übereinstimmung mit den Satellitenbeobachtungen. Im Vergleich mit empirischen Modellaussagen geben die UAM Modellvarianten ein genaueres Bild der mesoskaligen Strukturen und der Dynamik des gekoppelten MIT Systems wieder, insbesondere für die hohen Breiten. Die neuen UAM Konfigurationen mit IMF-Abhängigkeit tragen damit zu verbesserten Möglichkeiten in der Weltraumwettervorhersage bei.

Abstract

The high-latitudinal thermospheric processes driven by the solar wind and Interplanetary Magnetic Field (IMF) interaction with the Earth magnetosphere are highly variable parts of the complex dynamic plasma environment, which represent the coupled Magnetosphere – Ionosphere – Thermosphere (MIT) system. The solar wind and IMF interactions transfer energy to the MIT system via reconnection processes at the magnetopause. The Field Aligned Currents (FACs) constitute the energetic links between the magnetosphere and the Earth ionosphere. The MIT system depends on the highly variable solar wind conditions, in particular on changes of the strength and orientation of the IMF.

In my thesis, I perform an investigation on the physical background of the complex MIT system using the global physical - numerical, three-dimensional, time-dependent and self-consistent Upper Atmosphere Model (UAM). This model describes the thermosphere, ionosphere, plasmasphere and inner magnetosphere as well as the electrodynamics of the coupled MIT system for the altitudinal range from 80 (60) km up to the 15 Earth radii.

In the present study, I developed and investigated several variants of the high-latitudinal electrodynamic coupling by including the IMF dependence of FACs into the UAM model. For testing, the various variants were applied to simulations of the coupled MIT system for different seasons, geomagnetic activities, various solar wind and IMF conditions. Additionally, these variants of the theoretical model with the IMF dependence were compared with global empirical models. The modelling results for the most important thermospheric parameters like neutral wind and mass density were compared with satellite measurements. The variants of the UAM model with IMF dependence show a good agreement with the satellite observations. In comparison with the empirical models, the improved variants of the UAM model reproduce a more realistic meso-scale structures and dynamics of the coupled MIT system than the empirical models, in particular at high latitudes. The new configurations of the UAM model with IMF dependence contribute to the improvement of space weather prediction.

Content

Introduction

The modern high technological civilization is increasingly involving the near-Earth environment in our everyday lives. It is used in numerous ways ranging from satellite communication and global positioning systems to satellite monitoring of the ecological situation on Earth's surface and weather prediction. For a successful expansion into the near-Earth space environment, people should develop technology in parallel with the investigations of the structures, physical background and responses of Earth's environment to inner and outer influences. The deeper understanding of the physical processes in the complex and highly coupled near Earth's space system is, therefore, a fundamental problem in modern physics *[Eastwood, 2008]*.

Over fifty years since the beginning of the satellite era, a huge amount of satellite measurements of different physical parameters have been collected. These data complement the ground-based observations. The analysis of all these collected data allowed researchers to reconstruct the structure of Earth's environment and to describe the processes in it. However, these measurements needed for the comprehensive description of the complex near Earth's environment have a significant disadvantage. The observations do not represent the complex Earth's environment globally for instant of time. Moreover, they provide limited information about physical parameters. For example, a satellite provides only the information about the environment close to the spacecraft for each moment. Ground-based measurements, on the other hand, are also restricted by the position of the station.

At the same time, the systematization of the measurements and information about the near-Earth space also allowed researchers to obtain empirical models, such as the Horizontal Wind Model 2007 (HWM07) *[Drob et al. 2008]* and Naval Research Laboratory Mass Spectrometer and Incoherent Scatter Extended 2000 model (NRLMSISE00) *[Picone et al., 2002]*. These models represent the global distribution of ionospheric and thermospheric parameters (horizontal thermospheric wind fields (HWM07); the temperature and density of the basic constituents of the neutral atmosphere), but not the whole Earth's environment as coupled system. In addition, the empirical models do not so well reproduce the dynamics of such highly variable areas as, for example in the high latitudinal region. They efficiently describe the general behavior, but do not enable predictions of meso-scale structures as well as all rapid changes during dynamic situations. They do not provide much information about the physical parameters and the coupling processes because of their characters shuch as average, empirical description of specific part of Earth's environment.

A relatively new way of research the near-Earth space is the use of physical-theoretical global simulation. Using first-principal physical equations, researchers can describe Earth's environment as a complex dynamical coupled system. Together with observations, the theoretical first-principal physical description can be used as a very powerful instrument for deeper investigations of the near-Earth space and nature in general.

The aim of my thesis is to investigat the Magnetosphere – Ionosphere – Thermosphere (MIT) dynamic coupling system. This system is part of the complex Earth environment. The MIT system is affected by inner and outer driving forces. The outer influence could be characterized by the highly variable solar wind conditions, in particular by changes in the strength and orientation of the Interplanetary Magnetic Field (IMF). The solar wind and IMF interactions transfer energy to the MIT system via magnetospheric Field Aligned Currents (FACs). Together with it, the IMF forms the asymmetric high-latitude magnetospheric/ionospheric electric field distribution in the Northern and Southern Hemispheres *[Haaland et al. 2007]*.

For my investigation, I make use of the global physical, three-dimensional, time-dependent and self-consistent Upper Atmosphere Model (UAM) *[Namgaladze et al., 1988, 1990, 1991, 1994, 1995a, 1995b; Volkov and Namgaladze, 1996; Hall et al., 1997]*. The UAM model describes the near-Earth space environment as well as the electrodynamics of this coupled system for the altitudinal range from 80 km up to the 15 Earth radius.

For the deeper understanding of the physical background and for the prediction of the MIT dynamic coupling system responses on various solar wind/IMF conditions, I further developed the UAM model by improving its performance at high latitudes. This concerns, in particular, the adaption of the IMF dependent electrodynamics *[Förster et al. 2011b; Förster et al. 2012; Namgaladze et al. 2013; Prokhorov et al., 2014]*.

In my thesis, I present three IMF dependent variants of the UAM model as follows:

The first variant is the model with modified electric field distribution. For this version of the UAM model, an adapted pre-calculated electric field distribution was as input parameter. The electric field was modified with respect to the B_Y component of the IMF. I simulated a twisting of the electric field inside the polar latitudes in the opposite directions for the Northern and Southern Hemispheres.

The second variant is the UAM model with the IMF dependent FAC distribution as input parameter. For this version, the FAC patterns for the Northern and Southern polar areas were specified using an empirical IMF dependent FAC model. I used the empirical model of *Papitashvili et al. [2002]* for this task. The obtained FAC distributions were adapted for the UAM model. The FAC patterns were presented as system of Region 1, 2 and 0 currents for the Northern and Southern Hemispheres. Such FAC configuration provided the required modifications in the electric field distributions with respect to the strength and orientation of the IMF.

The third variant of the model was obtained by including the empirical high-resolution IMF dependent FAC model of *He et al. [2012]* (MFACE) to the UAM model. In this version of the UAM model, the two dimensional FAC distributions for the Northern and Southern Hemispheres were defined by the MFACE model. This empirical model was used to specify the position of the auroral precipitation area. Using this model as part of the UAM model, the IMF dependent electric field distribution was reproduced with respect to the B_Y and B_Z components of the IMF, solar wind velocity, season, and magnetic activity.

I tested the first variant of the UAM model by simulating the time interval of October 28, 2003, 00 – 24 UT (this interval contains a time period with a relatively "stable" IMF B_Y component). The simulation results (with/without the dependence of the IMF) for the thermospheric neutral wind data were compared with the CHAllenging Minisatellite Payload (CHAMP) accelerometer measurements. Using the modified electric field, I could significantly improve the agreement between the UAM modeling data and the CHAMP satellite observations.

To test the second and third variants of the UAM model, I performed a simulation of the MIT dynamic coupling system for various intervals which representet for different seasons, geomagnetic and solar wind/IMF conditions. The obtained results for the thermospheric neutral wind, neutral mass density and electron density were compared with the CHAMP satellite measurements and global empirical models.

Additionally, I completed a statistical study where different variants of the UAM model were compared with the CHAMP observations and the empirical models. The comparison showed that all variants of the UAM model could reproduce the meso-scale structures of the satellite measurements more realistically in comparison with the empirical models. In addition, the statistical characteristics of the models could be investigated in more detail.

Chapter 1 provides short information about the UAM model. In this chapter, I provide a brief description of the structure of the model (four blocks plus the equation systems), input/output parameters, start conditions, coordinate systems and spatial resolution. The material of this chapter was partially presented in *Namgaladze et al. 2013*.

Chapter 2 presents the algorithm of the electric field calculation using a symmetrical distribution of the Field-Aligned Current (FAC) for the Northern and Southern Hemispheres *[Iijima and Potemra 1976]*. Together with it, I describe the improvement of the UAM model by including the IMF dependence via the modification of the electric field. The simulations with the modified version of the UAM model for October 28, 2003 were compared with the CHAMP satellite data. The material of this chapter was partially published by *Förster et al. 2011b and Namgaladze et al. 2013*.

In Chapter 3, I describe the method which allows the use of any FAC distribution as input parameter for the UAM model. This was done for the first time for the UAM model. Using this method, I incorporated an empirical IMF dependent FAC model *[Papitashvili et al. 2002]* to the UAM model. The IMF dependent version of the UAM model was tested for various solar wind/IMF conditions. The simulation results for the thermospheric neutral wind, neutral mass density, and electron density were compared with the CHAMP measurements. The material of this chapter was partially published by *Förster et al. [2012], Namgaladze et al. [2013]*, and *Prokhorov et al., [2014]*.

Chapter 4 presents the high-resolution empirical MFACE model and a detailed description of the method how to adapt the MFACE model *[He et al. 2012]* for the UAM model. This was the first time that I used the two dimensional high-resolution distribution of the FAC as input parameter for the UAM model. The new modification of the UAM model was tested for various geomagnetic conditions. The obtained modeling results for the thermospheric neutral wind and neutral mass density were compared with the CHAMP accelerometer measurements and empirical models. The material of this chapter was partially published by *Prokhorov et al., 2014*.

In Chapter 5, I perform a statistical comparison of the thermospheric neutral wind calculated by the various modifications of the UAM model with the CHAMP cross-track wind measurements and the global thermospheric wind model (HWM07). In addition, I compare the neutral mass density results with the corresponding CHAMP accelerometer data and the global empirical atmosphere density model (NRLMSISE00).

1. The Upper Atmosphere Model (UAM)

1.1. Introduction

The material of this chapter was partially presented in ***Namgaladze et al. 2013***. The equations and their descriptions are directly taken from this publication.

The global physical UAM model was developed for more than 30 years. The first comprehensive model description can be found in ***Namgaladze et al. [1988]***. Later reviews of further development of the model with further sophistication and application to various tasks were published in ***Namgaladze et al., [1991, 1994, 1995a, 1995b, 2013]***. I will not repeat all the details of the UAM model formulations here. However, for a better comprehensibility of the background of the model, I present a brief UAM model description. I provide a short information about the UAM model structure (four blocks together with the equation systems), input/output parameters, start conditions, coordinate systems and spatial resolution. The detailed descriptions of the blocks and equations can be found in ***Namgaladze et al. [1988]*** and ***Brunelli and Namgaladze [1988]***.

1.2. The UAM model

The UAM is a global physical, three-dimensional, time-dependent and self-consistent model. It represents the Earth's upper atmosphere in the altitude ranging from 80 km (60 km for some versions) up to 15 Earth radii of geocentric distance. The model was constructed at the Kaliningrad Observatory which is now the West Department of the Institute of Terrestrial Magnetism, Ionosphere and Radiowave Propagation of the Russian Academy of Sciences (IZMIRAN) ***[Namgaladze et al., 1988, 1990, 1991, 1994]***. Furthermore, the UAM model was developed at the Polar Geophysical Institute and at Murmansk State Technical University ***[Namgaladze et al., 1995a, 1995b; Volkov and Namgaladze, 1996; Hall et al., 1997]***.

The UAM model includes the thermosphere, ionosphere, plasmasphere and inner magnetosphere as well as the electrodynamics of the MIT coupled system. The model describes the Earth's environment by means of numerical integration of the system of equations of continuity, momentum and heat balances for neutral gas composition, electron and ions, together with the equation for electric field potential.
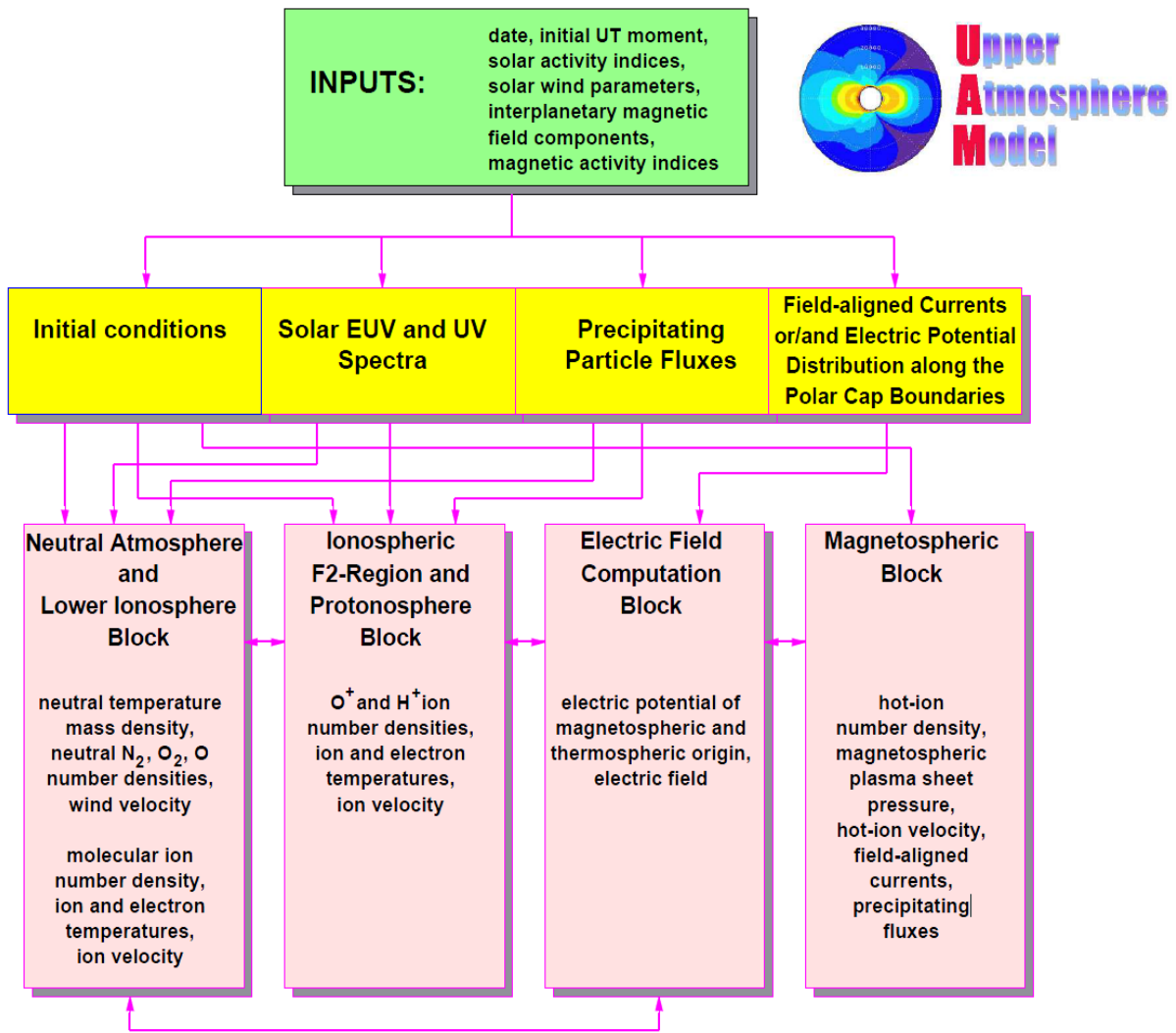
Figure 1.1. *The schematic structure of the UAM model with its inputs (initial and boundary conditions), the four main computational blocks, and their output parameters* **[Förster et al., 1999]**.

The structure of the UAM model, which is shown in Figure 1.1, can be divided into four main blocks:

1. The neutral atmosphere and lower ionosphere block. The altitude range is from 80 (60) up to 526 km. The calculated parameters are the temperature, densities and wind velocity of neutral atmosphere as well as electron and ion temperatures, density and velocity.

2. The ionospheric F2-region and protonospheric block. The altitude range is from 175 km up to 15 Earth radii of geocentric distance. The calculated parameters are the densities, temperatures and velocities of atomic ions O^+ and H^+ and electron temperature.

3. The electric field block. The altitude range is the same as that of Block 2. The calculated parameters is the global Earth's electric field.

4. The magnetospheric block. The altitude range is the same as that of Blocks 2 and 3. The calculated parameters comprise the magnetospheric plasma sheet density, ion density, its pressure, velocity and field aligned currents.

The hydrodynamic equation systems of the UAM model are solved numerically using finite-difference methods in the nodes of the spatial grid. The model uses a geomagnetic spherical coordinate system for Block 1 and geomagnetic dipole coordinates for Blocks 2, 3 and 4 *[Namgaladze et al. 2013]*.

1.3. The neutral atmosphere and low ionosphere block

1.3.1. Neutral atmosphere

This section of the UAM model offers the three-dimensional distributions of the neutral atmosphere parameters including the neutral gas temperature T_n, the neutral mass density ρ, the thermospheric wind velocity vector V and the mass density of the main neutral gas components N_2, O_2, and O. These parameters are calculated globally for an altitude range from 80 (60) to 526 km using a spherical geomagnetic coordinate system. The UAM model provides the neutral atmosphere parameters by solving the full system of the continuity (Equations 1.1 and 1.4), momentum (Equation 1.2), and energy balance equations (Equation 1.7) for the neutral gases (see below). This hydrodynamic equation system is solved in a fully self-consistent way. Apart from this, there is a possibility to alternatively use one or more of these parameters which can be obtained from such global empirical thermospheric models, as the MSISE-90 *[Hedin et al. 1991]* or its later modified version NRLMSISE-00 *[Picone et al. 2002]*. These models are included into the UAM model as an option.

$$\partial n_n / \partial t + \nabla[\ n_n(V + V_{dn})\ ] = Q_n - L_n \ , \tag{1.1}$$

$$\rho[\ \partial V / \partial t + (V, \nabla)V + 2\Omega \times V\ ]_{hor} = - (\nabla p)_{hor} - \sum_i \sum_n \mu_{ni}\ \nu_{ni}\ n_n\ (V - V_i)_{hor} + \eta\ (\nabla^2 V)_{hor}\ , \tag{1.2}$$

$$\rho\ g = - \partial p / \partial r \ , \tag{1.3}$$

$$\partial \rho / \partial t + \nabla(\rho V) = 0 \ , \tag{1.4}$$

$$\rho = \sum_n n_n\ m_n \ , \tag{1.5}$$

$$p = \sum_n n_n\ kT \ , \tag{1.6}$$

$$\rho\ c_v\ [\ \partial T / \partial t + (V, \nabla)T\ ] + p\ \nabla V = \nabla(\lambda_n \nabla T) + P_{nQ}{}^{UV} + P_{nQ}{}^{J} + P_{nQ}{}^{C} - P_{nL} \ . \tag{1.7}$$

In this equation system n_n is the concentration of the n-th neutral component; V is the neutral wind velocity vector; V_{dn} is the diffusion velocity vector which has only a vertical component equal to the sum of molecular and eddy diffusion velocities; Q_n, L_n are the production and loss rates of the n-th neutral component taking into account the dissociation of O_2 and the reactions of recombination for O and O_2; the index "*hor*" stands for horizontal vector components; ρ, p are the mean mass density and pressure of the neutral gas; Ω is the Earth's angular velocity vector; μ_{ni}, v_{ni} are the reduced mass and frequency of collisions between the neutral and ion components of the atmosphere; V_i is the ion velocity vector; η is the coefficient of viscosity; g is the sum of gravity and centrifugal accelerations; r is the geocentric distance; m_n is the mass of the n-th neutral component; k is the Boltzmann's constant; T is the temperature of the neutral gas; c_v is the specific heat at constant volume; λ_n is the thermal conductivity coefficient of the neutral gas; P_{nQ}^{UV}, P_{nQ}^{J}, P_{nQ}^{C} are the rates of heating of the neutral gas by UV and EUV solar radiation, Joule heating and heating by precipitating energetic particles; P_{nL} is the rate of heat loss of the neutral gas due to radiation *[Namgaladze et al. 2013]*.

The UAM model calculates the O and O_2 distribution from the continuity equation (Equation 1.1). The total neutral mass density ρ is computed using the hydrostatic equilibrium equation (Equation 1.3). The N_2 distribution is obtained as the difference between the total neutral mass density and mass density of the molecular and atomic oxygen (Equation 1.5) below the turbopause level. This difference decreases with altitude and becomes comparable with the model error above the turbopause level. To avoid it, the barometric law is used to calculate the mocular nitrogen concentration above this level. The horizontal meridional (V_x) and zonal (V_y) components of the thermospheric neutral wind are obtained by using the momentum equation (Equation 1.2). The vertical wind component is calculated from the continuity equation (Equation 1.4). A separate equation is used for the vertical wind component because the momentum equation for the neutral gas is reduced to Equation 1.3 and does not contain this component. The neutral temperature distribution is computed from the heat balance equation (Equation 1.7).

The upper boundary condition at 526 km for those equations is the assumption that $\partial V/\partial r = \partial T/\partial r = 0$ and all neutral components are in diffusive equilibrium. The geostrophic approximation (or tides can be assumed alternatively) is used for the neutral wind distribution as the lower boundary condition at 80 {60} km. The temperature and concentrations of the neutral components are culculated with the empirical thermospheric models at that boundary.
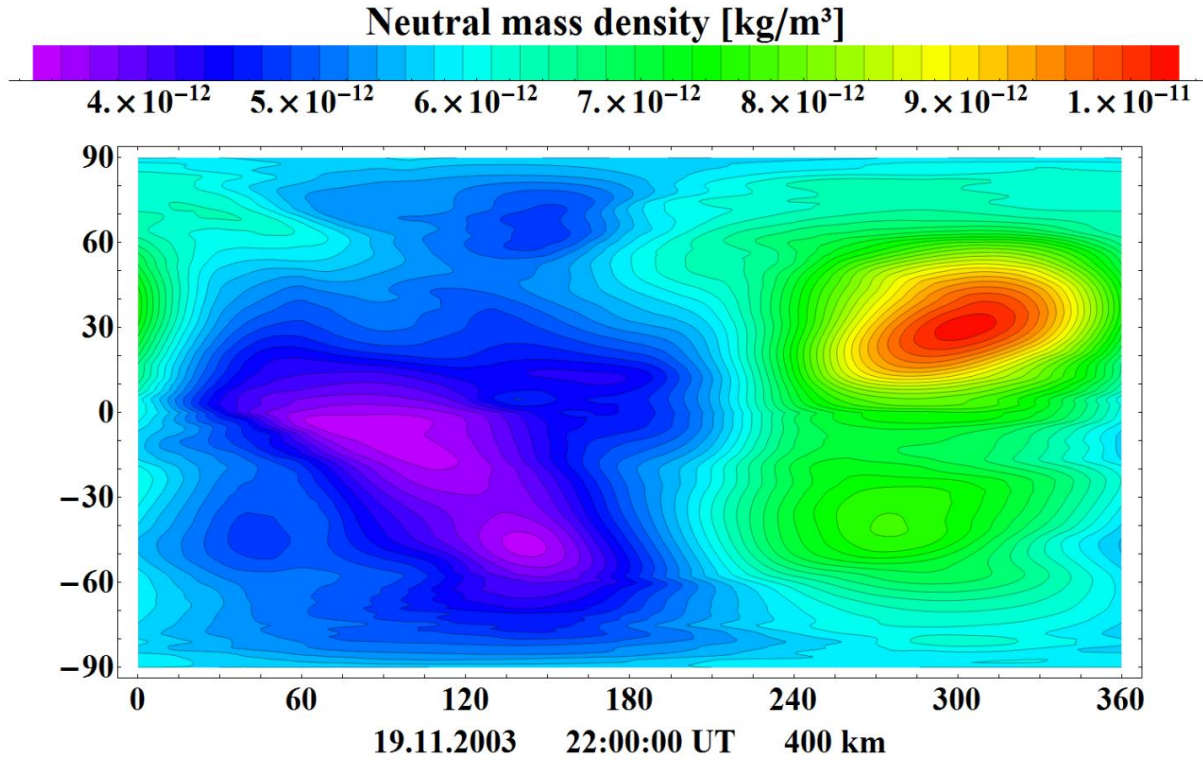
Figure 1.2. *An example of the neutral mass density distribution calculated with the UAM model for 22:00:00 UT of 19th of November 2003. The pattern is presented in the geomagnetic coordinate system.*

As shown in the example above, one neutral atmosphere parameter calculated in this section of the UAM model is shown in Figure 1.2. It represents the global neutral mass density distribution at 400 km altitude level. The neutral mass density depletion during night time (03 MLT corresponds to 120 deg. of magnetic longitude) and enhancement at the day time (15 MLT corresponds to 300 deg. of magnetic longitude) are clearly visible in the figure. The pattern also shows the equatorial anomaly *[Liu et al., 2007]*. This anomaly appears on the day side as a two-peak meridianal variation with a maximum at 40 deg in the Northern Hemisphere and second maximum at -40 deg in the Southern Hemisphere.

1.3.2. Lower ionosphere

This section of the UAM model describes the parameters of the D, E and F1 ionospheric region using a spherical geomagnetic coordinate system. The total concentration of the molecular ions $n(XY^+) = n(NO^+) + n(O_2^+) + n(N_2^+)$ together with the molecular ion velocity $V(XY^+)$ are calculated for the altitude range from 80 (60) up to the 526 km. The ion and electron temperatures T_i and T_e are computed for heights of 80 (60) km up to the 175 km. The UAM model offers the distribution of these parameters by solving the system of the continuity

(Equation 1.8), momentum (Equations 1.12 and 1.12), and energy balance (Equations 1.9 and 1.10) equations presented below.

$$\partial n(XY^+) / \partial t = Q(XY^+) - L(XY^+) , \tag{1.8}$$

$$(3\, n_i\, k\, /2\,)\, \partial T_i / \partial t = P_{iQ}{}^J + P_{iT}{}^e + P_{iT}{}^n , \tag{1.9}$$

$$(\, 3\, n_e\, k\, /2\,)\, \partial T_e / \partial t = P_{eQ}{}^p + P_{eQ}{}^c + P_{eT}{}^i + P_{eT}{}^n , \tag{1.10}$$

$$n_i m_i \boldsymbol{g} - \nabla(n_i k T_i) - \sum_n \mu_{in}\, v_{in}\, n\, (\boldsymbol{V_i} - \boldsymbol{V}) + e\, n_i\, (\boldsymbol{E} + \boldsymbol{V_i} \times \boldsymbol{B}) = 0 , \tag{1.11}$$

$$\nabla (\, n_e\, k T_e\,) + e\, n_e\, (\boldsymbol{E} + \boldsymbol{V_e} \times \boldsymbol{B}) = 0 , \tag{1.12}$$

$$n_e = \Sigma n_i. \tag{1.13}$$

In this equation system, $Q(XY^+)$, $L(XY^+)$ are the production and loss rates of the molecular ions taking into account ionization by solar EUV direct and scattered radiation, ionization by precipitating electrons, ion-molecular reactions and dissociative recombination; $P_{iQ}{}^J$ is the rate of the Joule heating of the ion gas; $P_{iT}{}^e$, $P_{iT}{}^n$ are the rates of the heat exchange between ion, electron and neutral gases; n_e is the electron concentration; $P_{eQ}{}^p$, $P_{eQ}{}^c$ are the rates of heating of the electron gas by photoelectrons and by precipitating magnetospheric electrons; $P_{eT}{}^i = - P_{iT}{}^e$; $P_{eT}{}^n$ is the rate of the elastic and inelastic exchange of heat between electron and neutral gases; m_i is ion mass; $\boldsymbol{g}$ is the vector of gravity acceleration; $v_{in}n_i = v_{ni}n_n$; e is the electron charge; $\boldsymbol{E}$, $\boldsymbol{B}$ are the electric and magnetic fields *[Namgaladze et al. 2013]*.

The charged particle transport processes are neglected in Equations 1.8, 1.9 and 1.10. This assumption is used in the UAM model because of the dominating photochemicals, local heating and heat exchange processes in the D, E and F1 ionospheric regions. The ion velocity vector distribution is obtained from Equations 1.11 and 1.12. Equation 1.13 describes the quasi-neutrality of the ionospheric plasma.
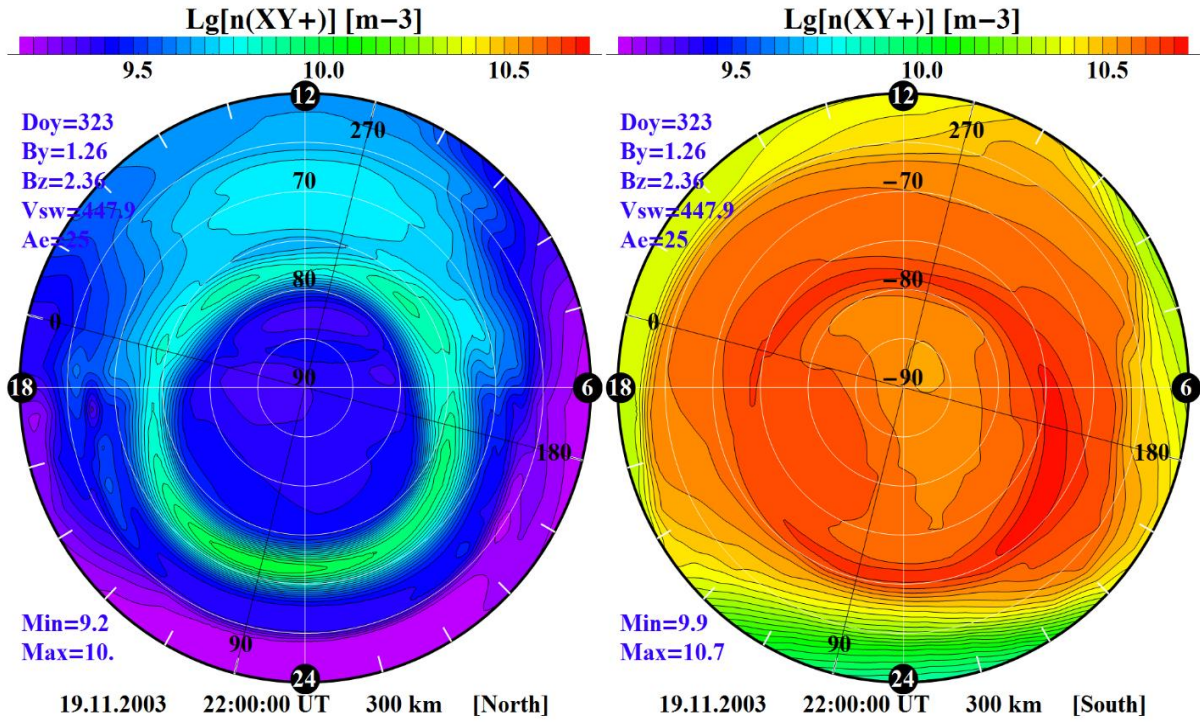
Figure 1.3. *An example of the molecular ion density distributions calculated with the UAM model for the Northern (left panel) and Southern (right panel) polar area. The time moment is 22:00:00 UT of 19th of November 2003. The patterns are presented in the polar geomagnetic coordinate system.*

The logarithm of the ion number density distributions at the 300 km level for the Northern and Southern polar regions is presented in Figure 1.3. It is one of the ionospheric parameters computed in this section of the UAM model.

The difference between the hemispheres is clearly visible in Figure 1.3. This is defined by the different solar EUV ionization fluxes for the Northern (polar night) and Southern (polar day) Hemispheres. Together with it, the molecular ion density enhancement caused by the auroral precipitation particles is also visible in both hemispheres. This enhancement constitutes a ring structure shifted by a few degrees to the night side along the noon-midnight line.

1.4. The ionospheric F2-region and protonospheric block

This part of the UAM model describes the ionospheric F2 region and the protonosphere (plasmasphere and inner magnetosphere cold plasma) parameters. The distributions of the electron, atomic oxygen and hydrogen ion densities $n(e)$, $n(O^+)$, $n(H^+)$ and $n(He^+)$ together with the electron and ion temperatures T_e and T_i and ion velocities $V(O^+)$, $V(H^+)$ and $V(He^+)$ are calculated there using the geomagnetic dipole coordinate system. The altitude range is from 175 km up to 15 Earth radii of geocentric distance. This block is based on the assumption that

all charged components are fully magnetized above 175 km ($\mu_{in} << \Omega_i$, where the Ω_i is the ion gyrofrequency). This means that the geomagnetic field has a very strong influence on the behavior of the charged particles. The electrons and ions with negligible collisions with other particles can move only along magnetic field lines. This assumption significantly simplifies the solution of the model equations. The distribution of the parameters is obtained by solving the equations along geomagnetic dipole field lines, taking into account the electromagnetic plasma drift, which is perpendicular to the vector of the magnetic field. The system of continuity (Equation 1.14), momentum (Equation 1.15) and heat balance (Equation 1.18 and 1.19) equations is presented below.

$$Dn_i/Dt + \nabla^{par}(n_i \mathbf{V}_i^{par}) = Q_i - L_i - n_i \nabla^{per} \mathbf{V}^{per} , \tag{1.14}$$

$$2\, m_i\, n_i\, (\mathbf{\Omega} \times \mathbf{V}_i)^{par} = m_i\, n\, \mathbf{g}^{par} - \nabla^{par}(n_i\, k\, T_i) - (n_i/n_e)\, \nabla^{par}(n_e\, k\, T_e) -$$

$$-\sum_n \mu_{in} v_{in}\, n_i\, (V_i^{par} - V^{par}) - \sum_j \mu_{ij}\, v_{ij}\, n_i\, (V_i^{par} - V_j^{par}) , \tag{1.15}$$

$$V_i^{per} = V_e^{per} = \mathbf{E} \times \mathbf{B} / B^2 , \tag{1.16}$$

$$V_e^{per} = \sum_i n_i\, V_i^{per} / n_e , \tag{1.17}$$

$$(3\, n_i\, k\, /\, 2)\, (DT_i/Dt + \mathbf{V}_i^{par}\, \nabla^{par} T_i) + (n_i\, k\, T_i)\, \nabla \mathbf{V}_i^{par} - \nabla^{par}(\kappa_i \nabla^{par} T_i) =$$

$$= P_{iQ}^{J} + P_{iT}^{e} + P_{iT}^{j} + P_{iT}^{n} , \tag{1.18}$$

$$(3\, n_e\, k\, /\, 2)\, (DT_e/Dt + \mathbf{V}_e^{par}\nabla^{par} T_e) + (n_e\, k\, T_e)\, \nabla \mathbf{V}_e^{par} - \nabla^{par}(\kappa_e \nabla^{par} T_e) =$$

$$= P_{eQ}^{p} + P_{eQ}^{c} + P_{eT}^{i} + P_{eT}^{j} + P_{eT}^{n} . \tag{1.19}$$

In this equation system the subscripts i, j and e refer to the ions O^+, H^+, and electrons, respectively. Q_i, L_i are the production and loss rates of O^+ and H^+ ions which take into account the photo- and corpuscular ionization, the ion-molecular reactions between O^+ and O_2 and N_2, and the charge exchange processes between O^+ and H, and between H^+ and O; $\mathbf{g}^{par}$ is the geomagnetic field aligned component of the sum of gravity and centrifugal accelerations; P_{iQ}^{J} is the rate of the Joule heating of the ion gas; P_{iT}^{e}, P_{iT}^{j}, P_{iT}^{n} are the ion heat exchange rates; P_{eQ}^{p}, P_{eQ}^{c} are the rates of local and non-local heating of the electron gas by photoelectrons and by precipitating magnetospheric electrons; P_{eT}^{i}, P_{eT}^{j}, P_{eT}^{n} are the electron heat exchange rates. The symbols *par* and *per* refer to the directions parallel and perpendicular to the geomagnetic field. The operator $D/Dt = \partial/\partial t + (V_{per}, \nabla)$ gives the Langrangian temporal derivatives along the electromagnetic drift trajectory determined by Equation 1.16 ***[Namgaladze et al. 2013]***.

Equations 1.14, 1.15, 1.16, 1.17, 1.18 and 1.19 are integrated along the geomagnetic field lines. The drift speed of the geomagnetic field lines is calculated from Equation 1.16. The boundary conditions are defined at the bases of the field lines in the Northern and Southern hemispheres at the 175 km level. The atomic ion concentrations are calculated from the photochemical equilibrium at this altitude, while the ion and electron temperatures are obtained from Equations 1.9 and 1.10. In the UAM model the geomagnetic field lines with $L \geq 15$ (line bases have magnetic latitude poleward of 75 deg) are open (here L is the parameter of McIlwain). The ion concentrations and heat fluxes are defined as zero at the upper boundary (15 R_E) for those geomagnetic field lines.
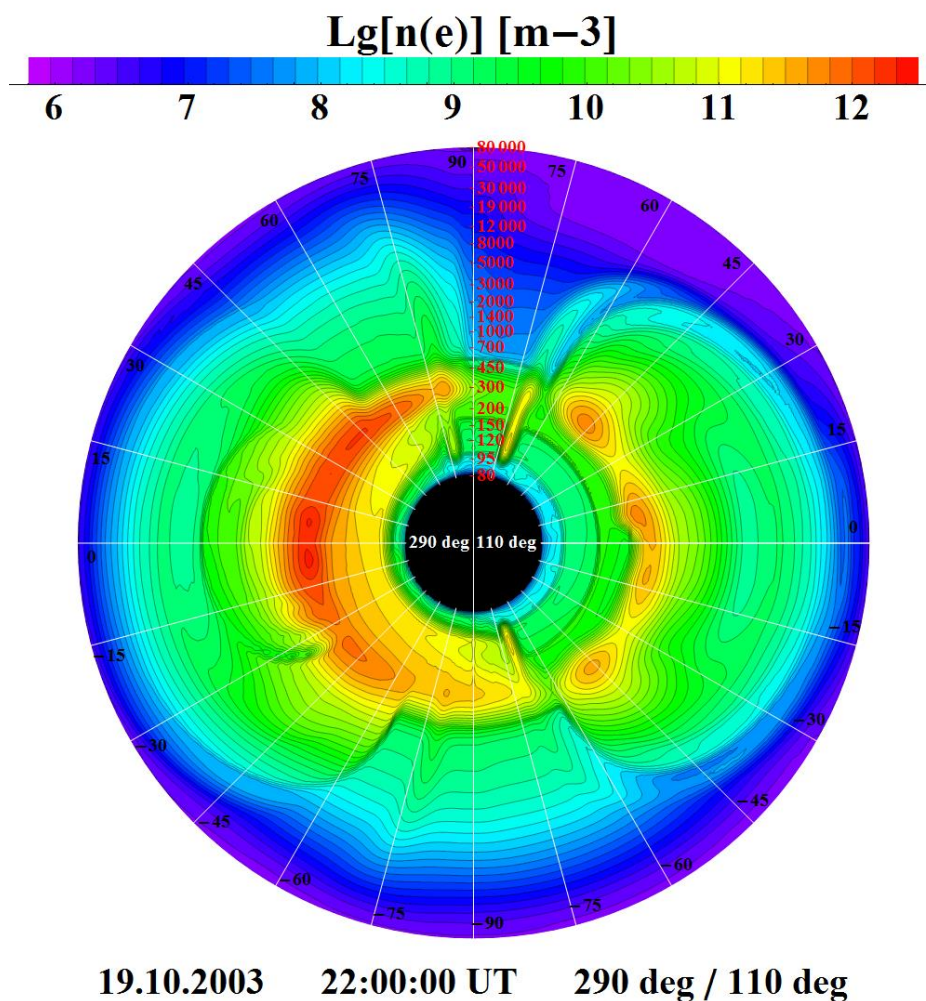
Figure 1.4. *An example of the electron density distributions obtained with the UAM model for 22:00:00 UT of 19th of November 2003. The pattern is shown in the spherical geomagnetic coordinate system (see the figure description in text below).*

The vertical distribution of the electron density (in logarithmic scale) calculated with the UAM model for the altitude range of 80 up to 80 000 km is shown in Figure 1.4. The left part of the pattern presents the dayside electron density profile along the 290 deg geomagnetic

longitude (close to the noon meridian). The right part of the pattern shows the nightside profile (close to the midnight meridian). The Northern Hemisphere with the geomagnetic pole is illustrated at the top of the figure while the Southern Hemisphere is presented at the bottom, correspondingly.

In Figure 1.4 the maximum of the F2 ionospheric region (NmF2) is clearly seen at the dayside and nightside at the altitude range of 300 – 450 km. Together with it, the electron density enhancement in the auroral region is observed. The position of the auroral region is shifted to the nightside as shown already in Figure 1.3. The contours of the geomagnetic dipole field are also well pronounced as density contours in the figure.

1.5. The electric field block

1.5.1. The electric field calculation

The magnetic field is a static in the UAM model. The additional magnetic field generated by the ionospheric current system and variation of the electric field is much less than the Earth's core magnetic field (by several orders of magnitude). This non-significant additional magnetic field is neglected in the UAM model. Hence, Maxwell's equation for the electric field $\nabla \times \mathbf{E} = -\partial \mathbf{B}/\partial t$ can be written as $\nabla \times \mathbf{E} = 0$. In other words, the modeling electric field is a potential field.

The charges driven by the external generators (the magnetospheric generator and the ionospheric generator {thermospheric wind dynamo}) flow through the ionosphere. The charge flux (current) should satisfy the continuity equation. This equation is given below:

$$\mathrm{div}\boldsymbol{j} = \mathrm{div}\ (\boldsymbol{j}_i + \boldsymbol{j}_m + \boldsymbol{j}_l) = \nabla[\sigma^{\mathrm{T}}\ (-\nabla\varphi + \boldsymbol{V}\times\boldsymbol{B}\ ) + \boldsymbol{j}_m + \boldsymbol{j}_l] = 0. \tag{1.20}$$

In this equation, σ^{T} is the tensor of ionospheric conductivity; $\boldsymbol{j}_i$, $\boldsymbol{j}_m$, $\boldsymbol{j}_l$ are the ionospheric, magnetospheric and lower atmosphere current densities, respectively. The first current density $\boldsymbol{j}_i$ represents the dynamo-action of the thermospheric winds. This term constitutes an inner source for electric field. The last two $\boldsymbol{j}_m$ and $\boldsymbol{j}_l$ are used as input parameters at the upper (175 km) and lower (80 {60} km) boundaries of the electric field block.

Ohm's law for the ionospheric current density can be represented in the following way:

$$j_i = \sigma_{par}\mathbf{E}_{par} + \sigma_p\mathbf{E}_{per} + \sigma_h\,[\mathbf{b} \times \mathbf{E}_{par}], \quad \mathbf{E}_{par} = \mathbf{B}\,(\mathbf{B},\mathbf{E})/B^2, \quad \mathbf{E}_{per} = \mathbf{B} \times [\mathbf{E} \times \mathbf{B}]/B^2,$$

where j_i represents the ionospheric current density and σ_h, σ_p, σ_{par} are the Hall, Pedersen and parallel to the magnetic field conductivities, correspondingly. These components can be written as:

$$\sigma_h = e^2 n_e[\Omega_e /m_e(\Omega_e^2 + \nu_{en}^2) - \Omega_i /m_i(\Omega_i^2 + \nu_{in}^2)],$$

$$\sigma_p = e^2 n_e[\nu_{in} /m_i(\Omega_i^2 + \nu_{in}^2) + \nu_{en} /m_e(\Omega_e^2 + \nu_{en}^2)],$$

$$\sigma_{par} = e^2 n_e[1/m_i\nu_{in} + 1/m_e\nu_{en}],$$

where m_i, m_e are ion and electron masses; Ω_i, Ω_e are ion and electron cyclotron frequencies; and ν_{in}, ν_{en} are ion-neutral and electron-neutral collision frequencies. *[Namgaladze et al. 2013]*.

The ionospheric conductivity tensor can be written for a Cartesian coordinate system as shown below:

$$\sigma = \begin{vmatrix} \sigma_{par} & 0 & 0 \\ 0 & \sigma_p & \sigma_h \\ 0 & -\sigma_h & \sigma_p \end{vmatrix} \tag{1.21}$$

The Z axis is oriented along the geomagnetic field in Formula 1.21. The UAM model uses the ideal dipole coordinate system (see section 1.7). The inclination of the Earth's magnetic field depends, therefore, on latitude only. Taking into account the angle between the geomagnetic field and the vertical direction, (1.21) can be rearranged for the spherical geomagnetic coordinate system as follows:

$$\sigma = \begin{vmatrix} \sigma_{rr} & \sigma_{r\theta} & \sigma_{r\lambda} \\ \sigma_{\theta r} & \sigma_{\theta\theta} & \sigma_{\theta\lambda} \\ \sigma_{\lambda r} & \sigma_{\lambda\theta} & \sigma_{\lambda\lambda} \end{vmatrix}$$

where $\sigma_{rr} = (\sigma_{par} - \sigma_P)\sin^2 I + \sigma_P$, $\sigma_{r\theta} = \sigma_{\theta r} = (\sigma_{par} - \sigma_P)\sin I \cos I$, $\sigma_{r\lambda} = \sigma_{\lambda r} = \sigma_h \cos I$, $\sigma_{\theta\theta} = (\sigma_{par} - \sigma_P)\cos^2 I + \sigma_P$, $\sigma_{\theta\lambda} = -\sigma_{\theta\lambda} = -\sigma_h \sin I$, $\sigma_{\lambda\lambda} = \sigma_P$, I is the magnetic field inclination.
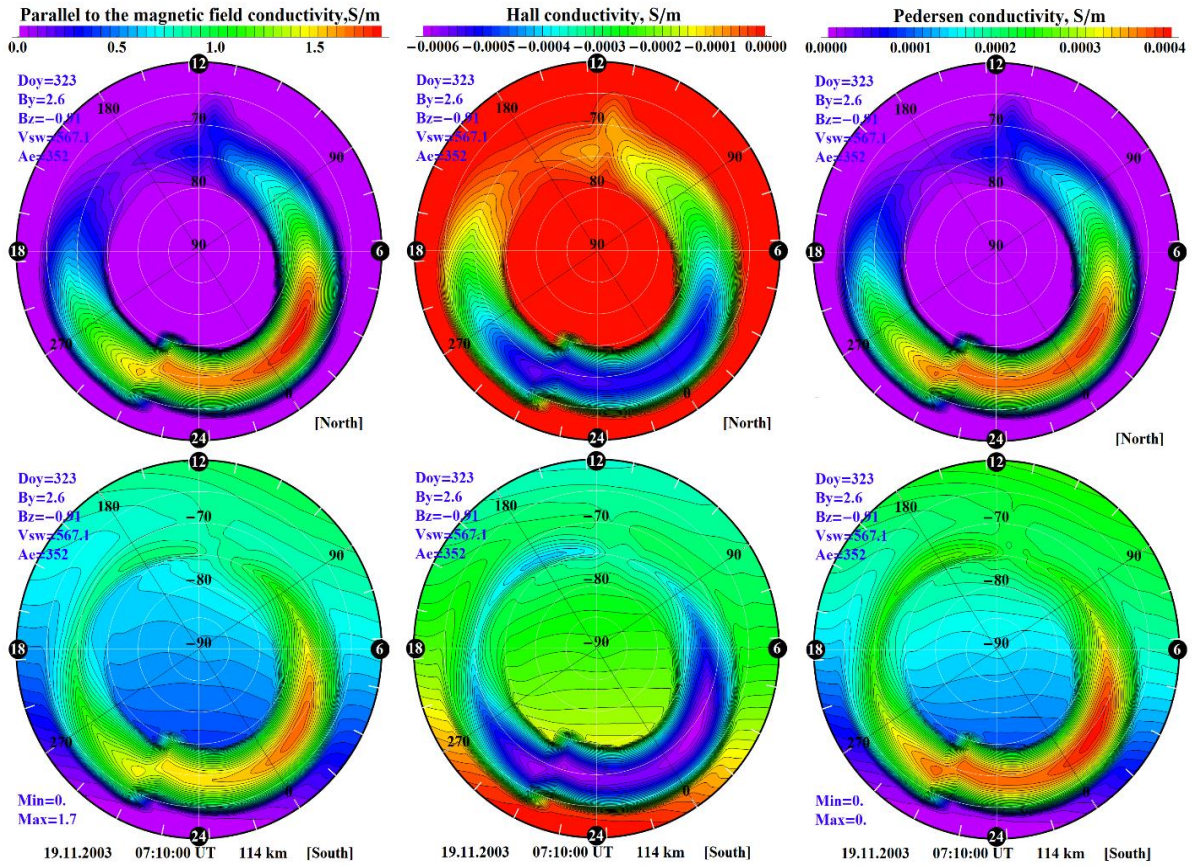
Figure 1.5. *An example of the Hall (middle column), Pedersen (right column) and parallel to the magnetic field (left column) conductivity distributions calculated with the UAM model for the Northern (upper panels) and Southern (bottom panels) polar areas. The time moment is 07:10:00 UT of 19th of November 2003. The patterns are presented in the polar geomagnetic coordinate system with an outer border at ±60 deg.*

The conductivity distributions at the altitude 114 km (near the maximum of the Hall and Pedersen conductivities) are shown in Figure 1.5. The distributions have the shape of the auroral precipitation area. The conductivity magnitudes are mostly defined by the intensity of the auroral precipitation fluxes. An additional background conductivity is provided by the solar EUV ionization fluxes. This additional conductivities are different for the Northern (polar night) and Southern (polar day) Hemispheres.

The Hall and Pedersen conductivities have their maxima in the altitudinal range ~105-130 km. On the other hand, the conductivity parallel to the magnetic field is increases with altitude and is much larger than the Hall and Pedersen conductivities (by ~ 6 - 7 orders of magnitude above the 175 km). Due to these features of the Earth's ionosphere, the component of the electric field patalel to the magnetic field can be neglected and thus the magnetic field lines can be described as electric equipotential lines.

The vertical component of the ionospheric conductivity is defined by the parallel to the magnetic field conductivity which lies inside the current-carrying region of 80{60} - 175 km at the high latitudes. Hall and Pedersen conductivities perpendicular to the magnetic field are by several orders of magnitude smaller than the conductivity parallel to the magnetic field line (See Figure 1.5). In other words, the vertical component of the Earth's electric field is by several orders of magnitude smaller than the horizontal components.

The ionospheric currents can be described as:

$$j_r = \sigma_{rr}E_r + \sigma_{r\theta}E_\theta + \sigma_{r\lambda}E_\lambda,$$

$$j_\theta = \sigma_{\theta r}E_r + \sigma_{\theta\theta}E_\theta + \sigma_{\theta\lambda}E_\lambda,$$

$$j_\lambda = \sigma_{\lambda r}E_r + \sigma_{\lambda\theta}E_\theta + \sigma_{\lambda\lambda}E_\lambda.$$

Based on the assumption that the radial component is negligibly small $(j_r \ll j_\theta, j_\lambda)$ inside the current-conducting layer, the ionospheric currents can be written as:

$$j_\theta = \hat{\sigma}_{\theta\theta}E_\theta + \hat{\sigma}_{\theta\lambda}E_\lambda,$$

$$j_\lambda = \hat{\sigma}_{\lambda\theta}E_\theta + \hat{\sigma}_{\lambda\lambda}E_\lambda,$$

where $\hat{\sigma}_{\theta\theta} = \sigma_{par}\sigma_P /(\sigma_{par} \sin^2 I + \sigma_P \cos^2 I)$, $\hat{\sigma}_{\theta\lambda} = -\hat{\sigma}_{\lambda\theta} = \sigma_{par}\sigma_h \sin I/(\sigma_{par} \sin^2 I + \sigma_P \cos^2 I)$, $\hat{\sigma}_{\lambda\lambda} = (\sigma_{par}\sigma_P \sin^2 I + (\sigma_P{}^2 + \sigma_h{}^2) \cos^2 I)/(\sigma_{par} \sin^2 I + \sigma_P \cos^2 I)$.

The neutral wind creates an additional electric current, the so called dynamo effect. This current is generated inside the current-conducting area via the collision between neutral and charged particles. The dynamo electric field caused by the neutral wind results in the following expression:

$$\mathbf{v} \times \mathbf{B} = B \cdot v_\lambda \cos I \cdot \boldsymbol{e}_r - B \cdot v_\lambda \sin I \cdot \boldsymbol{e}_\theta + B \cdot (v_\theta \sin I - v_r \cos I) \cdot \boldsymbol{e}_\lambda$$

The ionospheric current system, therefore, takes this form:

$$j'_\theta = \hat{\sigma}_{\theta\theta}E_\theta + \hat{\sigma}_{\theta\lambda}E_\lambda + B \cdot (-\hat{\sigma}_{\theta\theta}v_\lambda \sin I + \hat{\sigma}_{\theta\lambda} \cdot (v_\theta \sin I - v_r \cos I)), \tag{1.22}$$

$$j'_\lambda = \hat{\sigma}_{\lambda\theta}E_\theta + \hat{\sigma}_{\lambda\lambda}E_\lambda + B \cdot (-\hat{\sigma}_{\lambda\theta}v_\lambda \sin I + \hat{\sigma}_{\lambda\lambda} \cdot (v_\theta \sin I - v_r \cos I)). \tag{1.23}$$

The vertical component of the Earth's electric field is neglected inside the current-carrying region (80{60} - 175 km) in the UAM model, thereby allowing the integration Equation 1.20 along the vertical direction. Due to this assumption, the current-carrying layer is described as a plane. Equation 1.20 can be written for the spherical coordinate system in the following way:

$$\frac{\partial(J_\theta \sin \theta)}{\partial \theta} + \frac{\partial J_\lambda}{\partial \lambda} = r_2 \sin \theta \cdot \sin I \cdot j_{par} \,, \tag{1.24}$$

where $J_\theta = \int_{r_1}^{r_2} j'_\theta dr$, $J_\lambda = \int_{r_1}^{r_2} j'_\lambda dr$, $j_{par} = j_m + j_l$

The electric field is the minus gradient of the electric potential and can be written for the spherical coordinate system as:

$$\mathbf{E} = -\frac{1}{r}\frac{\partial \varphi}{\partial \theta} \cdot \mathbf{e}_\theta + -\frac{1}{r \sin \theta}\frac{\partial \varphi}{\partial \lambda} \cdot \mathbf{e}_\lambda \tag{1.25}$$

Equation 1.20 can be presented using Equations 1.22, 1.23, 1.24, and 1.25 in the following way:

$$\frac{\partial}{\partial \theta}\left(\alpha \frac{\partial \varphi}{\partial \theta}\right) + \gamma \frac{\partial \varphi}{\partial \theta} + \frac{\partial}{\partial \lambda}\left(\beta \frac{\partial \varphi}{\partial \lambda}\right) - \delta \frac{\partial \varphi}{\partial \lambda} = \psi \,, \tag{1.26}$$

where $\alpha = \sin \theta \cdot \int_{r_1}^{r_2} \hat{\sigma}_{\theta\theta} dr$, $\gamma = \frac{\partial}{\partial \theta}\left(\int_{r_1}^{r_2} \hat{\sigma}_{\theta\lambda} dr\right)$, $\beta = \frac{1}{\sin \theta} \cdot \int_{r_1}^{r_2} \hat{\sigma}_{\lambda\lambda} dr$, $\delta = \frac{\partial}{\partial \lambda}\left(\int_{r_1}^{r_2} \hat{\sigma}_{\theta\lambda} dr\right)$

$$\psi = -r_2^2 \cdot \sin \theta \sin I \cdot j_{par}(r_2) +$$

$$+ r_2 \frac{\partial \left(\sin \theta \cdot \int_{r_1}^{r_2} B \cdot (-\hat{\sigma}_{\theta\theta} v_\lambda \sin I + \hat{\sigma}_{\theta\lambda} \cdot (v_\theta \sin I - v_r \cos I)) \, dr\right)}{\partial \theta} +$$

$$+ r_2 \frac{\partial \left(\int_{r_1}^{r_2} B \cdot (-\hat{\sigma}_{\lambda\theta} v_\lambda \sin I + \hat{\sigma}_{\lambda\lambda} \cdot (v_\theta \sin I - v_r \cos I)) \, dr\right)}{\partial \lambda}$$

In Equation 1.26, the terms α, β, γ, and δ describe the integrated conductivity tensor of the ionosphere while j_{par} represents the magnetospheric and lower atmosphere current densities.

The thermospheric dynamo current system is defined in the UAM model by using the neutral wind distribution calculated on the previous time step. The characteristic time of the thermospheric neutral wind variation is $\sim 0.5 - 1$ hours, while the modeling time steps are $\sim 3 - 30$ seconds. In other words, the neutral wind variation is negligibly small during the modeling time steps. For this study, the magnetospheric currents are obtained from empirical models.

Equation 1.26 is solved numerically on the sphere at 175 km altitude. The detailed description of the numerical scheme was described by *Klimenko et al. 2006*. The result describes the electric potential distribution on the lower boundary of the ionospheric F2 region and the protonosphere. The electric field is defined using the equipotentiality assumption for the geomagnetic field lines above 175 km (the electric potential along the magnetic field lines is constant above 175 km). The electric field is obtained as the gradient (in B-perpendicular direction) of the electric field potential above this level.
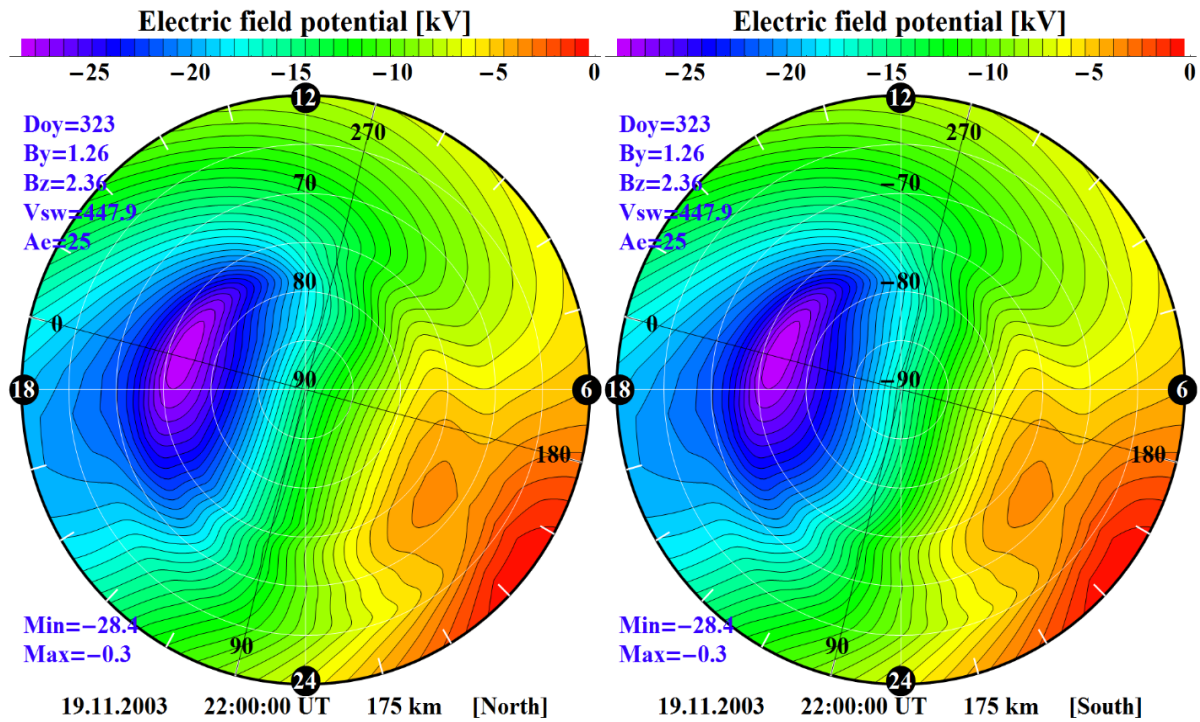
Figure 1.6. *An example of the electric field potential distributions calculated with the UAM model for the Northern (left panel) and Southern (right panel) polar areas. The time moment is 22:00:00 UT of 19th of November 2003. The patterns are presented in the polar geomagnetic coordinate system.*

Figure 1.6 illustrates the electric field potential distributions for the Northern and Southern polar regions. The distribution was calculated for low magnetic activity (AE index is 25 nT). The minima and maxima of the electric potential are clearly seen in both hemispheres at the evening and morning side, respectively. The electric field potential patterns are mirror symmetrical for both hemispheres because the FAC distribution are the same for both the Northern and Southern polar areas. In the real situation, however, this should not be the case (see Figures 2.1 and 2.2).

1.5.2 The charge separation in the Earth's ionosphere.

The plasma in the upper atmosphere is quasi-neutral. This means that the positive and negative charge densities must be equal everywhere for spatial scales more than the Debye length. The characteristic sizes of the Debye length for the upper atmosphere have the order of a few millimeters up to a few centimeters (increasing with altitude).
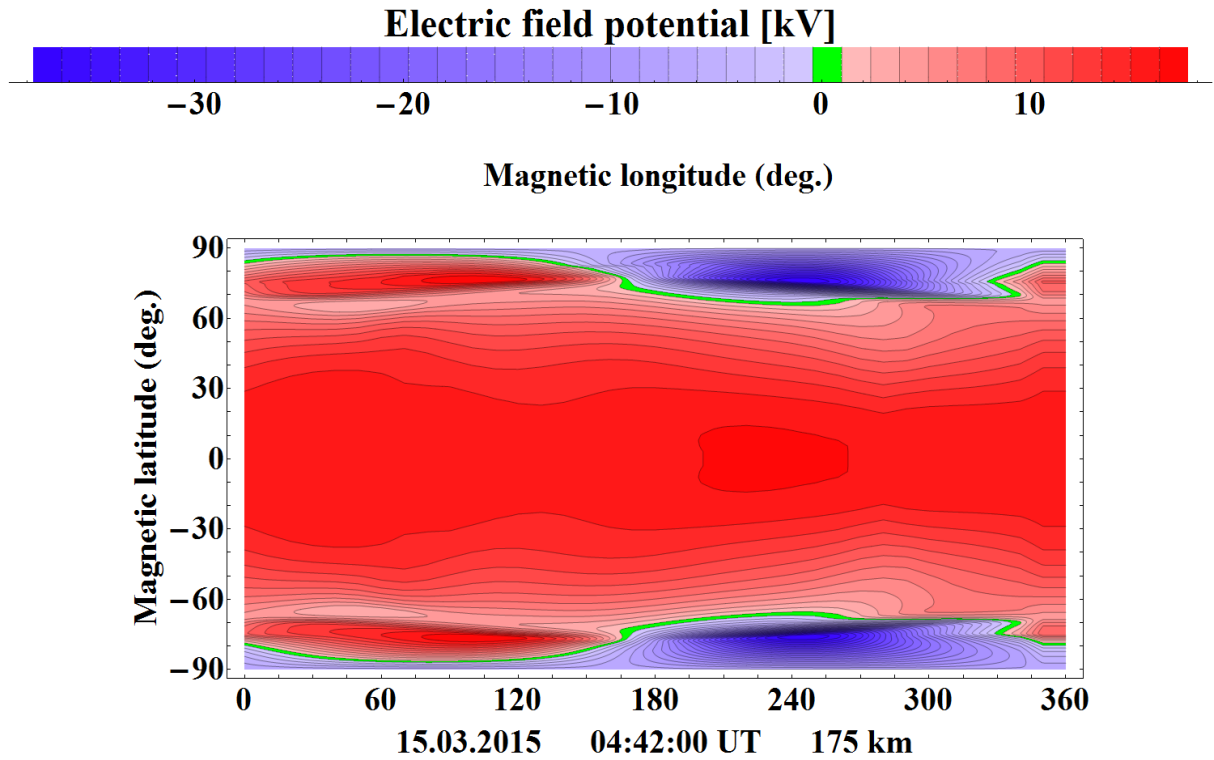
Figure 1.7. *An example of the electric field potential distributions calculated with the UAM model for 04:42:00 UT of 15th of Mach 2015. The pattern is presented in the geomagnetic coordinate system.*

On the other hand, for modeling the Earth's electric field the Maxwell's equation can be written as:

$$\nabla \cdot \mathbf{E} = \rho / \varepsilon_0, \tag{1.27}$$

where $\mathbf{E} = -\nabla \varphi$ is electric field (φ is the electric field potential); $\rho = n[e] * q_e$ is the charge density ($n[e]$ is electron density; q_e is electron electric charge {$q_e = 1.602176565(35) * 10^{-19}$ C}); and ε_0 is electric constant ($\varepsilon_0 = 8.854187817 * 10^{-12}$ F/m).

This additional charge density is the result of the charge separation generated by the magnetospheric and ionospheric generators. This charge separation creates the electric field

(external to the ionosphere). This electric field drives charged particles (electrons and ions) providing the electric current in the Earth's ionosphere.
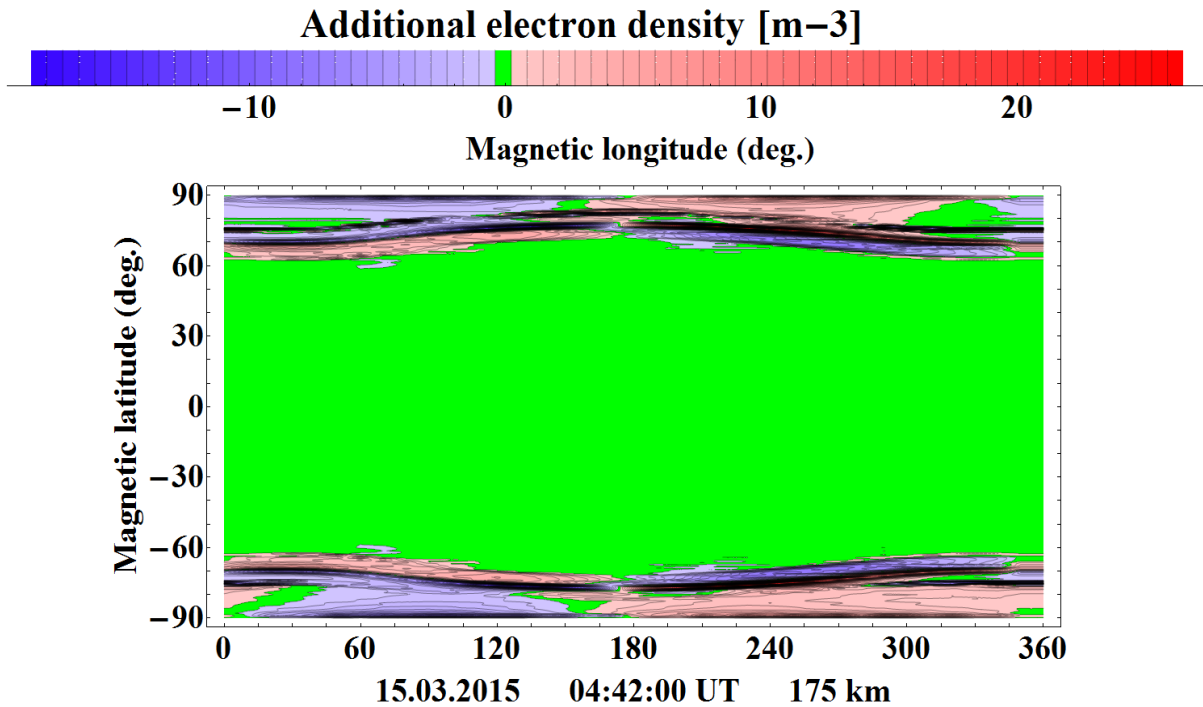
Figure 1.8. *Additional electron density (charge separation) with respect to the electric field potential distributions calculated with the UAM model for 04:42:00 UT of 15ᵗʰ of Mach 2015. The pattern is presented in the geomagnetic coordinate system. Max=26.5m⁻³; Min=-18.5m⁻³.*

Figure 1.8 represents the additional electron density obtained from the electric potential distribution presented in Figure 1.7 using Equation 1.27. The maxima values of the additional charge density are located at high latitudes where the maxima values of the electric field are located.

The strongest charge separation is visible at the auroral precipitation areas. Those distributions have the structure and shape similar to those of the magnetospheric FAC distribution (see Figure 2.4).

Other maxima of the additional charge density are clearly seen near the Northern and Southern poles. The poles in the UAM model are singular points where the electric field potential is calculated as average of the nearest numerical grid point values. Those maxima close to the poles mainly represent an artificial numerical effect. Their magnitude depends on the first latitudinal step of the spatial grid (here it is ~1.1 deg.). This effect increases along with the resolution of the numerical spatial grid near the poles.

The Earth's global electric field can be defined using the classical electrostatic theory. In other words, Equation 1.27 can be used instead of Equation 1.20. The example of such electric field reconstruction is shown in Figure 1.9.
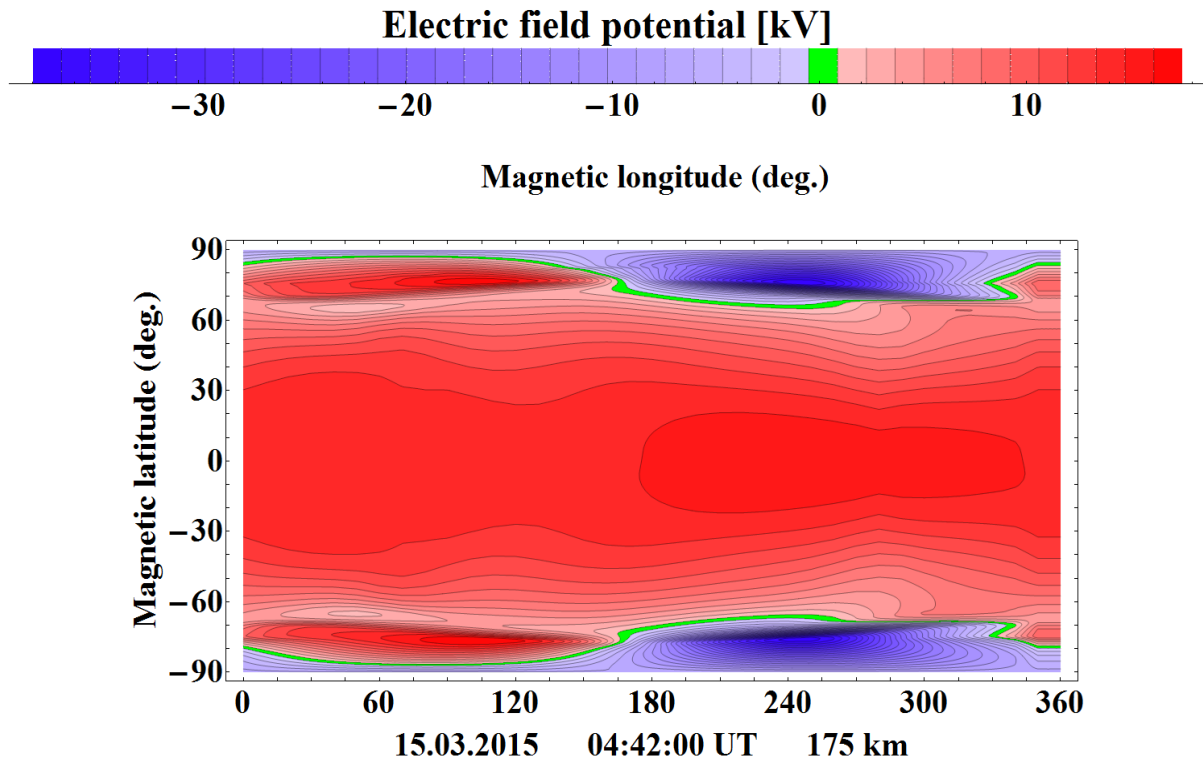
Figure 1.9. An example of the electric field potential distributions obtained using the additional charge density for 04:42:00 UT of 15th of Mach 2015. The pattern is presented in the geomagnetic coordinate system.

The electric potential pattern (Figure 1.9) was calculated using only the additional charge density distribution (taken Figure 1.8) completly without knowledge about the ionosphere. Figures 1.9 and 1.7 are the same. The negligible difference took place because of the numerical calculation precision.

This is a very simple way to define the global electric field at the first glance. On the other hand, finding such charge density in the space is a massively complicated without any information about the electric field. Due to this, the electric field is obtained from Equation 1.20 in the UAM model. The additional information about the ionosphere including the perfect conductivity along the magnetic field lines; the electric field is a potential field simplifies the definition of global electric field. If the global electric field is defined at the lower boundary then it is known everywhere (see Section 1.5.1).

The charge separation breaks the quasi-neutrality of the ionospheric plasma. Is this significant or not? To answer this question, the additional charge density should be compared with the background charge density, which refers to the concentration of electrons or ions.

**Figure 1.10.** *Equatorial vertical cut of the additional electron density with respect to the electric field potential distributions calculated with the UAM model for 04:42:00 UT of 15th of Mach 2015.*

The charge separation magnitude depends on the strength of the Earth electric field (see Equation 1.27). This is clearly seen in Figure 1.8. The absolute value of the Earth's electric field decreases along with the altitude. The distance between the equipotential magnetic field lines is growing along with the altitude. Hence, the maximal values of the additional charge density are located at the lower boundary (175 km). At the same time, the magnitude of the charge separation decreases along with the altitude (see Figure 1.10).

Figure 1.11. *The electron density distributions obtained with the UAM model for 04:42:00 UT of 15th of Mach 2015. Min=7.39*10^9 m^-3*

The minimal value of the background electron concentration is $7.39*10^9$ m^{-3} (see Figure 1.11). The computer precision is six digits (Fortran; Real*4). In other words, the calculation accuracy for the electron density is about $\sim 10^3$-10^5 m^{-3}.

The maximal value of the additional electron density (charge separation) is 26.5 m^{-3} (see Figure 1.8). This value is smaller than the precision of the background electron concentration calculation by a few orders of magnitude.

The altitudinal distribution of the additional electron density shown in Figure 1.10 can be compared with the vertical electron density profile presented in Figure 1.4.

1.6. The magnetospheric block

This section of the UAM model describes the magnetospheric plasma. The system of the equation for continuity and momentum equations for energetic ions is presented in Equation 1.28 and Equation 1.29, respectively:

$$\partial n_i / \partial t + \nabla(n_i V_i) = 0 , \tag{1.28}$$

$$n_i e(\boldsymbol{E} + V_i \times \boldsymbol{B}) = \nabla p_i , \tag{1.29}$$

$$d (pV^\gamma) / d t = 0, \qquad \gamma = 5/3 ,$$

$$j_{//} = \mathbf{e}_z[\nabla V, \nabla p_i] / B , \qquad V = B \int_0^1 B^{-1} \, dz ,$$

In these equations, $j_{//}$ is the field-aligned current density; $\boldsymbol{E}$ and $\boldsymbol{B}$ are the electric and geomagnetic fields; $\boldsymbol{e}_z$ is the field-aligned (**B**-parallel) unit vector; V is the half-volume of the geomagnetic field tube; z is the distance along the geomagnetic field line; l is the value of z at the top of the geomagnetic field line; p_i is the magnetospheric ion gas pressure considered isotropic and constant along the geomagnetic field line; n_i is the magnetospheric ion concentration; V_i is the magnetospheric ion drift velocity; and e is the electron charge *[Namgaladze et al. 2013]*.

Several assumptions are used in this section: 1) the magnetospheric electrons are considered to be cold; 2) their pressure is neglected in comparison with that of the magnetospheric ions; 3) the Earth magnetic field has a dipole geometry; 4) the geomagnetic field lines are closed at latitudes equatorward of the polar cap boundary (latitude less than 75 deg.); and 5) the field lines are open inside the polar cap areas *[Volkov and Namgaladze 1996; Namgaladze et al. 2013]*. Please note that this block is included into the UAM model as an option. I did not use it for my study.

1.7. Input parameters

The following input parameters are used in the UAM model: time (day of year and UT time); solar flux F10.7; geomagnetic activity AE (Kp) indexes; solar wind velocity; B_Y and B_Z components of the IMF; precipitation particle fluxes; FAC distribution; and vertical currents at the lower boundary which are not used here.

The first parameter – time - defines the Earth's position and orientation in the Sun – Earth system.

The solar activity is presented in the UAM model by the flux F10.7. The solar UV and EUV fluxes depend on the solar activity. They are responsible for the ionization by illumination.

The UV and EUV spectra are calculated using the data from ***Ivanov-Kholodny and Nusinov 1987.*** The intensities of night sky scattered radiation are chosen equal to 5kR for $\lambda = 121.6$ nm and 5R for each of the other emission lines ($\lambda\lambda = 102.6$ nm, 58.4 nm, 30.4 nm) ***[Namgaladze et al. 2013]***.

In the UAM model precipitation particle fluxes given by the empirical model of ***Hardy et al. [1985]*** are used. This model provides the spatial distribution of precipitation electron fluxes at the upper boundary of the thermosphere (526 km) following the formulas given below:

$$I(\Phi,\Lambda,E) = I_m(E)\exp[-(\Phi - \Phi_m(E))^2/(\Delta\Phi(E))^2 - (\Lambda - \Lambda_m(E))^2/(\Delta\Lambda(E))^2],$$

$$\Phi_m = (\Phi_{md} + \Phi_{mn})/2 + (\cos\Lambda)(\Phi_{md} - \Phi_{mn})/2,$$

where Φ, Λ are the geomagnetic latitude and longitude; $\Lambda = 0$ corresponds to the midday magnetic meridian; $I_m(E)$ is the maximum intensity of the precipitating electron flux; E is the energy of the precipitating electrons; Φ_{md}, Φ_{mn} are the geomagnetic latitudes of the maximum precipitation at the midday and midnight magnetic meridians. All precipitation parameters, I_m, Φ_{md}, Φ_{mn}, $\Delta\Phi$, Λ_m, and $\Delta\Lambda$ are dependent on various geophysical conditions ***[Namgaladze et al. 2013]***.

Indices of the geomagnetic activities (AE {Kp}) are used in the UAM model to define the intensity and position of the precipitation fluxes and FAC as well as the cross polar cap potential drop.

The magnetospheric FAC distribution in the UAM model is presented by the system of the Region 1, 2 and 0 currents. The Region 1 currents flow into the ionosphere on the dawn side and out of the ionosphere on the dusk side. They are located on the inner boundary of the polar region close to the polar boundary of the auroral precipitation area. The Region 2 currents flow opposite to the FACs of Region-1 and are located equatorward close to the outer boundary of the auroral precipitation area. The Region 0 currents are located in the cusp region. The FAC system is a very sensitive and highly variable system with dependences on geophysical conditions such as geomagnetic activities, the IMF orientation and seasons. The spatial distribution of the FAC system has been realized in this study by one of the following empirical models: ***Iijima and Potemra [1976]*** (see Chapter 2); ***Papitasvily et al. [2002]*** (see Chapter 3); ***He et al. [2012]*** (see Chapter 4). Alternatively, there is an opportunity to include any other physically realistic distribution of FAC using adaptation algorithm described in Section 3.4.

The solar wind velocity with B_Y and B_Z components of the IMF is used in the electric field block as input parameters for IMF dependent empirical FAC models.

The vertical lower atmospheric currents are going from the Earth to the lower ionospheric boundary. These currents are used to model disturbances in the upper atmosphere, of which the electric origin is in the lower atmosphere. One example is the modeling of disturbances in total electron content which take place before strong seismic events. Please note again thas these currents are included into the UAM model as an option. I did not use them for my study.

1.8. Initial conditions

The global empirical NRLMSISE00 *[Picone et al., 2002]* and IRI *[Bilitza 2001]* models are used as initial conditions for the UAM model. The first model provides the global distribution of neutral atmosphere parameters such as the temperature and composition of the neutral components and their spatial distributions for the altitude range of 80-526 km. The second empirical model provides the distribution of the charged particles in the ionosphere. On the other hand, any other more or less physically realistic space distribution of the upper atmospheric parameters can be used as the start condition for the UAM model.

Alternatively, instead of running the theoretical part of neutral atmosphere there is a possibility to use the empirical NRLMSISE00 model for the neutral atmosphere parameters in following ways: to use only the empirical profile of temperature; and to use only the empirical distribution of the neutral gas components; to use both of them together.

The UAM model provides its own steady state of the atmospheric parameters after some running time of the model is based on the system of equations. This solution can be significantly different from the start conditions. Here time depends on the altitudes, start conditions (how close they are to the model's steady state) and modeling parameters such as time steps, space grid and number of internal iterations. Usually, the UAM model runs for one full model day to avoid transient processes. For dense spatial grids and small time steps several hours can be sufficient.
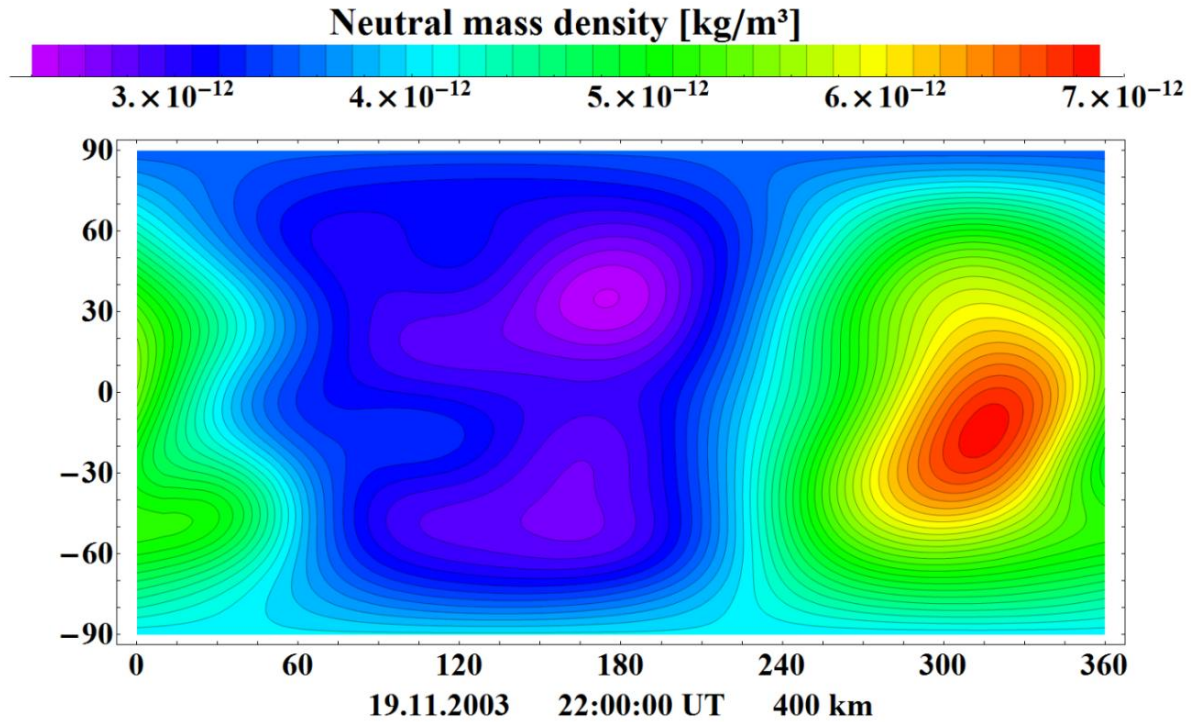
Figure 1.12. *An example of the neutral mass density distribution calculated with the NRLMSISE00 model for 22:00:00 UT of 19th of November 2003. The pattern is presented in geomagnetic coordinates.*

Figure 1.6 illustrates the neutral mass density distribution obtained with the empirical NRLMSISE00 model for the 400 km level. The input parameters are the same as those for Figure 1.2, which was calculated with the theoretical UAM model. The empirical model does not reproduce the equatorial mass density anomaly that was detected by the CHAMP accelerometer observations *[Liu et al., 2007]*. Figures 1.2 and 1.12 clearly reveal the difference between the UAM and NRLMSISE00 models in the spatial distribution of the neutral mass density as well as in the magnitude range. As seen in Figure 1.2, the NRLMSISE00 provides one maximum for the dayside. On the other hand, the UAM model presents the equatorial anomaly. The empirical NRLMSISE00 model was used as start condition for this model run.

1.9. Coordinate systems

The UAM model describes the Earth's environment by using both the spherical geomagnetic and the dipole coordinate systems.

The spherical geomagnetic coordinate system has its polar axis orientated along the geomagnetic axis. The polar angle in this coordinate system is geomagnetic co-latitude. The relation between this coordinate system and the geodetic coordinate system can be written as:

$$\cos \Theta = \cos \theta_0 \cos \theta + \sin \theta_0 \sin \theta \cos (\lambda - \lambda_0),$$

$$\cos \Lambda = [- \sin \theta_0 \cos \theta + \cos \theta_0 \cos (\lambda - \lambda_0)] / \sin \Theta,$$

$$\cos \theta = \cos \theta_0 \cos \Theta - \sin \theta_0 \sin \Theta \cos \Lambda,$$

$$\cos (\lambda - \lambda_0) = [\sin \theta_0 \cos \Theta + \cos \theta_0 \sin \Theta \cos \Lambda] / \sin \theta,$$

where Θ, Λ are geomagnetic co-latitude and longitude; θ, λ are geodetic co-latitude and longitude; θ_0, λ_0 are geodetic coordinates of the Northern geomagnetic pole, which is equal to 11.3° colatitude and −70.6° W longitude, correspondingly.

This coordinate system is used for the neutral atmosphere and lower ionosphere blocks as well as for the electric field block. It is effectively for the describtion of the interaction between neutrals, charged particles and magnetic field.

Together with it, the UAM model uses a dipole coordinate system. This coordinate system is very suitable for the description of the behavior of charged particles in the geomagnetic field of the Earth. One basic model assumption is that the charged particles can move only along the magnetic field lines in the upper atmosphere (above 175 km). This is well justified because of $\nu_{in} \ll \Omega_i$ above this height (where ν_{in} is ion-neutral collision frequency and Ω_i is ion gyrofrequency). Based on this, the system of equations of charged particles is implified significantly. This results in a simplified system of equations in which the system of equations for the particles become one-dimensional (along **B**) instead of three-dimensional. The relation between the dipole and the magnetic coordinate systems can be written as:

$$u = (R_E/r) \sin^2 \Theta,$$

$$q = (R_E/r)^2 \cos \Theta,$$

$$v = \Lambda,$$

where, u – perpendicular to vector of geomagnetic field and variable in the geomagnetic meridianal plane; q – variable along field line; v – perpendicular to u and q; Θ, Λ – geomagnetic co-latitude and longitude; R_E – radius of the Earth.

The dipole coordinate system is used in the ionospheric F2-region and protonospheric block and in the magnetospheric block.

1.10. Spatial grids

The UAM model computes the parameters of the upper atmosphere in the nodes of the spatial grid by solving the system of modeling equations using finite-difference numerical methods.

1.10.1. Spatial grid for the lower ionosphere and the neutral atmosphere

A spherical spatial grid is used in the model for the lower ionosphere and the neutral atmosphere at the altitude range of 80 − 526 km.
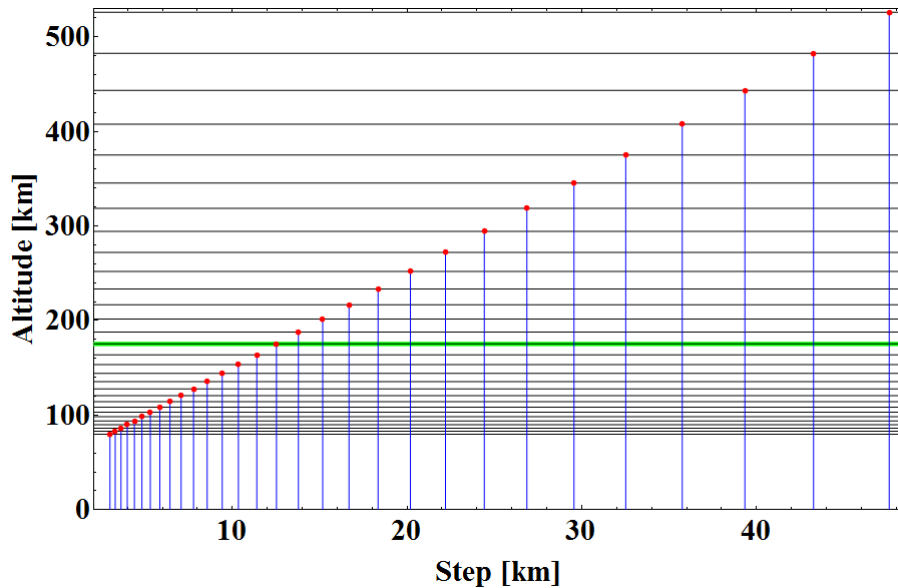
Figure 1.13. *The altitude levels (black horizontal lines) of the spherical spatial grid model for the lower ionosphere and neutral atmosphere. The altitudinal spatial steps are shown by the blue vertical lines. The green horizontal line represents the lower boundary (175 km) of the ionospheric F2 region and the protonosphere.*

The altitude levels of the UAM model for the lower ionosphere and neutral atmosphere are shown in Figure 1.13. This space grid has variable altitude steps, varying from 3 km near the lower boundary at h = 80 km, 5 km near h = 100 km, 15 km near h = 200, 25 km near h = 300 km and 40 km near upper boundary h = 526. The model uses 30 altitude levels.

The longitudinal spatial steps can be selected depending on the modeling task. Usually, the UAM model uses longitudinal space steps in the range of 5 − 15 deg. I use 10 deg step for the present study.

The latitudinal steps can also be selected depending on the modeling task. The UAM model can use regular latitudinal steps in the range of 1 – 10 deg as well as irregular steps. Steps of an irregular grid have a latitudinal dependence *[Namgaladze et al., 1995 a, b]*. Due to the irregular spatial steps along the meridian, the UAM model can focus on a particular area. For example, I use small latitudinal steps for auroral region for the present investigation (section 4.3.1). Such grid (see Figure 4.3) also allows the study of the processes in the high latitude with high spatial resolution.

1.10.2. Spatial grid for the electric field, the ionospheric F2 region and the protonosphere

Together with the spherical spatial grid, the UAM model uses a spatial grid in the dipole coordinate system. This grid is used for the description of the electric field, ionospheric F2 region and protonosphere in the altitude ranging from 175 km up to 15 R_E. The footpoints of the geomagnetic field lines are defined at the lower boundary (175 km). The longitudinal and latitudinal distributions of this grid have the same principle as the spherical grid. There is an option to use the same longitudinal and latitudinal spatial steps as in the spherical grid for the dipole grid at the lower boundary (175 km) as well as a grid with different spatial steps (with interpolation between the various spatial grids).

The altitude levels of the dipole grid are indicated by certain numbers of the nodes along the magnetic field line. These numbers vary from 9 on the innermost equatorial field line to a maximum value of 140 on the field line with L =15.

2. The UAM model with and without dependence on IMF

2.1. Introduction

The materials of this chapter were partially published in **Förster et al. 2011b and Namgaladze et al. 2013**. Some figures and tables were directly taken from these papers.

This part of my thesis describes the algorithm of the electric field calculation, which was used in the standard version of the UAM model. The standard variant used a symmetrical distribution of the FAC for the Northern and Southern Hemispheres. The system of the FAC was defined by the empirical model of **Iijima and Potemra [1976]** (IPM). The FAC was specified by the Region 1 and Region 2 currents. These currents were located at the poleward (Region 1) and equatorward (Region 2) boundaries of the auroral oval. The same boundaries are limited the auroral precipitation area.

Subsequently, I describe the improvement of the UAM model obligatory complies with the requirements of the present study, which focuses on the physical processes at high (auroral and polar cap) latitudes. The high latitude polar cap region and auroral zones turn out to be very dynamic areas of the Earth's environment due to their close connection to the magnetospheric interaction with the continuously variable solar wind and its imbedded IMF. The main driver of the large-scale magnetospheric convection are the reconnection processes at the magnetopause and in the magnetosphere tail, which are highly dependent on the IMF orientation the IMF B_Y and B_Z components in particular.

That improvement was achieved by including the IMF dependence. This dependence was added to the UAM model via the modification of the electric field. For this purpose, the pre-calculated distributions of the electric field potential were modified and used as an input parameter for the simulation run with the UAM model. The modification was performed by twisting the electric potential patterns inside the polar area in the opposite directions for the Northern and Southern Hemispheres depending on the B_Y component of the IMF. For positive B_Y the twisting was clockwise in the Northern Hemisphere and anticlockwise in the Southern Hemisphere and vice versa for negative IMF B_Y. This was done together with an adaptation of the cross polar cap potential drop to the IMF orientation.

The simulation with the modified version of the UAM model was performed for October 28, 2003. The obtained results were compared with the CHAMP satellite data. In this study I used the cross track accelerometer measurements of the thermospheric neutral wind data. The comparison shows good agreement between the modeling results and the observation data. The significant improvement is also clearly seen in Figure 2.14 by comparing the model run without (left panel) and with inclusion of the IMF B_Y dependence (right panel) in relation with the CHAMP cross trek measurements.

2.2. IMF

The Earth electric field geometry significantly depends on the IMF orientation. The statistical electric potential distributions for the Northern and Southern polar areas are shown in Figures 2.1 and 2.2. The patterns were obtained using the Cluster satellite measurements between February 2001 and March 2006. The observations were performed by the Electron Drift Instrument (EDI) *[Haaland et al. 2007]*.
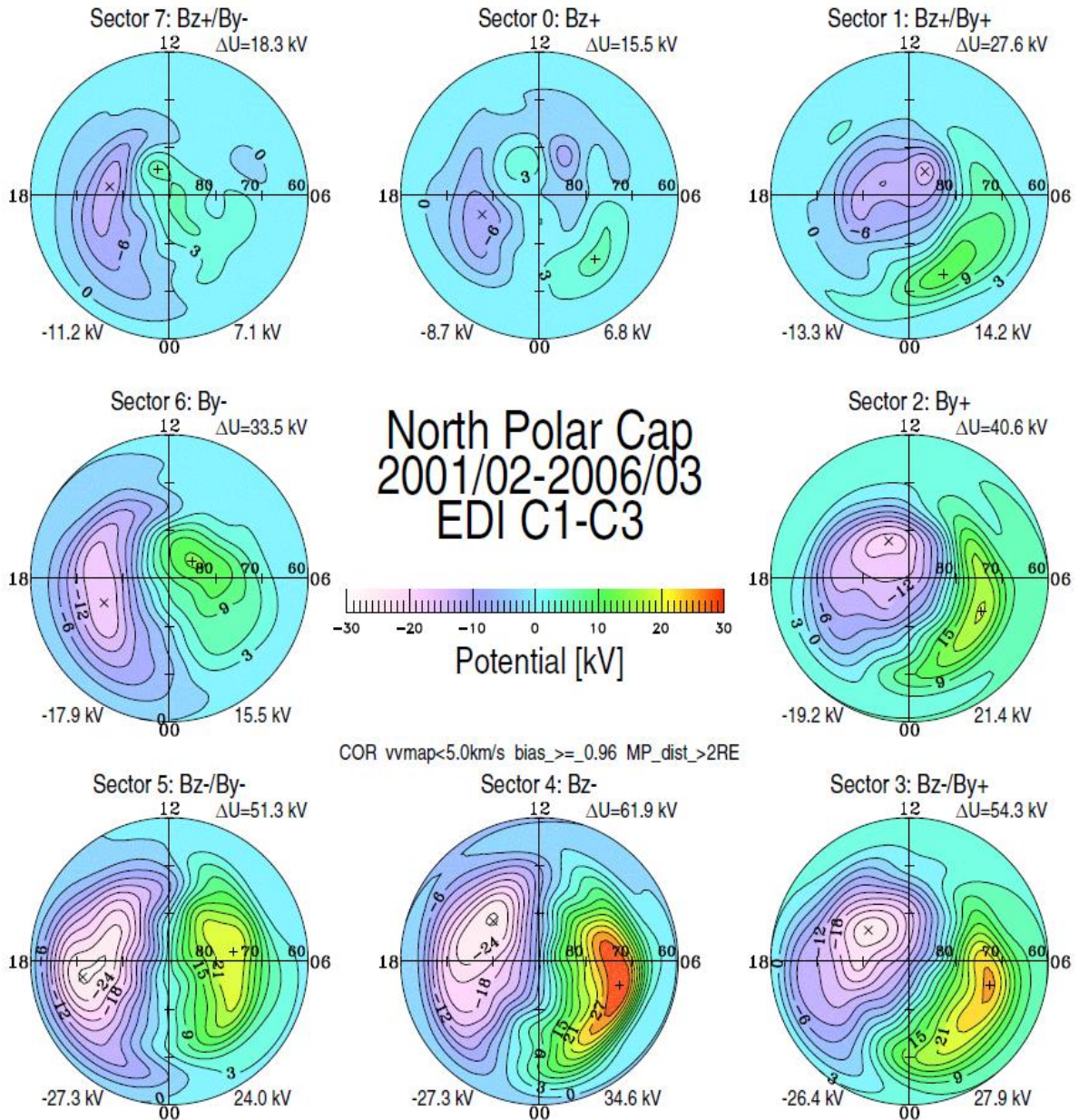
Figure 2.1. *Electric potentials in the Northern Hemisphere, as a function of AACGM latitude and magnetic local time, for 8 clock-angle orientations of the IMF, obtained by mapping the Cluster EDI velocity measurements into the ionosphere. The background color shows the value of the potential, according to the color bar at the center. Lines are drawn at fixed values of the*

potential, with a 3 kV spacing. The minimum and maximum potentials are listed at the bottom, and the total potential at the upper right of each map. ***[Haaland et al. 2007]***
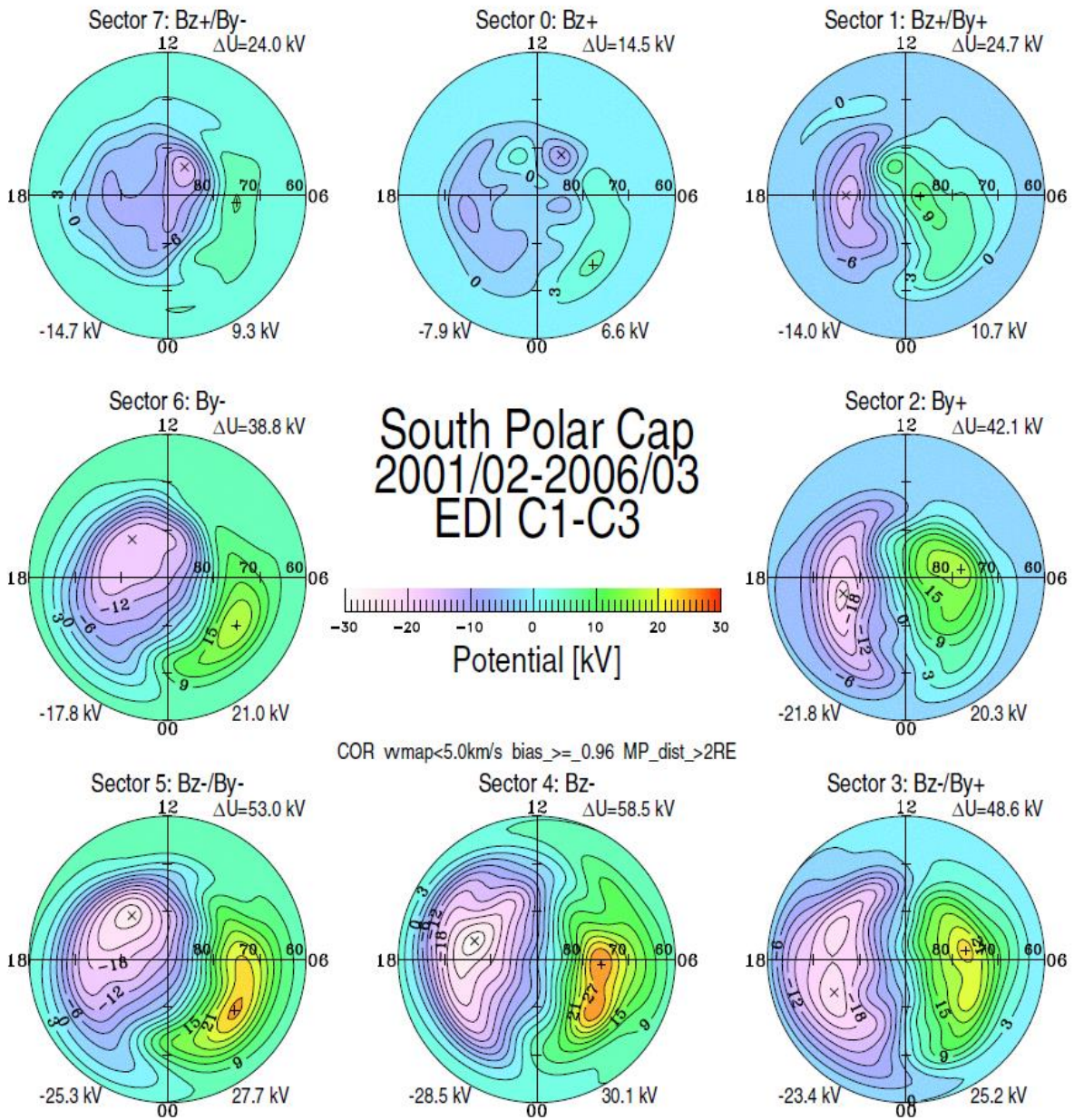
Figure 2.2. *Same as Figure 2.1, but for the Southern Hemisphere.* ***[Haaland et al. 2007]***

The patterns are shown in AACGM coordinate system for both hemispheres. The electric potential distributions are organized according to the IMF orientation (sectors 0-7). The southward IMF is strictly valid only for Sectors 3-5; for Sectors 2 and 6 the average of IMF B_Z for both sectors is zero while B_Y is positive for Sector 2 and negative for Sector 6 (see sectors 2-6 in Figures 2.1 and 2.2). Two additional convection cells appear on the day side at high latitudes close to the cusp region for the northward IMF orientation (see sectors 0). Together with it, the asymmetry is visible for the positive and negative IMF B_Y components. The evening

convection cell dominates for the positive IMF B_Y at the Northern Hemisphere (see sector 2 in Figure 2.1), while the morning cell dominates for the negative IMF B_Y (see sector 6) (Northern Hemisphere). The electric potential patterns show an asymmetrical behavior for the Southern Hemisphere.

In Figures 2.1 and 2.2 it is clearly seen that the IMF has a strong impact on the Earth electric field, which plays a great role in the MIT coupling system.

2.3. The UAM model without dependence on IMF

2.3.1. The empirical FAC model of Iijima and Potemra

In the standard version of the UAM model, the empirical FAC model *of Iijima and Potemra [1976]* (IPM) defined the FAC system. This model provides the local time distribution of the FAC.

The IPM model was used as input parameter for the UAM model with several assumptions:

1. The FAC distributions for the Northern and Southern polar regions were the same. The system of the FAC was specified by two parallel rings shifted by a few degrees to the night sector (along the noon – midnight meridian) with opposite (upward/downward) current flow directions described as the Region 1 and Region 2 currents.

2. The boundary between the open and closed field lines was the position of the Region 1 currents. This boundary was used in the UAM model to define the equipotentiality area. Along each meridian, all magnetic field lines, which are located equatorward of the Region 1 currents (including), are closed. The magnetic field lines placed outside this area (poleward of this boundary) are open. The electric potentials at both ends of the closed field-lines are equal. The open field-lines could have different electric potential values at the ends.*

   The UAM model uses an ideal dipole field and describes only the part of the Earth magnetosphere up to 15 R_E. The modeling definitions for the open and closed field-lines are different from the real situation. From the modeling point of view, the open field lines are the lines going outside the modeling area.

Such configuration of the FAC system provides symmetrical electric potential distributions for the Northern and Southern polar regions with small differences inside the area poleward of the Region 1 currents.
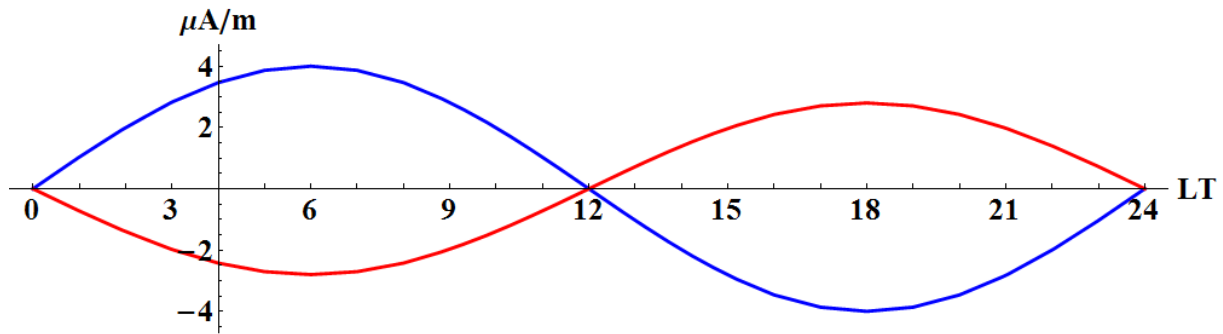
Figure 2.3. *An example of the local time Region 1 (blue) and Region 2 (red) currents profiles for the Northern Hemisphere.*

In Figure 2.3 the Region 1 currents are defined by a harmonic function (k*Sin[LT]). The local time distribution of these currents has maxima in the morning sector (6 LT) and minima in the evening side (18 LT). The zero values are located on the noon-midnight meridian. The Region 2 currents have a mirror symmetric distribution with a reduced amplitude (R2 = - 0.7*R1).
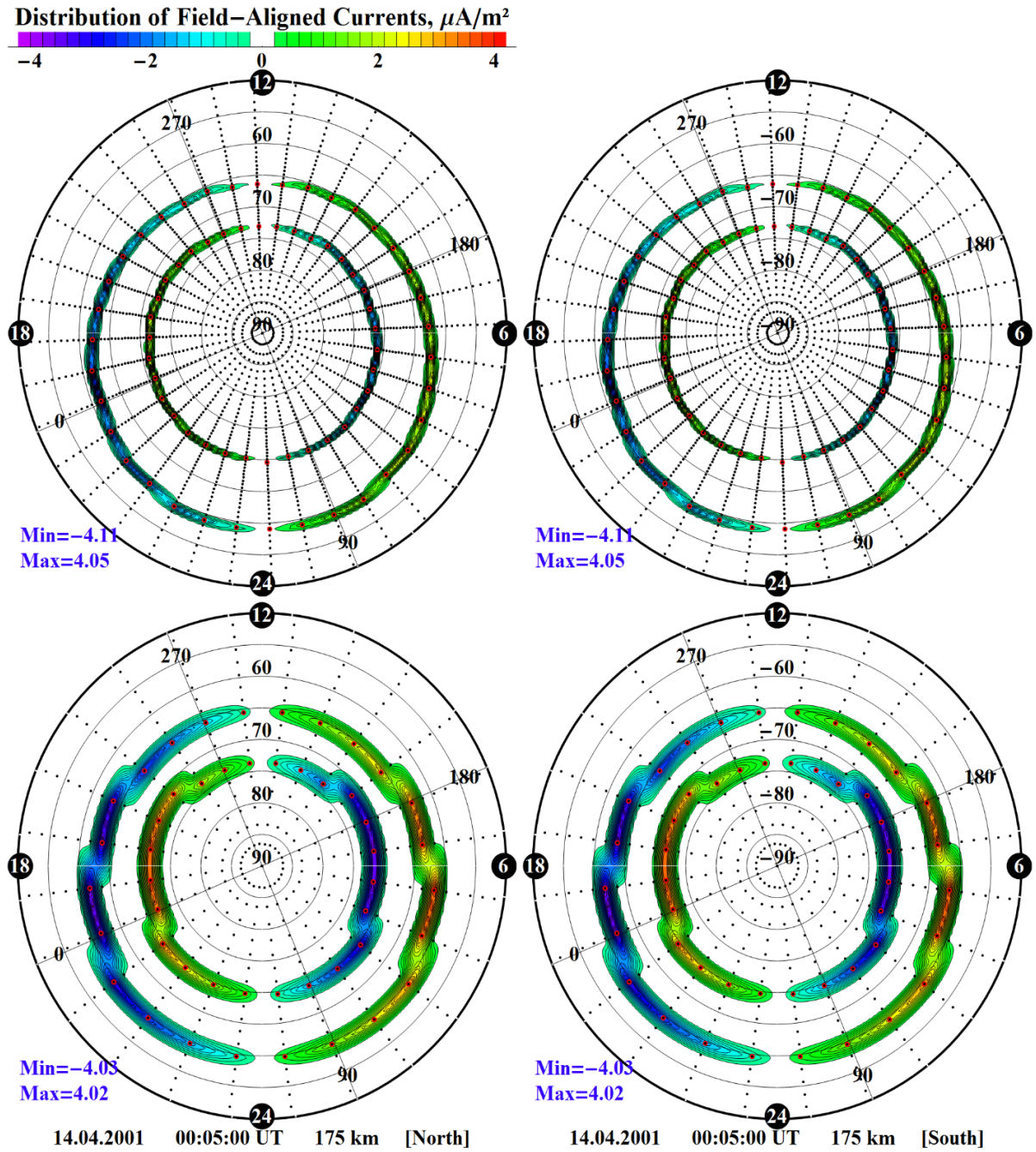
Figure 2.4. *An example of the FAC distributions for the Northern and Southern Hemispheres for different spatial grids. The distributions are obtained with the IPM model. The upward currents are positive (red), and the downward currents are negative (blue). Black points show the spatial grid nodes. Red points present the inner and outer boundaries of the auroral oval. The upper panel shows a high-resolution variable grid, while the lower panels show the standard equivalent grid scheme.*

The auroral area is shifted to the night side along the noon-midnight meridian (by about 4 deg.). The FAC system is represented by the Region 1 and Region 2 currents. Currents are located at the inner (Region 1) and outer (Region 2) boundaries of the auroral region. The red

dotted lines in Figure 2.4 show those boundaries. The boundary's position depends on the magnetic activity (Kp index in this version). They are moved equatorward with increasing magnetic activity. Together with it, these boundaries define the precipitation area (see Section 2.3.3).

The magnetospheric FAC system is defined along two boundary lines for each hemisphere. The Region 1 and Region 2 currents are located in one grid point for each longitude. But actually, they occupy an area between a few latitudinal steps, as it is indicated by the colored areas of the FAC distribution in Figure 2.4. Therefore, FAC distributions with the same current density provide different total currents (resulting in different cross polar cap potential drops) for different spatial grids. The solution to this problem is presented below (see Section 2.3.4).

2.3.2. The thermospheric wind dynamo currents

The contribution to the current system comes from the ionospheric thermospheric wind dynamo current. This current is calculated inside the UAM model. The thermospheric neutral wind is a driver for this dynamo current. During the simulation process, the thermospheric wind distribution calculated at the previous time step is used to obtain the dynamo current. This is done with the assumption that the distribution of the neutral wind does not significantly change during one time step. This current superposes (as a background) on the FAC system. An example of the ionospheric currents for the Northern and Southern polar regions is presented in Figure 2.5.
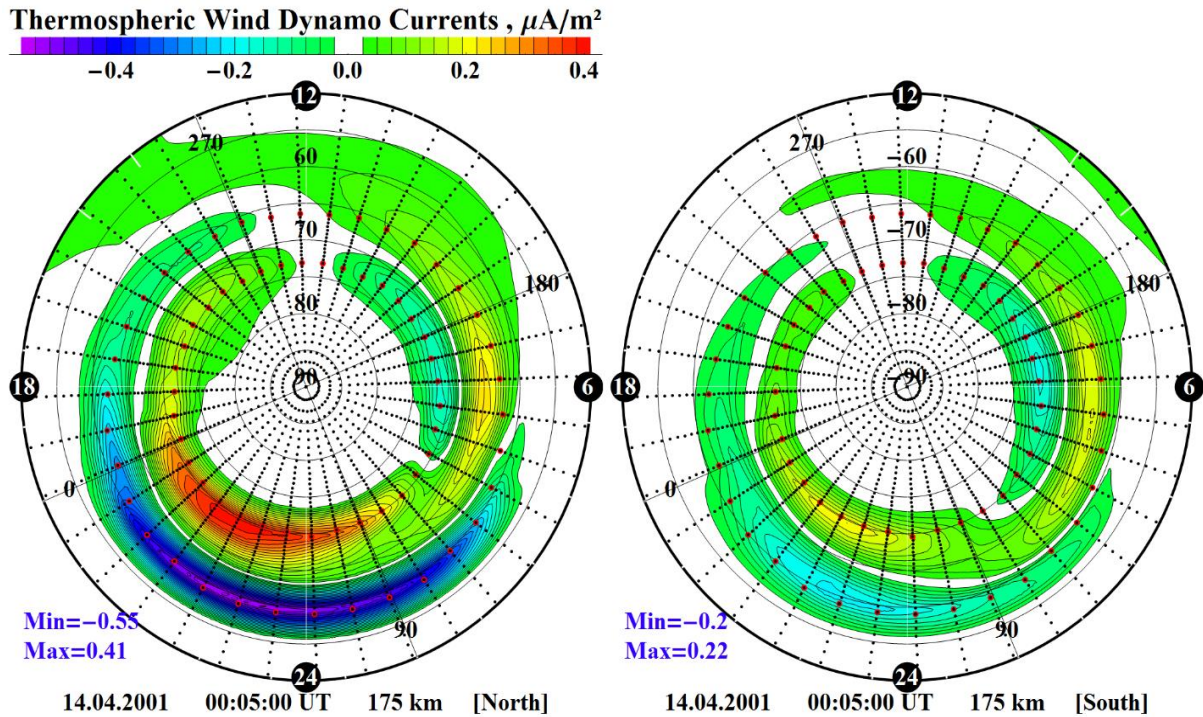
Figure 2.5. *The thermospheric wind dynamo current distribution obtained with the UAM model for the Northern winter (left) and Southern summer (right) Hemispheres. The patterns are shown in polar geomagnetic coordinates. The downward currents are negative (blue), and the upward currents are positive (red).*

In Figure 2.5, it is seen that the amplitude of the ionospheric currents is smaller than the magnitude of the magnetospheric currents (see Figure 2.4). In this example, the dynamo currents are about 10 times smaller than the FAC currents. The most significant impact takes place just prior to the midnight sector. Nevertheless, the dynamo current distribution is calculated globally as opposed to the FAC, which are limited by the boundaries of the auroral precipitation area (see Section 1.5). Because of this, the dynamo current can play a significant role. The impact of this source depends on many factors such as the season, UT time moment and geomagnetic activity. It is most significant during quiet time conditions.

The gradient of the electric field potential is the drive ions drift. The ion drift transfers via collisions energy to the neutral particles. In result, the electric field together with other drivers (such as for example a pressure gradient) generates the thermospheric neutral wind. On the other hand, the neutral wind is the driver for the dynamo currents. This is one of the examples, which manifests the feedback in the UAM model.

2.3.3. The auroral precipitations

The empirical model of **Hardy et al. [1985]** is used as input for the auroral precipitation. The model presents the energies of the precipitation fluxes, their intensities and positions in the dependence of the geomagnetic activity (Kp index – in this version). The precipitation leads to a region of higher conductivity (see Section 1.7).
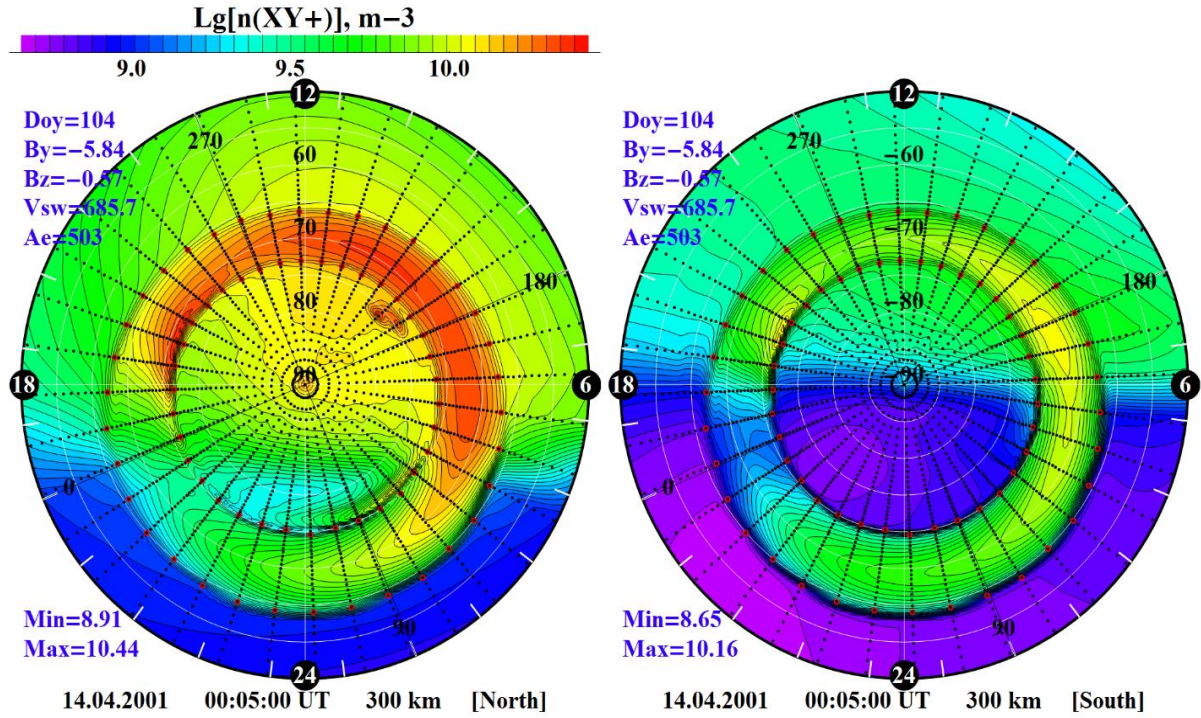
Figure 2.6. *The logarithm of molecular ion distribution at 300 km obtained with the UAM model for the Northern winter (left) and Southern summer (right) Hemispheres. The patterns are presented in the polar geomagnetic coordinate system. Black points show the spatial grid nodes. Red points present the inner and outer boundaries of the auroral oval.*

The molecular ion distribution is a direct result of the ionization due to the high-energy auroral particle precipitation. The precipitation area is located between the rings of the Region 1 and Region 2 currents. This area constitute the auroral oval, which is indicated by red dots for the inner and outer boundaries of the oval in Figure 2.6. The position of the precipitation flux maximum along each meridian is located in the center between the Regions 1 and 2 currents. These currents restrict the precipitation area. Outside this area, the auroral precipitations are zero. The UAM model uses a symmetric distribution of the auroral precipitation for both hemispheres.

The precipitation flux distributions for the Northern and Southern polar regions are the same, but the ion density distributions are different (see Figure 2.6). This is because of the different solar illumination (EUV) and neutral gas background conditions in the hemispheres.

The solar EUV provides significant additional ionization for the Northern polar region, while it is relatively small in the Southern polar region. Moreover, the hemispheres have different ionization backgrounds (neutral particle and temperature distributions).

2.3.4. The electric potential distribution

In the UAM model point of view the magnetospheric generator is a voltage generator. The required cross polar cap potential drop is, therefore, obtained by amplifying (reducing) the full distribution of the magnetospheric FAC system. An iteration process is used for this purpose. The basic logic of this method is, if cross-polar cap potential drop is smaller than required, the FAC coefficient is amplified by 30% in the opposite situation it is reduced by 30% (in an iterative manner). In result I obtained the cross polar cap potential drop with required accuracy (~5% or different).

Figure 2.7. *The electric field potential distribution calculated with the UAM model using the symmetrical FAC distribution for the Northern winter (left) and Southern summer (right) Hemispheres. The patterns are shown in a polar geomagnetic coordinates. Black points show the spatial grid nodes. Red points represent the inner and outer boundaries of the auroral region.*

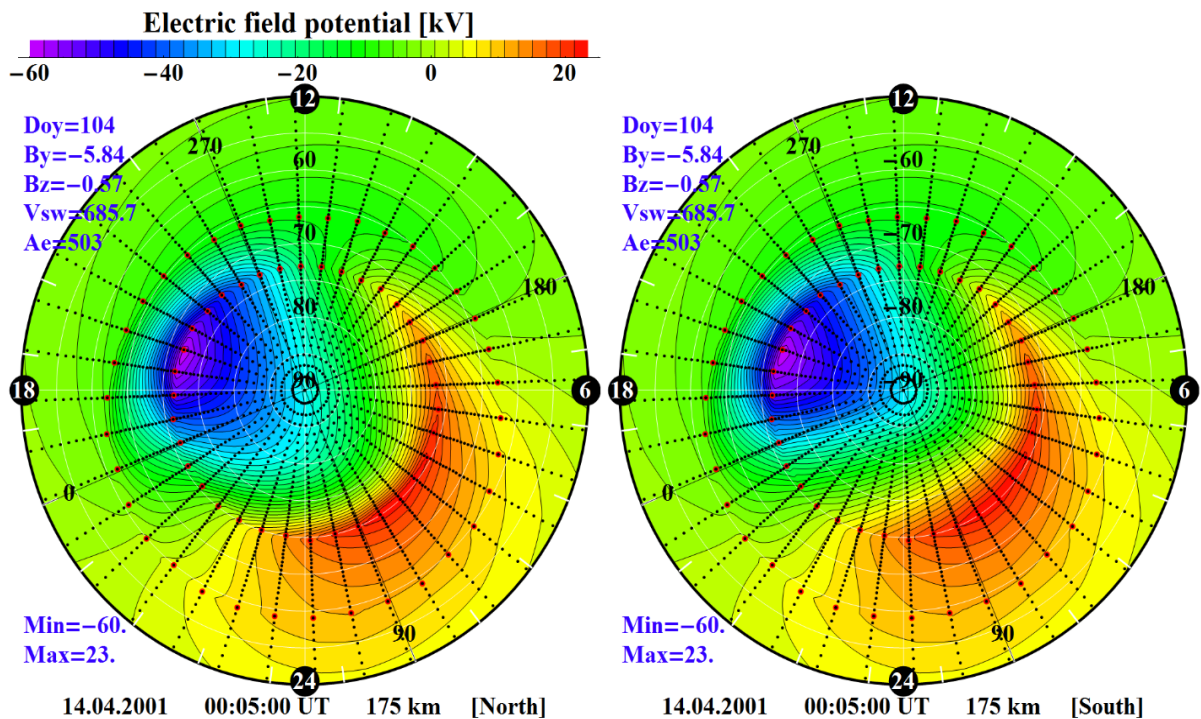In Figure 2.7 it is visible that the electric potential distributions have a mirror symmetry equatorward of the open/closed field line boundary (Region 1) for both hemispheres. A difference takes place only poleward the boundary, where the magnetic field-lines are open. This difference is not very significant.

The FAC distributions for the Northern and Southern Hemispheres are identical (magnitude and longitude position) according to the first assumption (see Section 2.3.1). In the UAM model, the following numerical scheme was used in order to solve the equation for the electric potential. For the closed field-lines, the FAC is the average value of the currents in both hemispheres. For the open field lines, the FAC are independent. In this version of the model, the Region 1 and Region 2 FACs are located in the area of closed field lines. Together with the second assumption (see Section 2.3.1), the standard version of the UAM model provides the identical positions and magnitudes of the minimum and maximum of the electric field potential for the Northern and Southern Hemispheres (full symmetry equatorward of the Region 1 FACs). In the real situation, the electric field potential distributions for the Northern and Southern Hemispheres should be different (see Figures 2.1 and 2.2).

To define the magnetospheric FAC system for the standard version it is sufficient to only describe the position of Region 1 and Region 2 FACs. The local time distributions are represented by the harmonic function (see Figure 2.3). The Region 1 and Region 2 FACs magnitudes are obtained by the iterative process (see Section 2.3.4) for required cross polar cap potential drop.

2.3.5. The CHAllenging Minisatellite Payload (CHAMP) satellite

The CHAMP was a small German satellite, which was developed and operated by the German Center of Geosciences in Potsdam. The satellite mission was started on July 15, 2000, into a near polar orbit with an inclination of 87.3 deg. and an initial altitude of 454 km *[Reigber et al., 2002]*. The end of the CHAMP satellite mission was at September 19, 2010, after 58277 orbits.

The CHAMP satellite measured various parameters of the upper atmosphere. In the present investigation the thermospheric neutral wind, neutral mass density *[Doornbos, et al. 2010]* and electron density measurements obtained from the satellite were used for a comparison with the UAM model results. The satellite observations were used as an etalon in the data comparison.

WIND, m/s [North Pole]

CHAMP   Jan 01 – Dec 31, 2003   H = 400 km
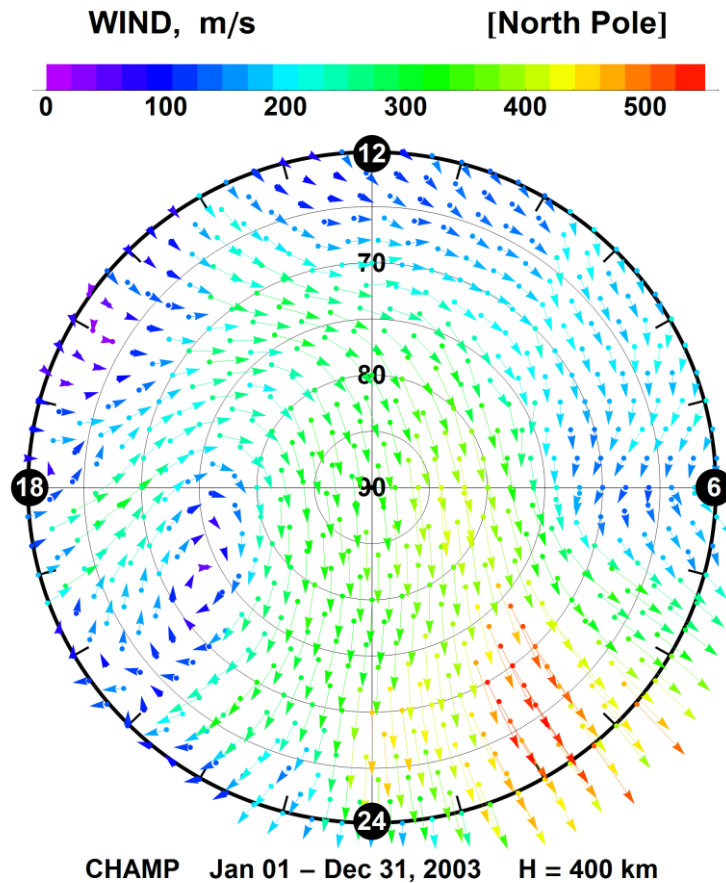
 Figure 2.8. *Average North Hemisphere thermospheric wind pattern given in polar geomagnetic coordinates (>60 deg magnetic latitude) at F-layer heights (400 km) using cross-track CHAMP accelerometer data of the full year 2003 as obtained from a recent European Space Agency (ESA) study [Doornbos et al. 2010]. The sun's position of the dial is at the top of the figure, with the dawn side on the right and the dusk side on the left. The wind direction is shown by the small vectors with the origin in the dots at the bin's position. Their length and color coding indicate the wind vector magnitude with the scale given on the top [Namgaladze et al. 2013].*

An example of the statistical thermospheric neutral wind distribution at 400 km for the Northern polar region obtained with the CHAMP accelerometer measurements is shown in Figure 2.8. The pattern was reconstructed using the satellite data collected during the year 2003. The satellite neutral wind observation clearly shows the vortex, which is located at the evening side. The morning side vortex is not pronounced so well. The noon – midnight stream is also visible. Maximum thermospheric neutral wind speed is about 550 m/s.

2.4. The UAM model with the dependence on IMF

2.4.1. Geomagnetic conditions

The time interval of October 28, 2003, 00 – 24 UT was selected for this study because together with a significant variation of the IMF orientation it comprises a period (05-11 UT) with a relatively "stable" IMF B_Y component (see Figure 2.9.). The IMF B_Y does not change significantly during that time.
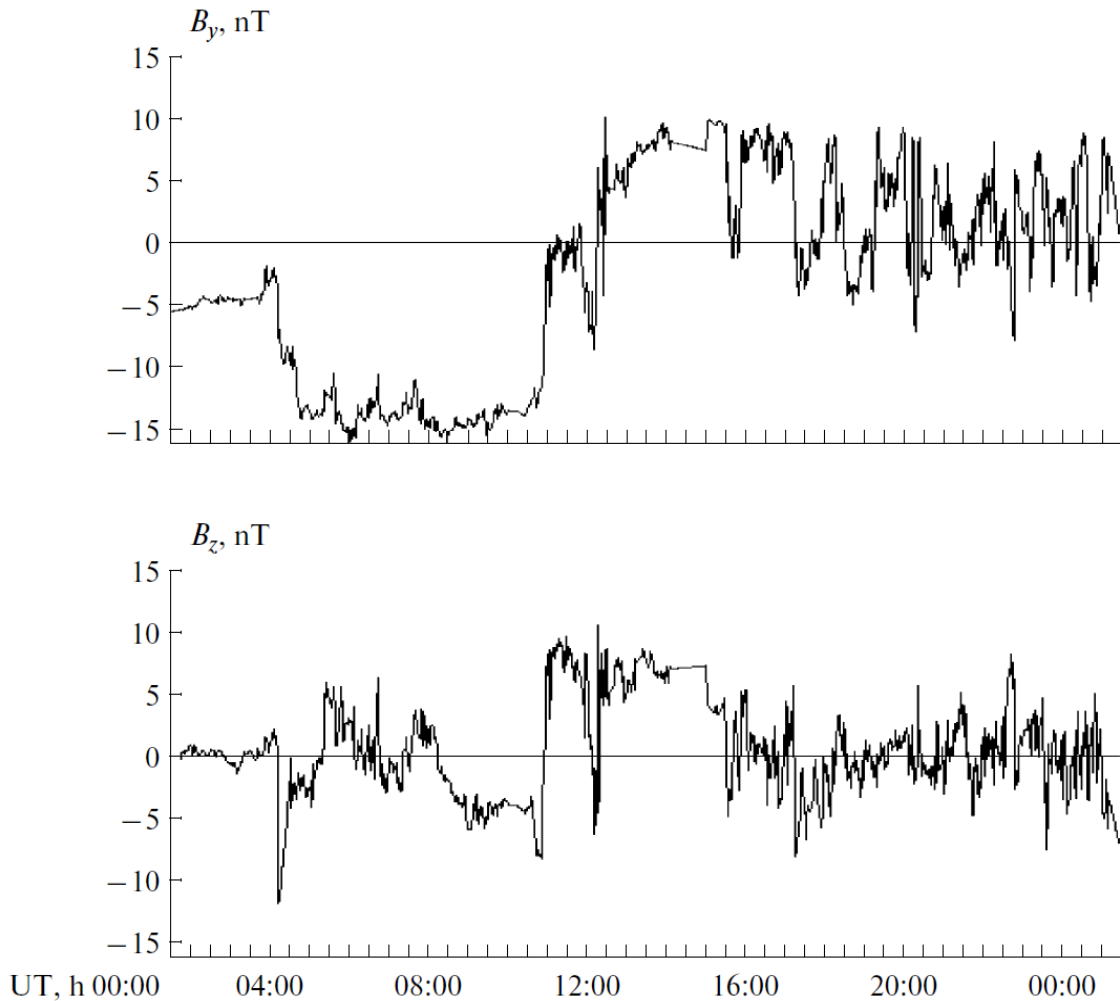
Figure 2.9. *The variations of the IMF B_Y (at the top) and IMF B_Z (at the bottom) components of interplanetary magnetic field on October 28, 2003 according to the Advanbced Composition Explorer (ACE) satellite data [**Förster et al. 2011b**].*

2.4.2. Electric potential distribution.
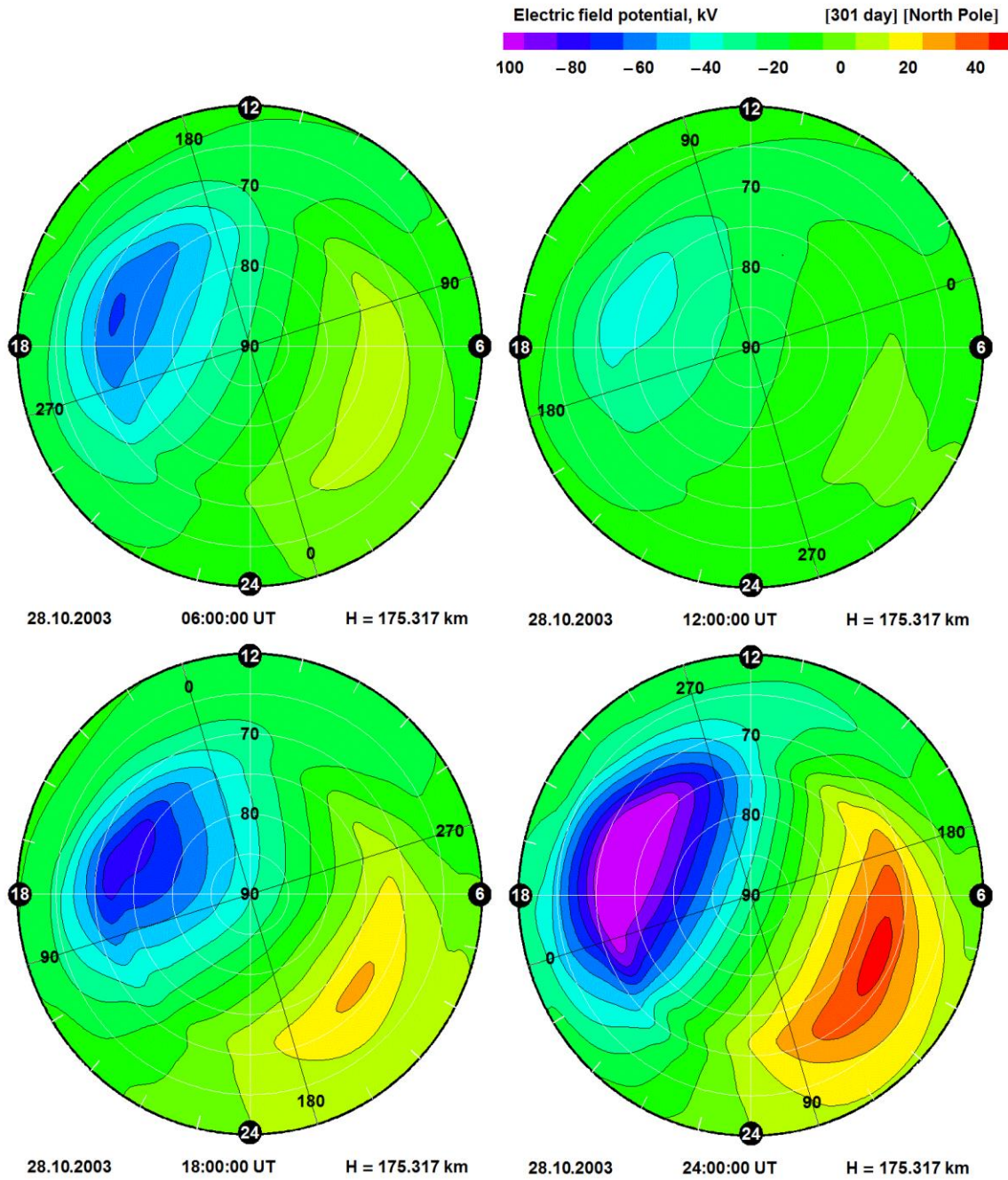
Figure 2.10. *Latitude-longitude electric field potential distributions in the polar geomagnetic coordinates at the latitudes higher than 60° (Northern Hemisphere) calculated using the UAM model at various universal time moments on October 28, 2003.* ***[Förster et al. 2011b]***

In Figure 2.10 the electric field potential distributions are shown only for the Northern Hemisphere. The Southern Hemisphere has the identical positions and magnitudes of the minimum and maximum of the electric field potential. This effect takes place because of the symmetrical distribution of the FAC system for the Southern and Northern polar regions. The

example represents only the variation of the cross polar cap potential drop with respect to the geomagnetic conditions.

2.4.3. Thermospheric neutral wind distribution
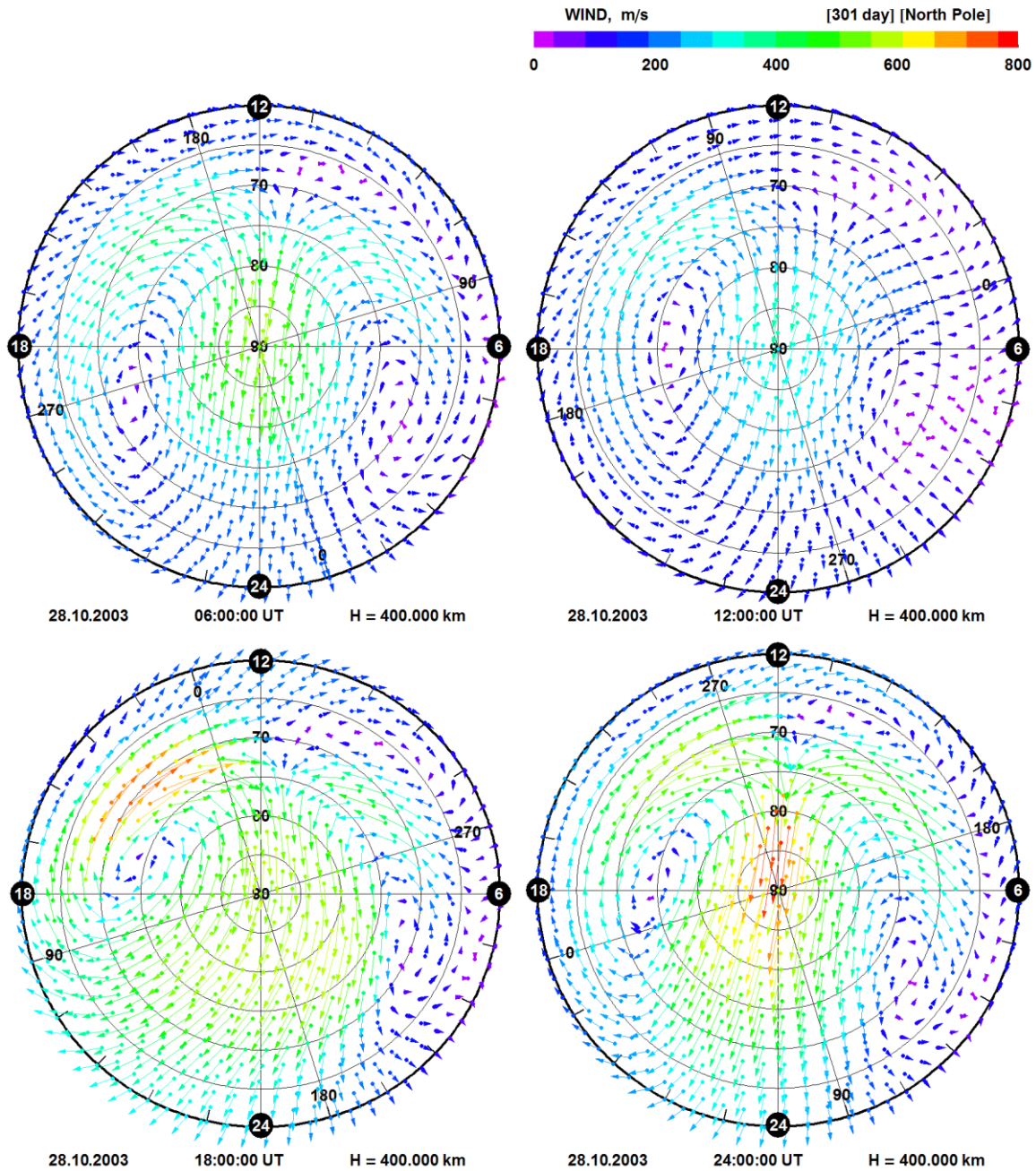
Figure 2.11. *Model calculations of the vector patterns of thermospheric wind circulation in polar geomagnetic coordinates at latitudes higher than 60° (Northern Hemisphere) at 400 km altitude for the same time moments as in Figure 2.10 performed using the UAM model. Maximum wind speed is 800 m/s.* **[Förster et al. 2011b]**

The thermospheric wind distributions at 400 km (CHAMP satellite altitude) obtained with the UAM model is shown in Figure 2.11. The time moments are the same as in Figure 2.10. The neutral wind vortices' areas are clearly seen in the evening and morning sides. The neutral wind distributions coincide with the electric potential patterns - the vortices positions and the amplitude - shown in Figure 2.10.

The patterns agreed well with the CHAMP satellite data presented in Figure 2.8 which include the magnitude and positions of the meso-scale structures such as the evening side vortex area. However, together with it, the modeling results show some difference with the satellite accelerometer measurements. For example, the morning vortices area is not so well pronounced in the CHAMP satellite data as in the theoretical simulation results. This difference takes place because of the different background of the data. The satellite pattern was constructed using one year of the CHAMP accelerometer measurements. Therefore, some variable parts, for example the morning vortex, were lost during a statistical data processing. On the other hand, the modeling result has peculiar features for each time moment. Those features depend on the highly variable geomagnetic conditions which are different for a various time moments. Because of this, the data comparison can be done only in general.

Alternatively, I performed a direct comparison between the UAM model result and the CHAMP satellite measurements to check the data quality. The examples of the data comparison during the polar overflights are presented in Figures 2.12 and 2.13.
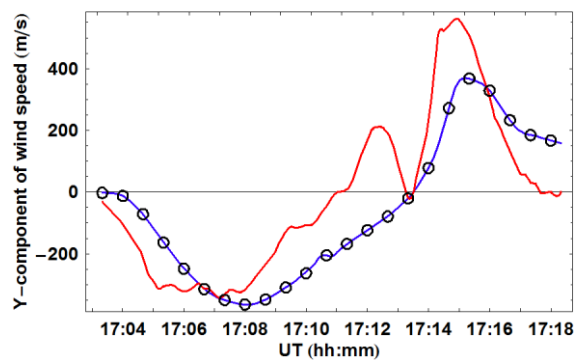
Figure 2.12. *Thermospheric crosswind speed variations at the altitude 400 km (October 28, 2003) according to the CHAMP satellite data along its flight trajectory (red curve without circles) and according to the UAM calculations (blue curve with circles).* **[Förster et al. 2011b]**

The CHAMP accelerometer provided the perpendicular (to the satellite flight direction) component of the thermospheric neutral wind. In this study, the CHAMP observation data are used with 10 second time resolution. The satellite overflight for the Northern polar regions are

shown in Figure 2.12. The CHAMP accelerometer measurements (red line) contain some small-scale fluctuations, while the UAM model presents more smooth results (blue line).

The time interval is 17:03 – 17:18 UT. The B_Y and B_Z components of the IMF are close to the zero value during this time interval (see Figure 2.9). The configuration of the electric potential distribution calculated with the UAM model (see Figure 2.10) agrees with the statistical distribution for the $B_Y = 0$ and $B_Z = 0$ (the electric field potential distributions are symmetrical for the Northern and Southern Hemispheres). This means that the geometry of the modeling electric field fits the actual situation. As a result, the UAM model shows good agreement with the satellite data for this overflight.

2.4.4. The modification of the electric field

The electric potential distribution has strong dependence on the IMF orientation as clearly seen in Figures 2.1 and 2.2. On the other hand, the UAM model with symmetric distribution of the FAC has no dependence on the IMF (see Figure 2.10).

I included the IMF dependence by the modification of the electric field. It was done in three stages. In the first stage, I ran the UAM model and saved the electric potential distribution at each modeling time step. In the second stage, I modified the electric potential patterns with respect to the IMF orientation (see description below). In the third stage, I ran the UAM model again with the modified electric potential distribution which was used as input parameter.
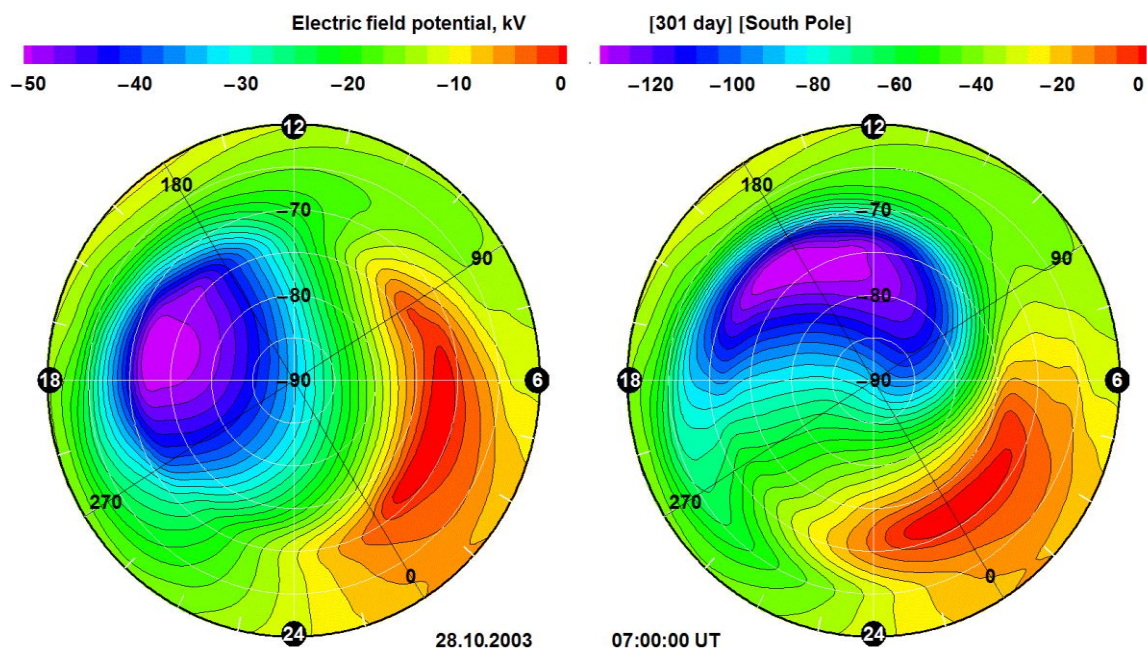
Figure 2.13. *An example of the electric potential distributions for the Southern polar region before (left panel) and after (right panel) modification. [Förster et al. 2011b]*

The IMF dependence was included to the UAM model by twisting the electric potential distribution at the polar areas. The patterns for the Northern and Southern Hemispheres were twisted in opposite directions in the Northern and Southern Hemispheres according to the IMF B_Y component. Together with it, I modified the cross polar cap potential drop according to the IMF orientation. The modification for the Southern polar region (07:00 UT) is shown in Figure 2.13; for the Northern polar region it is mirror symmetric (not shown here).
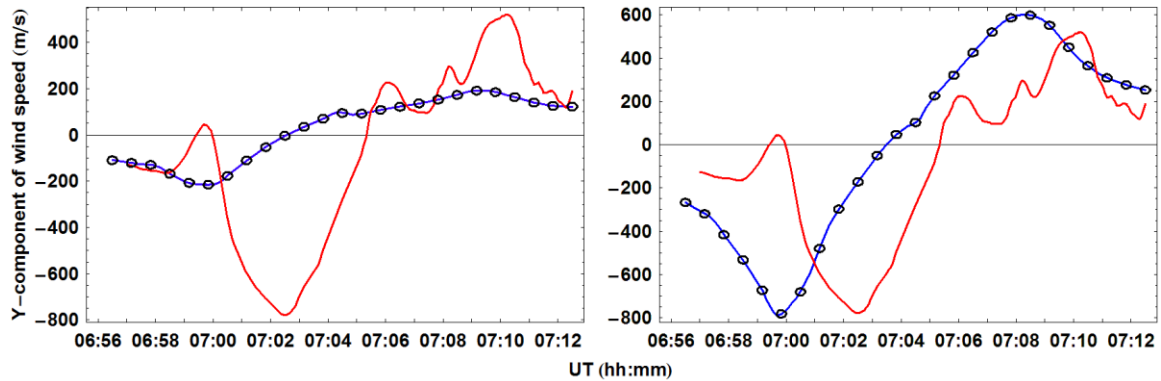
Figure 2.14. *Variations of thermospheric crosswind speed according to the CHAMP satellite data along its flight trajectory (curve without circles) and according to the UAM calculations (curve with circles) at the altitude 400 km calculated at 07:00:00 UT (October 28, 2003) with (on the right) and without (on the left) taking the B_Y interplanetary magnetic field component into account.* **[Förster et al. 2011b]**

The time interval is 06:56 – 07:12 UT. The Blue curve line with circles in Figure 2.14 (right panel) shows the thermospheric neutral wind calculated with the modified electric field potential distribution. The simulation results with none modified elect electric field is presented in the left panel.

For that time interval, the IMF B_Y component is negative (about -15 nT). The actual electric potential for this situation is significantly different from the modeling. As a result, the agreement between the satellite measurements and the simulation results is poor without including the dependence on the IMF orientation for this time as shown in the left panel. The amplification of the cross polar potential drop together with the twisting of the electric field significantly improved the UAM model prediction, enabling it to obtain the result similar to the CHAMP satellite measurement modeling data profile (right panel).

The small offset between the satellite accelerometer data and the modeling results (right panel) can be explained by the difference in coordinate systems (see Section 5.5). Also, the

satellite observation contains small scale variations, while the UAM model does not represent such features.

2.5. Conclusion

Including the IMF dependence to the UAM model, the MIT coupling dynamic system can be reproduced more realistically. This is clearly shown in Figure 2.14.

The method described above presents the way to include the dependence on the IMF orientation using a symmetrical FAC system (as a result of the symmetrical electric field) for the Northern and Southern polar regions. The electric field asymmetry between the hemispheres was obtained by twisting the pre-calculated patterns of the electric potential.

Based on this method, the pre-calculated electric field potential distribution was used as input parameter. The potential patterns became artificial. They were modified with respect to the IMF orientation, but had non-IMF background (originally they were symmetrical and calculated without the IMF dependence). This means that such manipulations with electric field are artificial.

To solve this problem, I used a system of FACs with IMF dependence (see Chapters 3 and 4) which allows the calculatint the electric field with respect to the IMF orientation, as well as keeping the self-consistency of the UAM model. Moreaver, the MIT couple dynamic system can be described more realistically through this approach.

3. Using the empirical field-aligned current model of Papitashvili

3.1. Introduction

The materials of this chapter are partially published in *Förster et al. [2012], Namgaladze et al. [2013]* and *Prokhorov et al., [2014]*. Some figures and tables are directly taken from these papers.

This part of my thesis is extention of a prior study (*Förster et al. [2011b]*). There, we undertook the successful improvement of the UAM model by including the dependence on IMF orientations. The dependence on IMF was included into the model by the direct modification of the electric field patterns. For this purpose, the electric potential distribution was calculated and saved for one particular reference interval. Then, the electric potential patterns were twisted for Southern and Northern Hemispheres in an asymmetrical way corresponding to the IMF B_Y variation. The modelling results for the thermospheric neutral wind was compared with thr CHAMP measurements. Such modified configuration of the electric field significantly improved the agreement between the simulation results and the satellite observations.

In this chapter, I describe the use of the empirical IMF dependent FAC model of *Papitashvili et al. [2002]* (PM) as input parameter for the UAM model. That configuration was used to investigate the MIT dynamic system at high-latitudes for various solar and geomagnetic activities, seasons and IMF strengths and orientations. For this purpose, I performed the simulations with the UAM model for various geomagnetic activities and solar wind/IMF conditions. The modeling intervals are presented in Table 3.1. To validate the modeling output, the simulation results for the thermospheric neutral wind, neutral mass density and electron density were compared with the CHAMP satellite measurements.

This was the first time I used an IMF-dependent FAC model as input parameter for the UAM model. In this version of the model the FAC distributions were different for the Northern and Southern Hemispheres. In the past, the system of the FAC in the UAM model was presented by the empirical FAC model of *Iijima and Potemra [1976] (IPM)*, which defined the Region 1 and Region 2 currents. The FAC systems were symmetric for the Northern and Southern Hemispheres and independent of the IMF values.

The study focuses on the high-latitude regions of the upper atmosphere. All figures are presented in a geomagnetic coordinates.

3.2. The UAM model modification with respect to the dependence on the IMF orientation

In Chapter 2 I described an UAM version that uses a symmetrical distribution of the FAC for the Northern and Southern Hemispheres (see Section 2.3). Such a configuration of the UAM model does not allow an asymmetry in the positions of the minima (maxima) of the electric field potential between the hemispheres. Such an asymmetry is associated with the variations of the IMF B_Y component as examplified in *Förster et al., [2011a]*.

To improve the UAM model by including the dependence on IMF orientation, I broke the symmetry in the electric potential distribution between the hemisphires. For that purpose, I used the following assumptions for the solution of the electric potential equation (Equation 1.20) in the new version of the UAM model:

1. The FAC systems are independent for the Northern and Southern polar regions. The system of the FAC is presented, as in the previous version, by two rings shifted to the night sector (along the noon – midnight meridian), which define the Region 1 and Region 2 currents. The Region 0 currents are added adjacent to the Region 1 currents at the poleward noon side (cusp area).

2. The boundary between the open and closed field lines is the position of the Region 2 currents. The magnetic field lines are closed till the Region 2 (including). The areas of the Region 1 and 0 currents are located on the open field lines.

Such assumptions provide a possibility to obtain different distributions of the electric field potential inside the polar regions for both hemispheres using an ideal dipole coordinate system. This configuration allows to model electric field effects with correspondence to the deformation of the Earth magnetic field (twisting of the high latitude magnetic field with respect to the B_Y component of the IMF). These assumptions are sufficient to model the patterns of electric potential with the dependence on the IMF conditions.

3.3. The empirical FAC model of Papitashvili

The empirical FAC model of Papitashvili (PM) is based on the high-precision magnetic field measurement obtained by the Ørsted and Magsat satellites. The model provides the FAC distribution for summer, winter and equinox conditions and with respect to the IMF strength and orientation. The PM model allows the mapping of the FAC patterns for IMF $|\mathbf{B}| \leq 12$ nT for the Northern and Southern Hemispheres. The model defines the FAC distributions in the geomagnetic latitude range of 50-90 deg. The input parameters of the PM model are the

magnitude and orientation of the IMF in the GSM coordinates (B$_Y$ and B$_Z$ components) and the season *[Papitashvili et al. 2002]*.
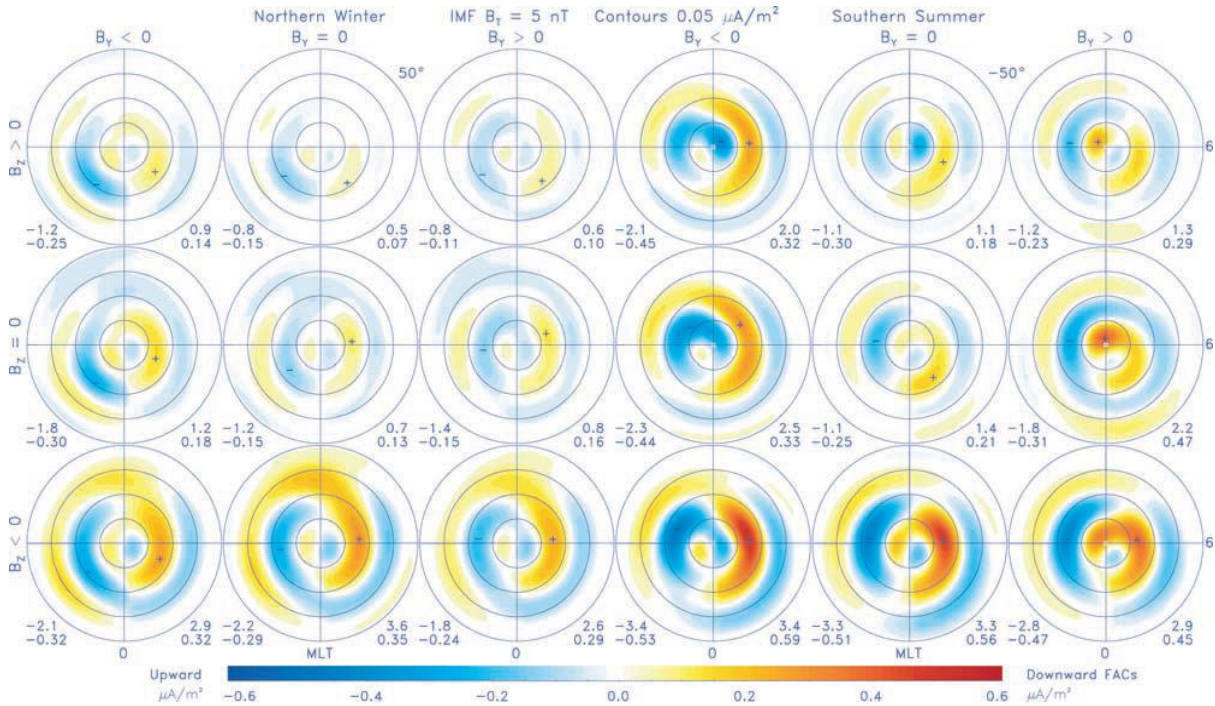
Figure 3.1. *Maps of field-aligned currents for B$_T$ = 5 nT organized by the IMF clock angle for northern winter (left) and southern summer (right). The central plots are the patterns for B$_T$ = 0. The total hemispherical currents (top numbers, MA) and the minimum and maximum current densities (lower numbers, mA/m^2) are marked at the bottom corners of each polar subplot. The upward currents are negative and the downward currents are positive. The FACs min/max density locations are identified by ''−'' and ''+'' [Papitashvili et al. 2002].*

Figures 3.1 shows the patterns of the FAC distribution for different IMF orientations for the Northern winter and Southern summer Hemispheres. The distributions are obtained with the empirical PM model using a magnitude B$_T$ = (B$_Y$^{2}+ B$_Z$^{2})$^{1/2}$ of 5 nT. The FACs of the Regions 1, 2 and 0 are clearly seen.

The whole system of the FACs is shifted to the night side along the noon-midnight meridian. The Region 1 currents comprise a ring structure with upward currents (out of the ionosphere) at the evening side and downward currents (into the ionosphere) at the morning side. The Region 2 currents are located equatorward of the Region 1 currents and present the outer ring (lower latitude) of the FAC system. The Region 2 currents have an opposite orientation (in comparison with Region 1 currents). The Region 0 currents are located near the pole (inside the ring of the Region 1 currents) and they are clearly visible in all panels.

A seasonal difference between the hemispheres is clearly seen. The magnitudes of the FACs for the Northern winter polar region are significantly weaker than those for the Southern summer polar region. The asymmetry in the FAC distribution with respect to the IMF orientation is also well visible.

3.4. Using the PM model as input parameter for the UAM model (adaptations & assumptions)

The model is organized with respect to the IMF orientation, especially for the $| B_T | \leq 5$ nT due to good data coverage. Because of this feature, the PM model is suitable for the simulation during quiet conditions and it is not massively useful for modeling storm and substorm events.

The PM model provides a smooth distribution of the FACs. That is not the case in real nature. The FAC system is highly variable and it is located in a narrow latitudinal area with a typical width of several kilometers. The smooth variation with latitude of the PM model is caused by the method used (spherical harmonics of 8th order) as well as the statistical origin of the model. The model represents an average value of a huge amount of measurements.

At the same time, the model reproduces additional currents near the equatorial boundary. Those currents look artificial and probably appear because of the use of spherical harmonic technique with artificial boundary conditions on the equatorial boundary.

Another important question is the relation between the FAC system and the auroral precipitation area. This is the area with higher conductivity. The precipitation fluxes increase the concentration of the ionized particles and the conductivity in the precipitation region. As a result, the conductivity grows inside the auroral area (see Figure 1.5). Any difference (even small) in space position between the current and precipitation patterns result in a significant effect of the electric field potential distribution due to Ohm's law. In other words, the same currents located inside and outside of the precipitation area - provide different electric field potential patterns of significant amount (several times) in the magnitude. To avoid this kind of disagreement, I implemented a strict positional agreement between the FAC and the auroral precipitation areas in this UAM model version.

Because of the features described above, the empirical PM model could not be used directly as input parameter for the UAM model. It required an adaptation as described below.
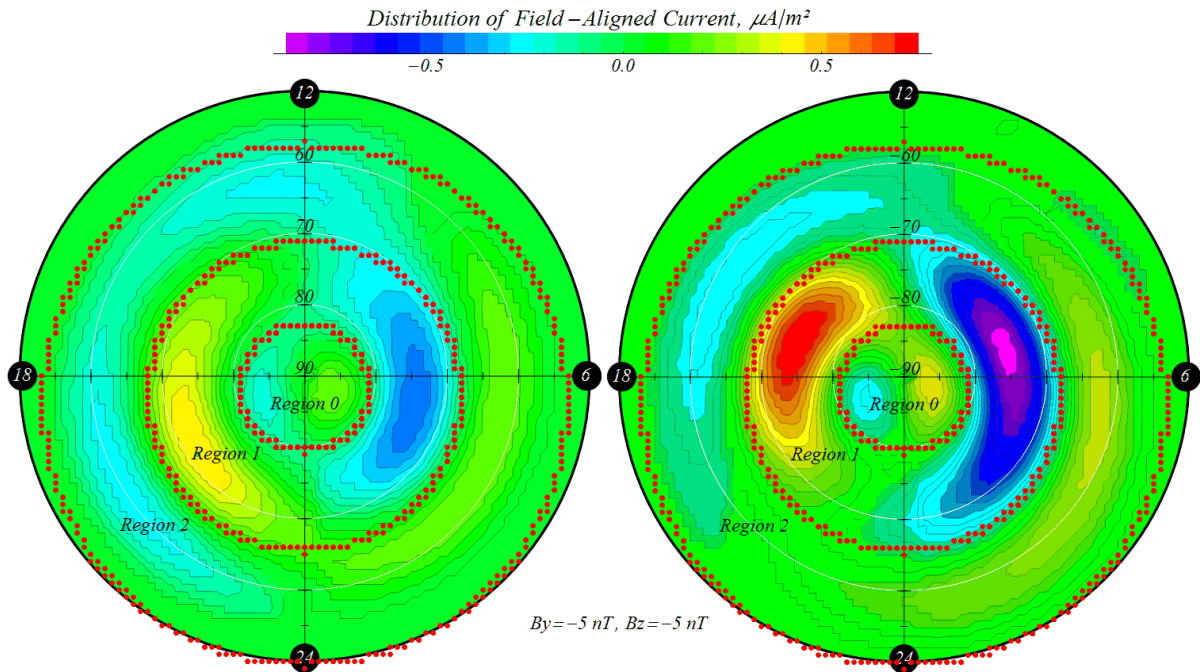
Figure 3.2. *An example of the statistical FAC distribution for the Northern winter (left panel) and Southern summer (right panel) Hemispheres obtained with the PM model. The red dot lines divide the polar areas into three zones: Region 1, 2 and 0. The downward currents are negative and the upward currents are positive. The patterns are shown in polar geomagnetic coordinates. The B_Y and B_Z components of the IMF are - 5 nT.*

The FAC system is focused along the auroral precipitation. For this purpose, I divided the FAC system into three parts: the areas of the Region 1, 2 and 0 currents (as shown in Figure 3.2). The currents are integrated inside the Region 1 and Region 2 areas along the meridians and inside the Region 0 area along the noon-midnight direction.

Such manipulation of the FAC system helps to exclude artificial currents near the equatorial boundaries of the PM model (they are located outside the integration area). Together with it, this division provides a clear separation of the FACs into the various zones. The result of this operation is presented below.
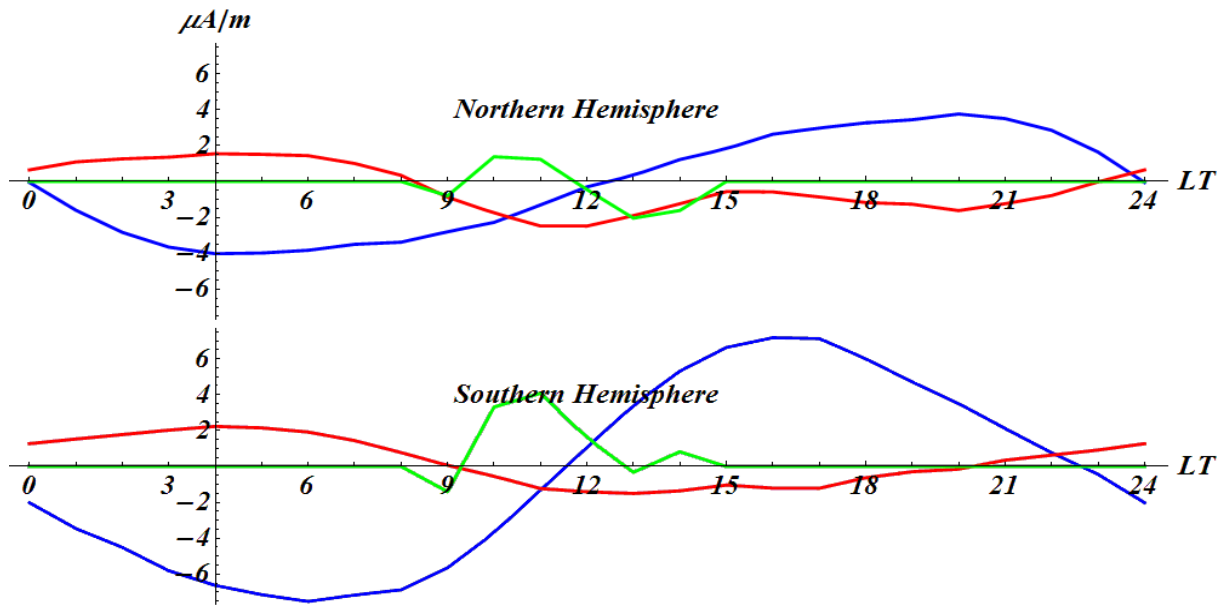
Figure 3.3. *The integrated FACs of the Region 1 (Blue), Region 2 (Red) and Region 0 (Green) currents for the Northern winter (top panel) and Southern summer (bottom panel) Hemispheres.*

In Figure 3.3 the integrated FACs illustrate the strong asymmetry between the Northern and Southern polar regions. The minima and maxima of the Region 1 currents are not located at the dawn – dusk meridian, as it was in the previous version. They are shifted instead by a few hours to the day side for the Northern and to the night side for the Southern Hemispheres. The difference between the winter and summer hemispheres in magnitude is clearly seen. This difference is about the factor of 2.
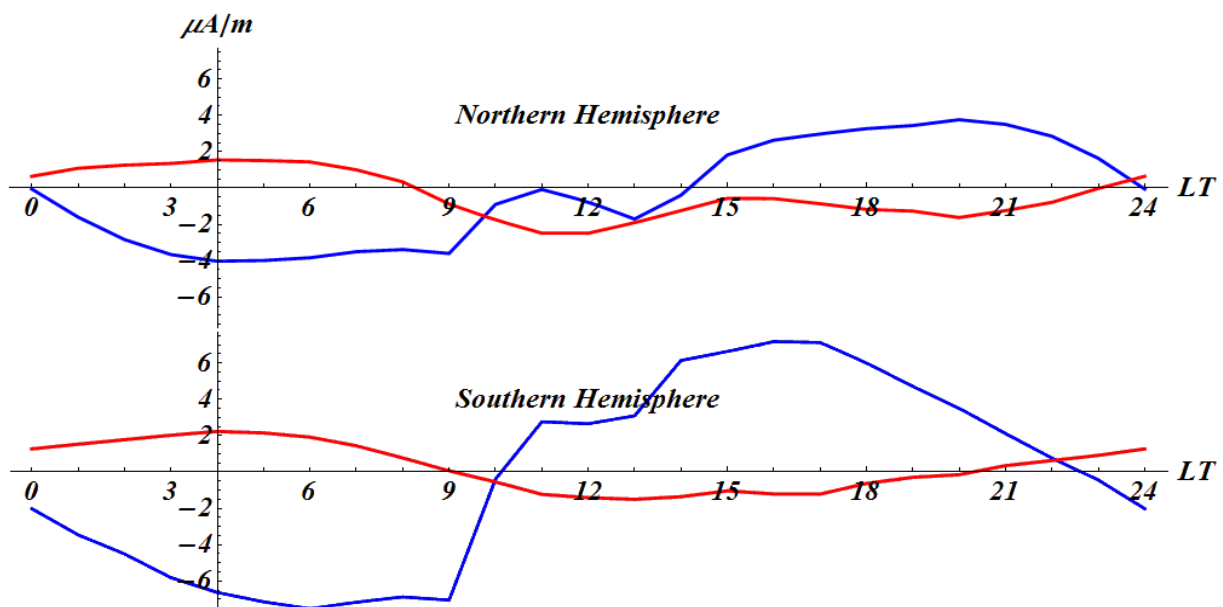
Figure 3.4. *The integrated FAC systems for the Northern winter (top panel) and Southern summer (bottom panel) Hemispheres. The superposition of the Region 1 and 0 currents is indicated by the blue color for the Region 1 and 0 currents and by the red color fort the Region 2 currents.*

The Region 1 and 2 currents for this specific version of the UAM model are located at the polar and equatorial boundaries of the auroral areas, respectively. The Region 0 currents are located adjacent to the Region 1 currents on the poleward side within the cusp near. According tot he model, the currents should be located inside the auroral area of higher conductivity (the precipitation area is defined in the area between the Region 1 and 2 currents), because of the significant difference in conductivity. In this version of the UAM model, I use a superposition of the Region 1 and 0 currents (see Figure 3.4). The Region 1 and 0 currents are located at the polar boundary of the auroral area.
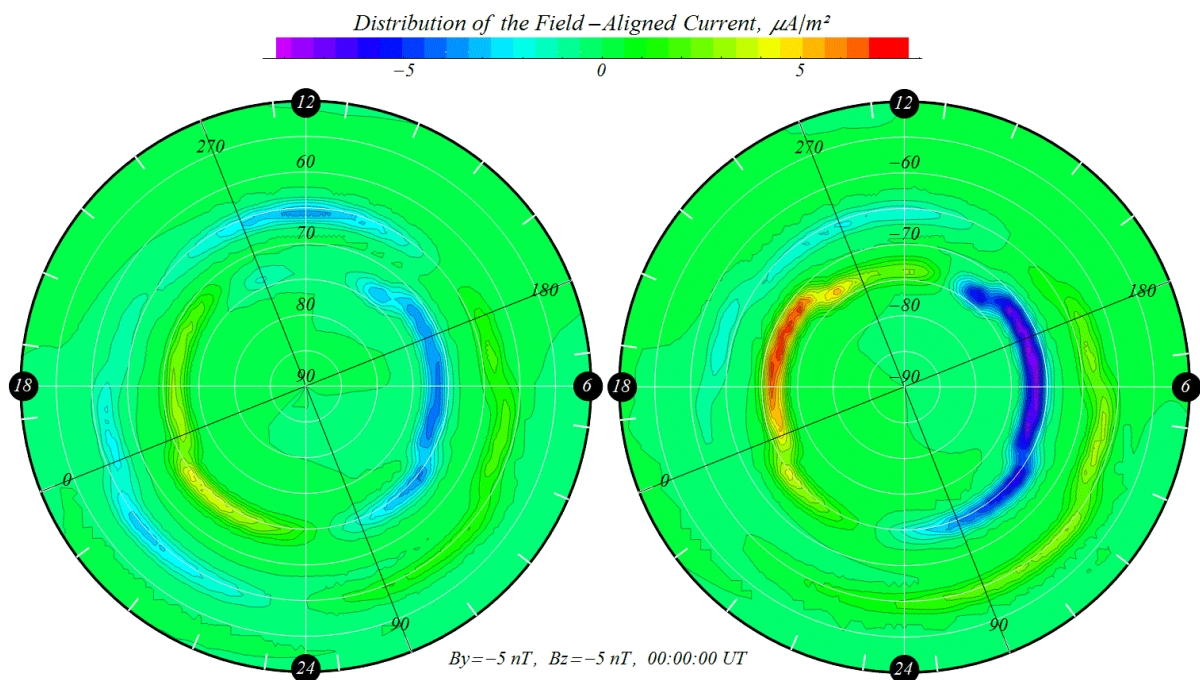
Figure 3.5. *The FAC distributions are obtained with the PM model for the Northern winter (left) and Southern summer (right) Hemispheres and adapted for the UAM model. The patterns are presented in the polar geomagnetic coordinate system. The B_Y and B_Z components of the IMF are - 5 nT. The downward currents are negative and the upward currents are positive.*

In Figure 3.5 the PM FAC system is adapted for the UAM model. The FACs are defined along the inner and outer boundaris of the auroral regions (similar to Figure 2.4, see Section 2.3.1). The superposition of the Region 1 and 0 currents is located at the inner boundary. The Region 2 currents are located at the outer boundary. The FAC distribution is for the same IMF conditions as shown in Figure 3.2.

3.5. The electric field potential

The electric field potential distribution is calculated by solving Equation 1.26. At the first step, the distributions of the internal neutral wind dynamo currents and the external magnetospheric currents (FACs) are found. The conductivity tensor is calculated from the neutral and charged particles composition. Now, the electric potential distribution can be calculated.
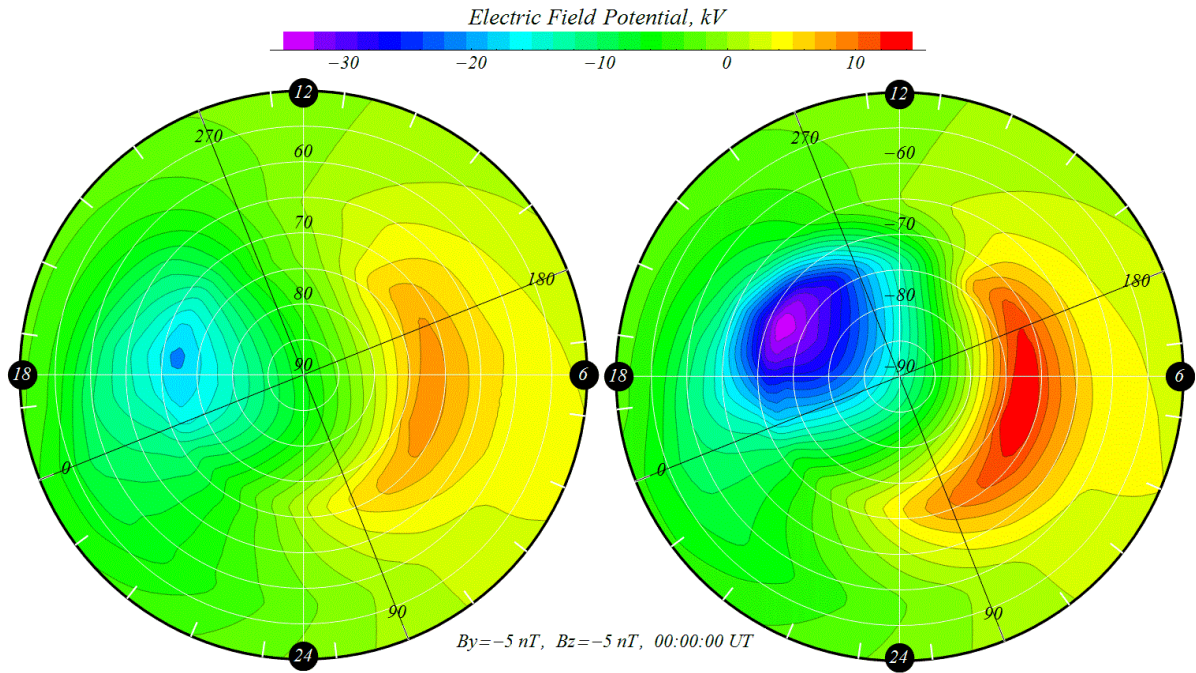
Figure 3.6. *The electric field potential distribution obtained with the UAM model for the Northern winter (left) and Southern summer (right) Hemispheres. The FAC system is calculated with the PM model. The patterns are presented in polar geomagnetic coordinates.*

The new model assumptions (see Section 3.2) lead to significant differences in the electric field potential distribution for the Northern and Southern polar regions. In Figure 3.6 the differences are clearly seen. They concern the magnitude of the cross polar cap potential drop, its position and the shape of the electric field potential patterns generally. An asymmetry between the hemispheres in the position of the minima and maxima is obvious.

As in the standard version of the UAM model, I use the assumption that the magnetospheric generator is a voltage generator. This configuration of the UAM model applies the same logic (an iterative manner) as described in Section 2.3.4, with one difference. In order to obtian the required cross polar cap potential drop, I use this iterative process in the new version of the UAM model independently for the Northern and Southern Hemispheres.
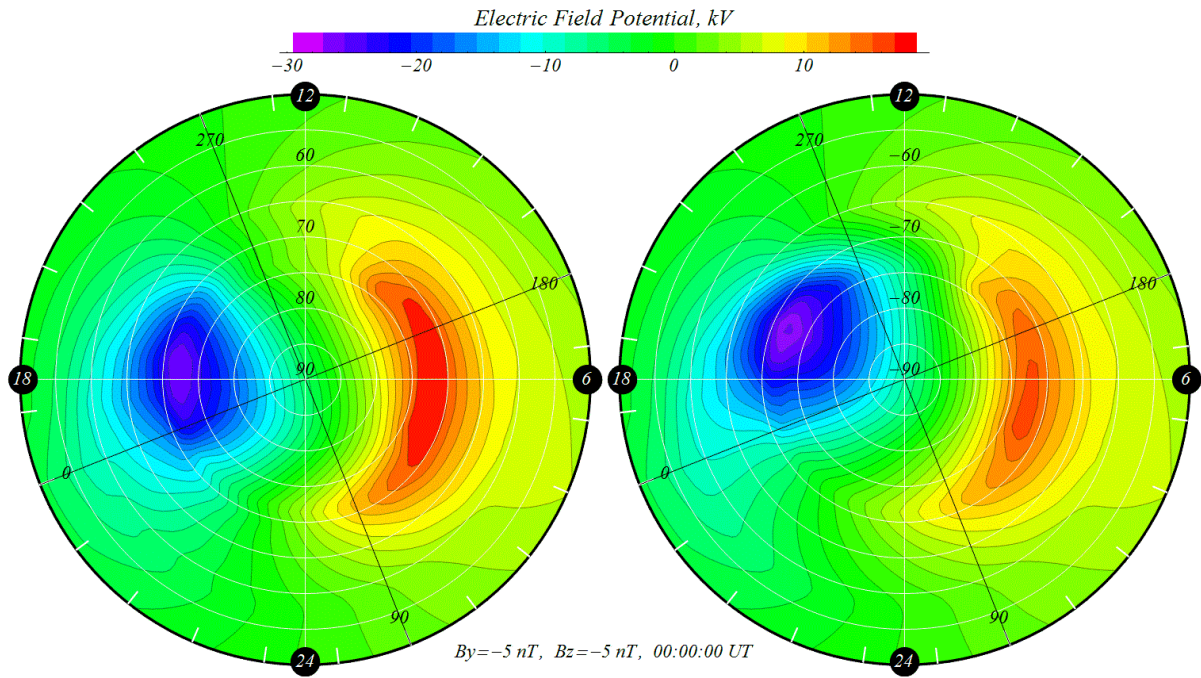
Figure 3.7. *The electric field potential distribution adapted for approximately equal cross polar cap potential drops for the Northern winter (left) and Southern summer (right) Hemispheres. The patterns are presented in polar geomagnetic coordinates.*

Figure 3.7 reveles that the resultant electric potential distribution is obtained as a result of this adaptation (iterative) procedure. The PM model is adapted and used as input parameter. The magnitudes of the FACs are modified with respect to the cross polar cap potential drop. The different resultant FACs for the Northern and Southern polar regions, together with the new position of the open/closed field lines boundary (see Section 2.3.4) for Equation 1.26, provides the asymmetrical electric potential for the hemispheres. This is clearly visible in the figure.

This adaptation scheme for the PM model is used in an automatic way during the calculation. As a result, the UAM model is provided with the PM FAC distributions as input parameters, which are dependent on the B_Y and B_Z components of the IMF. To extend the application area for higher activity conditions $|\mathbf{B_T}|>12$ nT (see Section 3.3), an extrapolation is used.

3.6. Modeling results and measurements

To quantify the modeling prediction quality, the simulation results are compared with the observations. The electric field potential distribution is compared with the CLUSTER EDI electric field measurements. Furthermore, the thermospheric neutral wind, neutral mass density and electron mass density results obtained with the UAM model are compared with the CHAMP satellite observations.

3.6.1. A comparison with the CLUSTER EDI measurements

At the first stage, I tested the algorithm of the electric field calculation. For this purpose, I reconstructed the electric field potential distributions of different sectors of the IMF. The PM model is used as input. The simulations are performed for summer, winter and equinox conditions. The modeling result for the Northern equinox Hemisphere is shown in Figures 3.8.
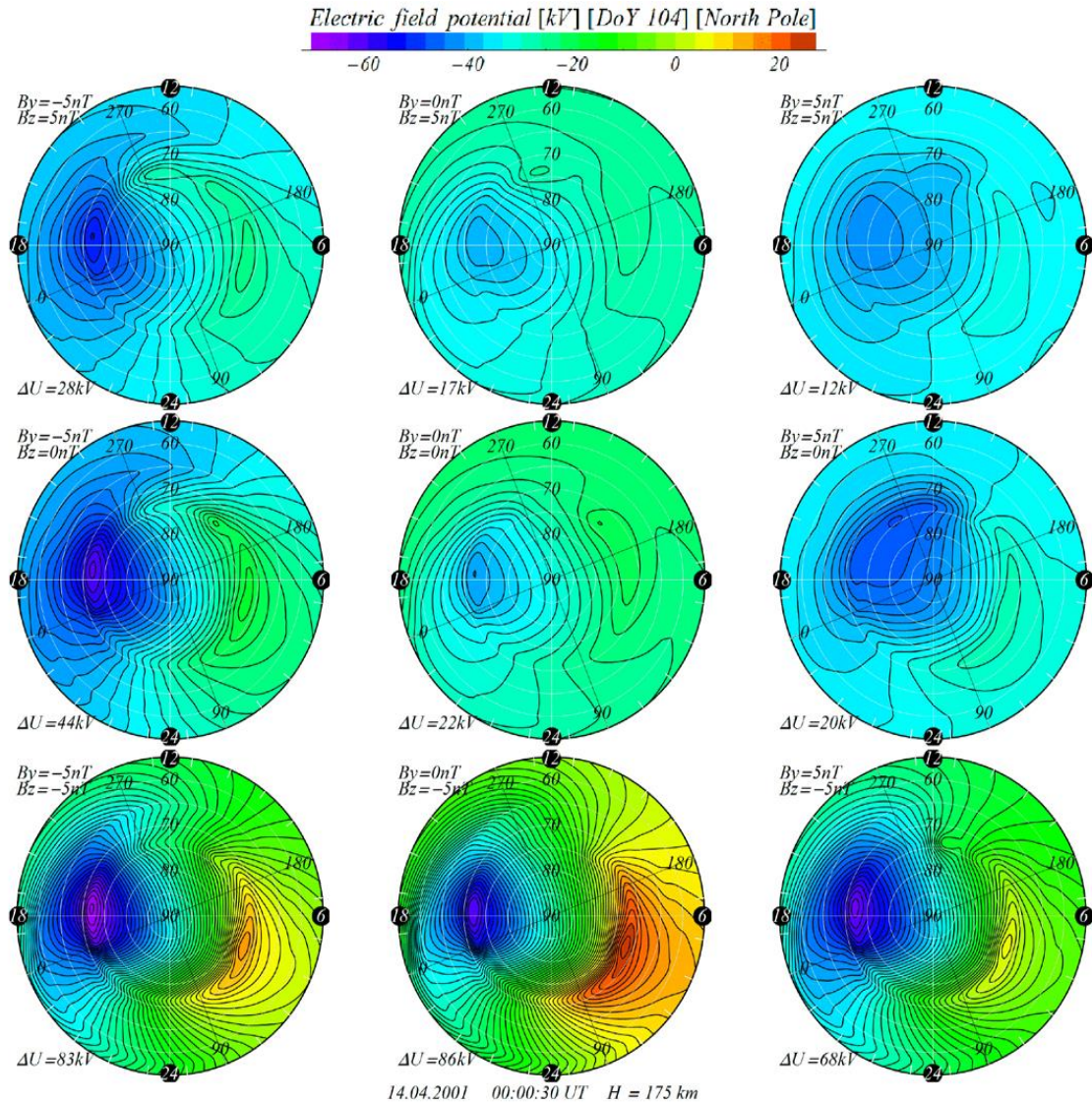
Figure 3.8. *The electric field potential distribution for the Northern equinox polar region obtained with the UAM model. The PM model is used as input. The patterns are presented for the 8 clock-angle orientations of the IMF. The central pattern shows additionaly the FAC distribution for $B_Y=0$ and $B_Z=0$, the so-called zero-state of the magnetosphere, supposedly with vanishing reconnection processes on the front side magnetosphere.*

The new configuration of the UAM model efficiently reproduces the general features of the statistical electric field potential distributions as presented in ***Haaland et al. [2007]***, which

were obtained using the Cluster electric field measurements with the electron drift instrument (see Figure 2.1).

The modelling electric field potential distributions show very good agreement with the statistical data. The UAM model reproduces similar minima and maxima values of the electric potential and also a similar geometry of the spatial distribution. This can be clearly seen by comparing Figures 3.8 and 2.1.

This comparison facilitates the examination of the modeling output. However, it is somehow incorrect because of several factors:

1. The statistical model is obtained from a huge amount of measurements sorted for the different IMF orientation. This is the average values of all those observations. As a result, many details are smoothed out. This statistical model does not represent seasonal and UT variations of the electric potential distribution.

2. On the other hand, the theoretical UAM model provides peculiar electric potential patterns for each time moment. The modeling result depends on season, UT, solar and geomagnetic conditions. At the same time, the modeling result has a significant dependence on "History". "History" here refers to the previous stage or temporal evolution of the upper atmosphere.

To calculate the electric field potential distribution, it is necessary to know the distribution of the internal (calculated) and external (input) parameters. In our case, the FAC system obtained with the PM model is the external parameter. The thermosphere wind dynamo currents and the tensor of conductivity are the internal parameters for the UAM model. The neutral wind distribution during the simulation is taken from the previous modeling time step (see Section 1.5.1). The thermospheric winds are calculated in the UAM model after the electric potential block, as well as the other parameters of the neutral atmosphere. The conductivity tensor and neutral wind do not change very rapidly. Therefore, they have strong dependence on the previous stage of the upper atmosphere.

In Figure 3.8, for example, the nine electric potential distributions obtained with the UAM model for the different IMF orientations have the same "History" and represent the UAM model reply on different FAC distributions only.

In any case, the UAM model shows very good results, which are in good accordance with the Cluster EDI measurements. The conclusion for this stage is, it is possible to obtain correct electric field potential distributions using the UAM model with the FAC calculated by the PM model.

3.6.2. A comparison with the CHAMP satellite measurements

3.6.2.1. Time intervals

The main idea of this stage of testing the UAM model with respect to the IMF dependence consist in a comparison with the satellite data. For that purpose, the new configuration of the UAM model was tested under various geomagnetic conditions (see Table 3.1). The obtained results were compared with the CHAMP satellite measurements. This investigation led to the quantification of the modeling predictions.

№	Date [dd.mm.yyyy]	Stable [hh-hh]	Unstable [hh-hh]	By [nT]	Bz [nT]	Kp (3-hourly)	$F_{10.7}$
1	14.04.2001	00-11	12-24	-7.2	-1.3	4+ 4- 3+ 3+ 3+ 3+ 3- 2o	181.0
2	25.05.2002	00-12	13-24	6.3	4.0	1- 0+ 0+ 0+ 1+ 2o 1+ 1o	187.4
3	18.11.2002	00-24	No Data	6.4	-5.6	3o 2o 2- 1+ 2+ 2o 3o 3o	174.8
4	01.02.2003	00-14	15-24	-9.2	-1.2	3o 2o 1- 1- 1+ 3- 5- 4+	122.1
5	23.10.2003	00-21	22-24	-0.6	6.7	2- 3+ 3- 3- 3o 4- 3o 4o	141.7
6	30.08.2004	08-22	00-07;23-24	3.0	-10.2	2+ 2o 3+ 4o 4o 6- 5o 7o	91.6
7	13.09.2004	00-21	22-24	-8.4	2.2	0o 0o 0o 0+ 0o 0+ 4+ 4+	119.1
8	06.10.2004	13-22	00-12;23-24	4.0	-1.0	1o 2- 1+ 1o 0o 0o 0+ 0+	92.0
9	10.12.2004	09-21	00-08;22-24	7.6	-2.4	2o 2+ 2o 2o 2+ 3o 2+ 3o	82.3
10	13.06.2005	00-14	15-24	9.8	-6.9	6o 6- 4+ 3o 4o 3- 3+ 2-	94.7
11	02.11.2006	00-08	09-24	4.0	-1.3	2+ 2o 1o 1o 2- 3- 3o 2+	86.8

Table 3.1. *Time intervals of stable IMF conditions for various seasons and activities* **[Prokhorov et al. 2014]**.

The time intervals shown in Table 3.1 represent periods of different seasons and under various geomagnetic conditions and IMF orientations. The year range is 2001-2006. The intervals are from various phases of the solar cycle with F10.7 values in the range of 82.2-187.4. Some of them, for example, the 30th of April 2006 are geomagnetically quiet (Kp is about 0). Others are disturbed such as the 30th of August 2004 (Kp is about 7).

All these 11 time intervals presented in Table 3.1 were specifically selected as the periods that include several hours without significant variations of the IMF. These time periods are called "stable". They are shown in the 3rd column. The B_Y and B_Z components of the IMF for these time periods are presented in the 5th and 6th columns, respectively. The intervals also comprise likewise also more variable time periods - adjacent to the "stable" periods. Those periods are called "unstable". They are noted in the 4th column.

3.6.2.2. The UAM model runs

The UAM model was tested under various strengths/orientations of the IMF and geomagnetic activities (see Table 3.1). The FAC distribution obtained with the PM model was used as input parameter for the UAM model. The UAM model was run for 24 hours for each of the time intervals presented in Table 3.1 with the geomagnetic conditions of that date. The simulated results were sorted for each day into the following four groups: "stable" and "unstable" intervals for the Northern and Southern polar areas, respectively.

A few examples for the thermospheric neutral wind, neutral mass density and electron density obtained with the UAM model are shown below. The results are presented together with their detailed descriptions and a comparison with the CHAMP satellite measurements.

3.6.2.3. The thermospheric neutral wind

One of the most important parameters of the neutral atmosphere is the neutral thermospheric wind. The $\mathbf{E} \times \mathbf{B}$ plasma drift (together with EUV, heating, etc.) transmits energy to the neutral particles via collisions (ion drug). The thermospheric neutral wind is the result of this MIT interaction. At the same time, the neutral wind generates the system of the thermospheric dynamo currents. Those dynamo currents are part of the Earth's environment electrodynamic system and play a role in the electric field formation. This is one of the examples of the complex MIT dynamic coupling.
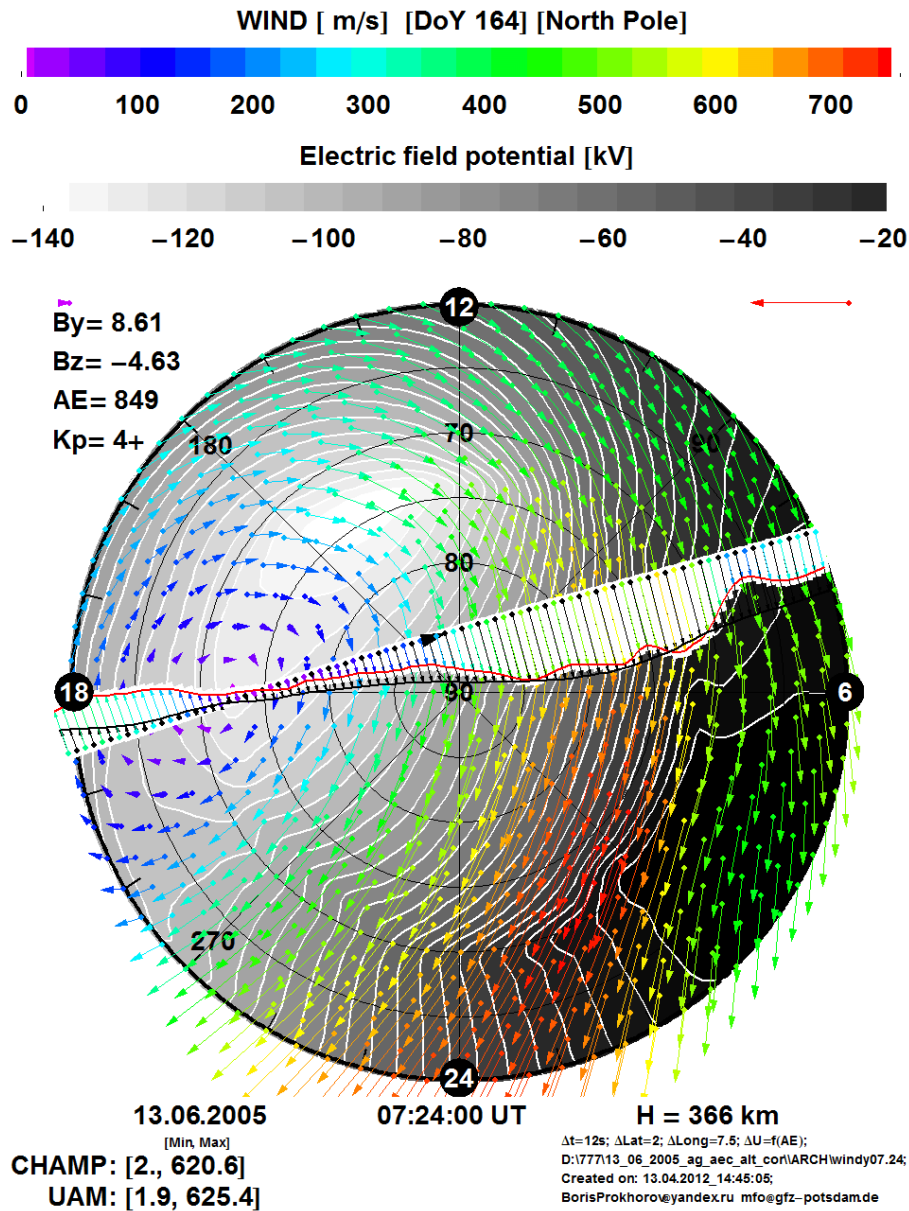
Figure 3.9. *A comparison of the UAM model result with the cross-track accelerometer measurements of the CHAMP satellite during the flight over the Northern Hemisphere for 13th of June 2005 07:24 UT.*

Figure 3.9 shows the UAM model neutral wind vector pattern by coloured arrows according to the colour scale on the top. The distribution of the electric potential is presented in the background in a black & white colour scale. The CHAMP cross-track measurement data are presented by the coloured arrows on the white background and bordered by a red line. The projection on the cross-track satellite direction of the UAM wind data is presented by a black arrows and bordered by a black line. The satellite position and flight direction are shown by black triangular sing. Points illustrate the position of the CHAMP before and after the time moment 07:24:00 UT.

In this study, I use satellite accelerometer measurements with 10 second time resolution. The modelling data is saved with a 1-minute time interval. I suppose that the neutral wind distribution does not change significantly during the 1-minute time interval. Therefore, I can use the modeling results for the same time moment to perform a comparison with 6 satellite data points. This means that for example the modeling time moment 07:24:00 is used for comparison with satellite data points within the following interval: 07:23:40 - 07:24:30 UT. The background wind pattern is given (only) for the six points around the current satellite position. The data for the other points are the modeling data of previous and later time moments, respectively. The satellite crosses the polar region during ~16 minutes, therefore the data are taken from ~16 different wind patterns. Nevertheless, the final result coincides well with the background thermospheric wind distribution. This means that the neutral wind does not change significantly during the CHAMP flight over the polar region due to the dominating inertial forces.

The evening neutral wind vortex is clearly seen, while the morning vortex is only presented as a slight deflection of the neutral wind flow in the figure. The strong noon – midnight stream (shifted to the morning side) is also clearly visible. The result itself implicates a fairly well agreement between the UAM modeling data and the satellite measurements.

3.6.2.4. The neutral mass density

Another important parameter of neutral atmosphere is the neutral mass density. This parameter describes the composition and space distribution of neutral particles in the upper atmosphere. The CHAMP satellite was measured this parameter with a very good accuracy. One example of the comparison between the UAM model and the CHAMP neutral mass density data is given below in Figure 3.10:

NEUTRAL MASS DENSITY [kg/ m−3] [DoY 164] [North Pole]
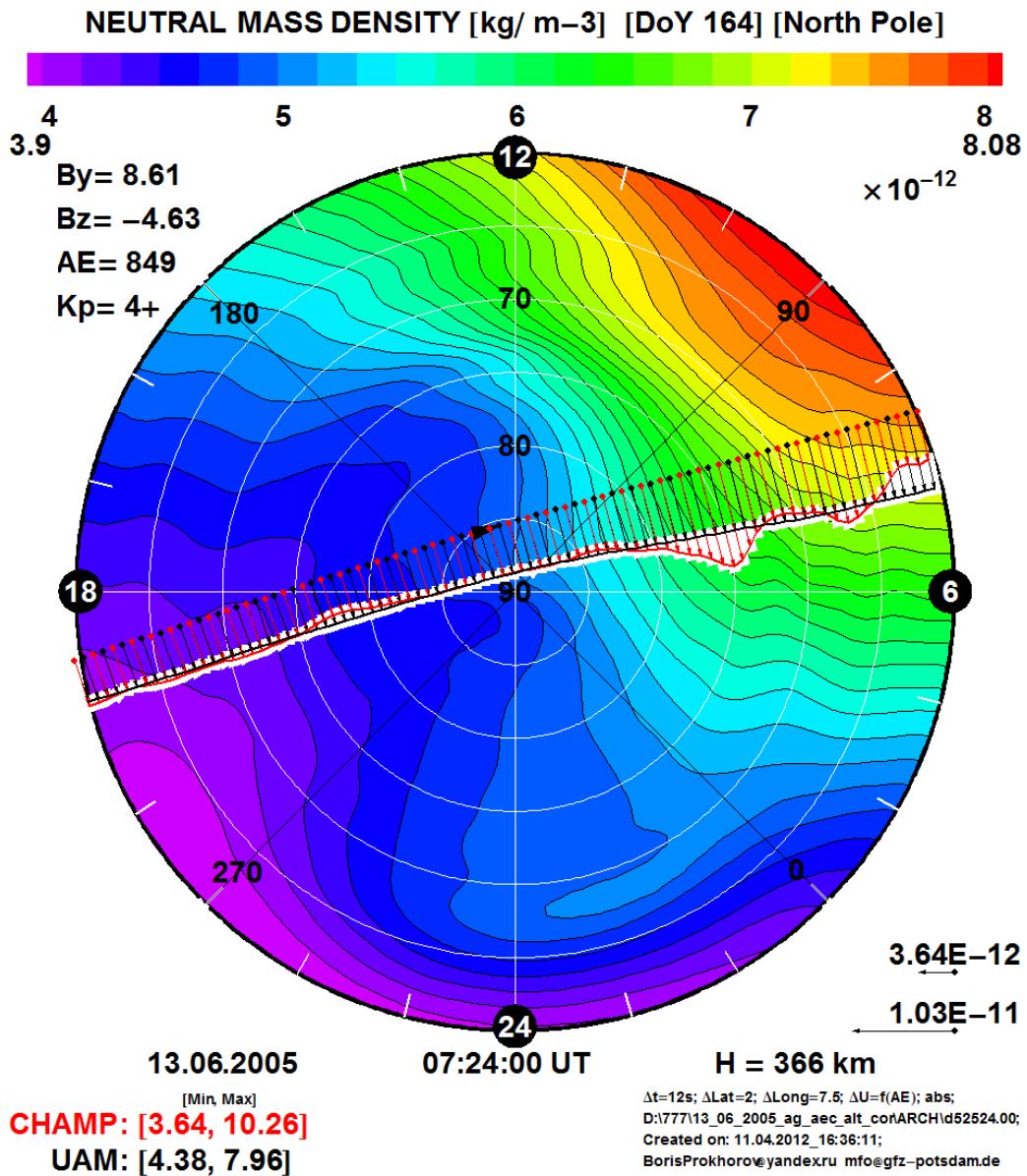
Figure 3.10. *Comparison of the UAM model result with the CHAMP accelerometer neutral mass density measurements. Flight over the Northern Hemisphere on 13th of June 2005 07:24 UT.*

The neutral mass density calculated by UAM model is presented in Figure 3.10 as a contour plot in the polar geomagnetic coordinates. The CHAMP accelerometer measurements are shown by red arrows and bordered by a red line. The UAM data are indicated by black arrows and bordered by a black line. The difference between the modeling data and the measurements is shown by the area with a white background. The satellite position and flight direction are shown by a black triangular sign. Points display the position of the CHAMP trajectory before and after the time moment 07:24:00 UT.

The CHAMP has a small variation in altitude satellite orbit of ~30km (see Figure 3.11). The neutral mass density is very sensitive for such a variation because of its strong, exponential

height variation according to the barometric law. This means that a difference in 30 km near an altitude of 360 km results in a difference in density in two times. Because of this, the modeling data presented by the black arrows in Figure 3.10 are adapted for the satellite altitude. The altitude of 366 km, given on the plot, is valid for the current satellite position and the contour plot.
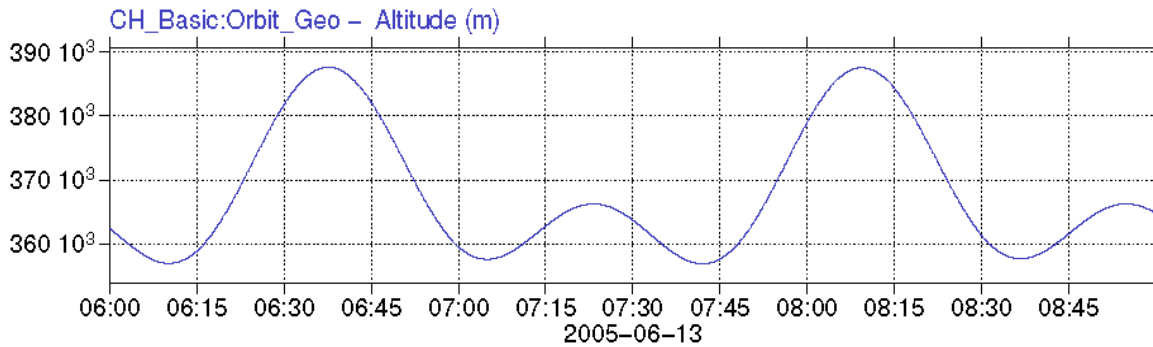
Figure 3.11. *Three hours of CHAMP altitude variation. The data was taken from: http://thermosphere.tudelft.nl/acceldrag/data.php*

The comparison of modelling neutral mass density data and the CHAMP observation data results in a very good agreement and with only occasional small differences. There are some-small scale fluctuations that are not reproduced by the model. They constitute in the upper atmosphere or some instabilities which take place during the measurements.

3.6.2.5. The electron density

The electron density is also a very important parameter of the upper atmosphere. The electron density in the polar region is important, for example, for the tensor of conductivity. The most interesting areas are the cusp and aurora regions itself, where precipitations are predominante. Therefore, I selected it as an example for the time moment, where the satellite passes over the cusp region. The comparison between the modeling result and the CHAMP date is illustrated in Figure 3.12.

Figure 3.12. *Comparison of the UAM model result with the CHAMP electron density measurements. Overflight over the Southern Hemisphere on 30th of August 2004 19:24 UT.*

The electron density calculated by the UAM model is illustrated in Figure 3.12 as a contour plot in a logarithmic scale in the polar geomagnetic coordinate system. The CHAMP measurement data are presented by red arrows and bordered by a red line. The UAM data are presented by black arrows and bordered by a black line. The difference between the modeling data and measurements is highlighted by a white background. The satellite position and flight direction are illustrated by a black triangular sing. Points shows the position of the CHAMP trajectory before and after the time moment 19:24:00 UT.

The modelling data in Figure 3.12 are presented in the same style the neutral mass density is presented in the previous plot (see Figure 3.10).

An enhancement of the electron density is clearly visible in the auroral precipitation area. The solar EUV provides additional electron density in the noon sector. The difference between the observation and the model results is very small.

3.7. Conclusion

The result of the comparison between the UAM model run with an additional IMF input and the CHAMP accelerometer measurements of the thermospheric neutral wind, neutral mass density, and electron density shows a very good agreement. The model reproduces the meso-scale structures of the upper atmosphere that are seen in the satellite data.

In this chapter, I represented only a few examples, but I performed a detailed analysis for 330 CHAMP flights over the polar regions during the 11 time intervals (see Table 3.1). A statistical comparison with other variants of the UAM model as well as with the global empirical models such as the thermospheric wind model (HWM07) and the atmosphere density model (NRLMSISE00) is also performed in Chapter 5.

The method presented in this chapter (see Section 3.4) allows the adaptation and the use of any physically reasonable FAC distribution as input parameter of the UAM model.

4. Using the MFACE field-aligned current model

4.1. Introduction

The materials of this chapter are partially published by *Prokhorov et al., 2014*. Some figures are directly taken from this paper.

The main idea of this chapter is the investigation of the MIT coupling at the high-latitude regions for various solar and geomagnetic activities, seasons and IMF strengths and orientations. For this purpose, I perform simulations of the upper atmosphere using the combination of the theoretical UAM and the high-resolution empirical MFACE models *[He et al. 2012]*. The MFACE model is used as input parameter to define the highly variable magnetospheric sources (system of FACs).

In this chapter, I present the high-resolution empirical MFACE model and a detailed description of the method to adapt the MFACE model for the UAM model. The new modification of the UAM model is compared with the satellite observations and empirical models. I perform a comparison of the thermospheric neutral wind calculated by the new modification of the UAM model with the CHAMP cross-track wind measurements and the global thermospheric wind model (HWM07) *[Drob et al. 2008]*. In addition, I compare the neutral mass density results with the corresponding CHAMP accelerometer data and the global empirical atmosphere density model (NRLMSISE00) *[Picone et al., 2002]*.

This is the first time I used a two dimensional high-resolution distribution of the FAC as input parameter for the UAM model. In the past, the system of the FAC in the UAM model was defined only along two lines *[Iijima et al. 1976, Papitashvili et al. 2002]*, which represent Region 1 and Region 2 currents. In this study, I use empirical models as additional references for the data comparison.

For this study, I analyzed 11 intervals (see Table 3.1) and performed comparisons (models/satellite) for 330 CHAMP flights over the polar regions. Unfortunately, it is impossible to present all of them. In this chapter I, therefore, show only a few examples, but performed a detailed analysis of the whole set.

The study focuses on the high-latitude regions of the upper atmosphere. All figures are shown in geomagnetic coordinates.

4.2. The high-resolution Model of Field-Aligned Currents through Empirical Orthogonal Functions Analysis (MFACE)

The MFACE model is a high resolution empirical model of field-aligned currents. Empirical Orthogonal Functions (EOF) of 12th order are used to construct the model. The observational basis of the model is the ten years interval (2000 – 2010) of magnetic field measurements obtained by the CHAMP fluxgate magnetometer.

The input parameters of the model are the magnitude and orientation of the IMF in GSM coordinates (B_Y and B_Z components), solar wind velocity (V_{SW}), day of year (seasonal dependence), and magnetic activity (AE index).

The MFACE model has the following spatial resolution. The latitudinal resolution is defined by a Butterworth low-path filter. It reduces small-scale fluctuations. The filtered cutoff the frequency is equivalent to a wavelength of 220 km; all longer wavelengths are suppressed. The actual latitude resolution is 55 km (about 0.5 deg). The longitude resolution is defined by the spherical harmonics of 4th order. The actual longitude resolution is 22.5 deg (1.5 hours).

The model provides the static two dimensional distribution of the FAC for the Northern and Southern polar regions. The MFACE model outlines the current profile and position of the Auroral Current Center (ACC) along each meridian. The model defines the FAC in latitude fixed to a 10 deg range equatorward and a 5 deg range poleward of the ACC position. Outside this area the FACs are zero. The positions of the ACCs constitute a closed oval around the polar cap region as shown in Figures 4.1 and 4.2 by the red dotted line. The ACC usually divides the FAC of Region 1 and Region 2.

The ACC can be used to define the shape and position of the auroral areas for the Northern and Southern polar regions. The auroral regions are significantly different for the Southern and Northern Hemispheres and depend on the IMF orientation. This is clearly seen in Figures 4.1 and 4.2 below:
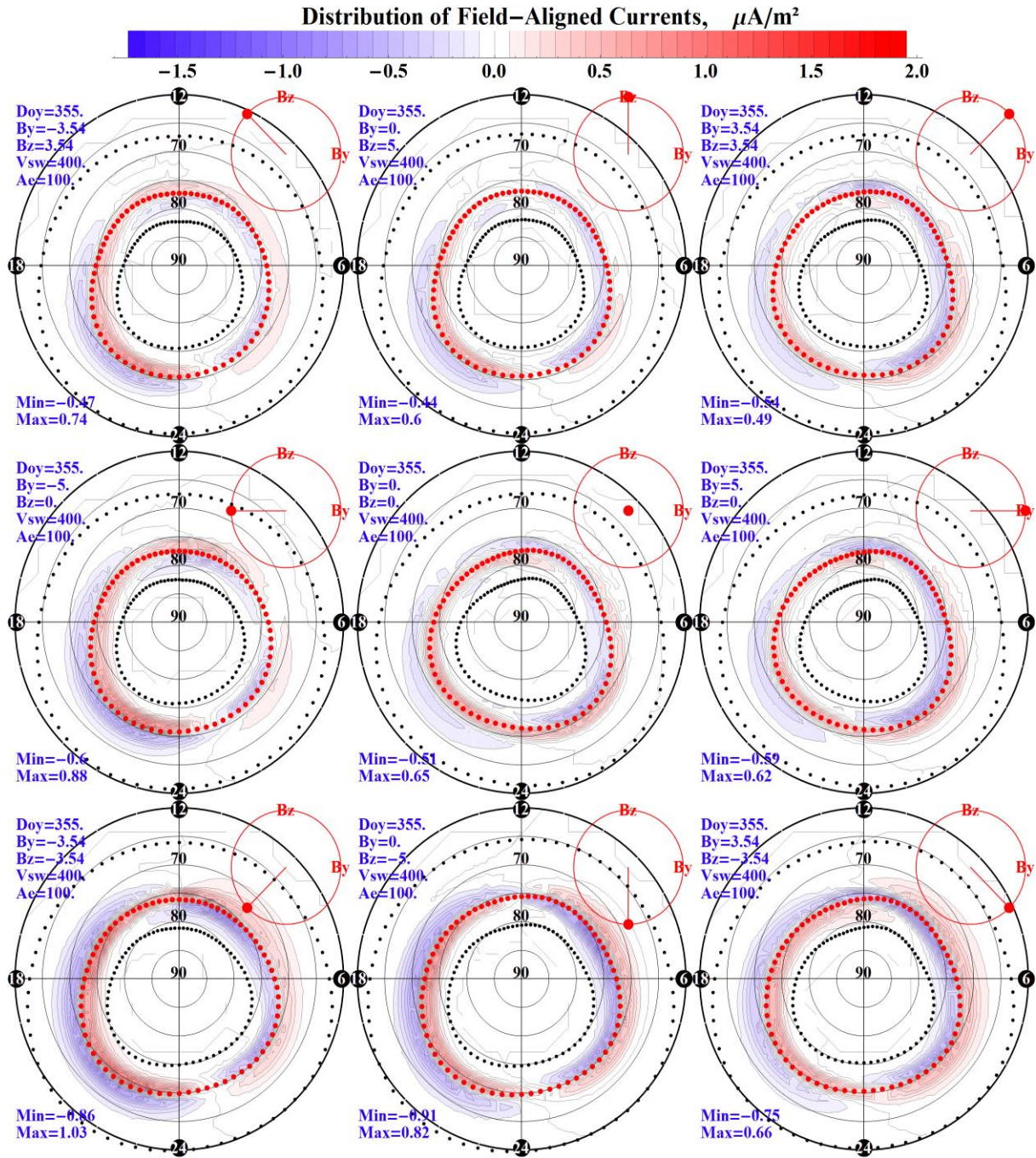
Figure 4.1. *An example of the FAC distributions for the Northern polar region. The distributions are obtained with the MFACE model. The patterns are shown for the same 8 clock-angle orientations of the IMF as in Figures 2.1 and 2.2. The central pattern shows the FAC distribution for $B_Y=0$ and $B_Z=0$, the so-called zero-state of the magnetosphere, supposedly with vanishing reconnection processes on the front side magnetosphere. Upward currents are indicated in red color, downward are indicated in blue color.*
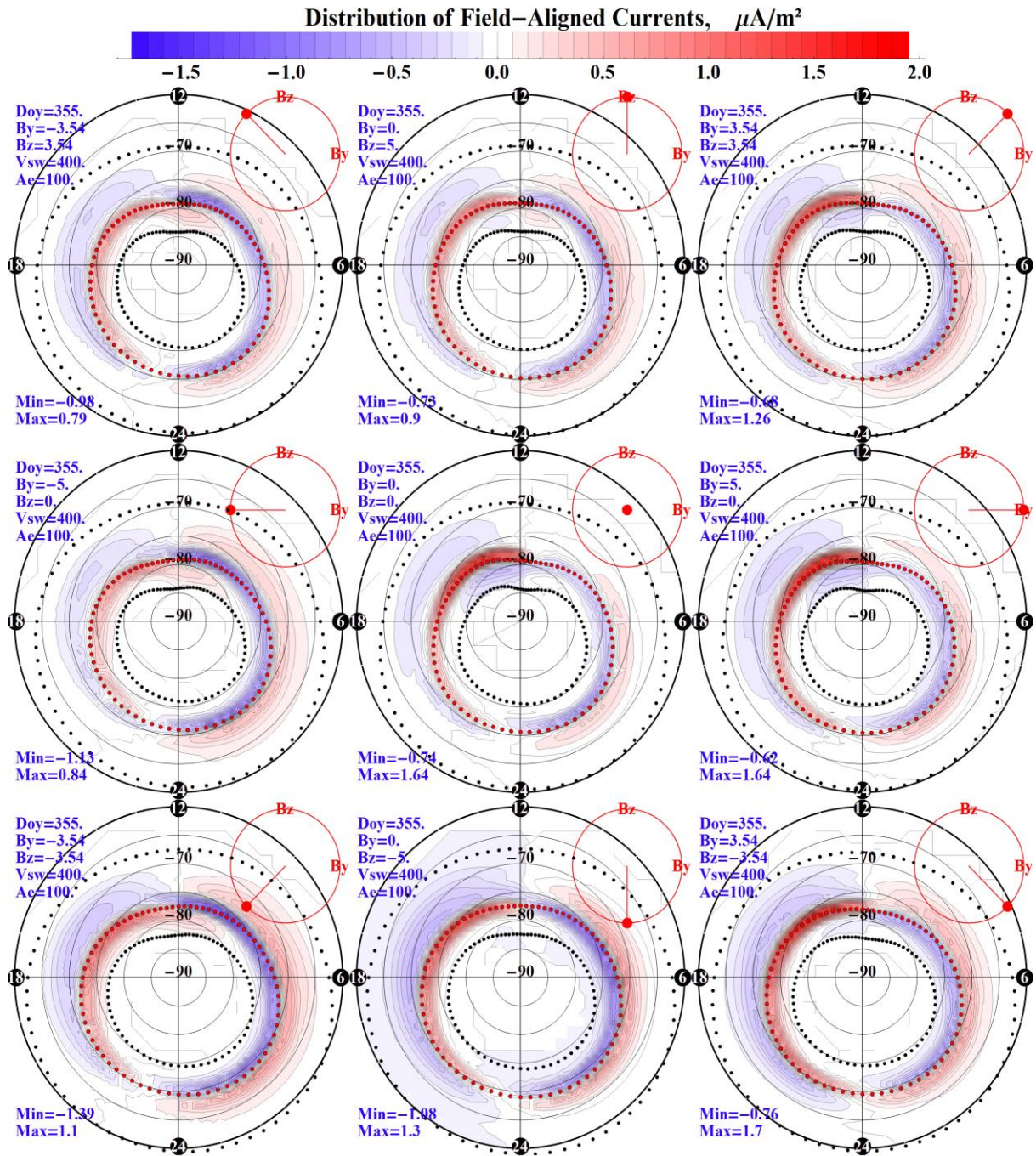
Figure 4.2. *An example of the FAC distributions for the Southern polar region. The figure is presented in the same style as seen in Figure 4.1 [**Prokhorov et al. 2014**].*

Figures 4.1 and 4.2 show patterns of the FAC distribution for different IMF orientations for the Northern and Southern Hemispheres. The distributions are obtained with the empirical MFACE model for low geomagnetic activity (AE index is 100 nT); the solar wind velocity is equal to 400 km/s and the magnitude $(B_Y{}^2 + B_Z{}^2)^{1/2}$ is 5 nT.

The whole system of the FACs is shifted by a few degrees to the night side. The Region 1 currents comprise the ring structure with upward currents (from the ionosphere) on the evening side and downward currents (into the ionosphere) on the morning side. The Region 2

currents are located equatorward of the Region 1 currents and form the outer ring of the FAC system. The Region 2 currents have the opposite orientation in comparison with Region 1 currents. The Region 0 currents are located in the cusp area located inside the polar cap region, poleward of the Region 1 currents. The Region 0 currents are visible in the middle upper panel for the Southern Hemisphere (for B_Y=0 nT & B_Z=5 nT); at all other panels the Region 0 currents are not so well pronounced o rare even absent.

The system of the FAC has an asymmetry in the distribution with respect to the IMF B_Y. This asymmetry is clearly seen between patterns with positive and negative B_Y. For the Southern Hemisphere the evening part of the Region 1 currents dominates for negative B_Y, while the morning part of Region 1 dominates for positive B_Y. The opposite is valid for the Northern Hemisphere.

Furthermore, a seasonal difference between the hemispheres is visible in Figures 4.1 and 4.2. The magnitudes of FACs for the Northern winter Hemisphere are significantly weaker than these for the Southern summer Hemisphere and vice versa for the Northern summer Hemisphere and Southern winter Hemisphere.

4.3 Using the MFACE model as input parameter for the UAM model (adaptations & assumptions)

4.3.1. The space grid

An irregular space grid has been selected with variable latitudinal, but equivalent longitudinal steps (10 deg). The step length is reduced to 0.5 deg in the auroral region so that all latitudinal features of the MFACE model are kept. The grid steps outside the polar region increases up to 2 deg (poleward) and up to 5 deg equatorward. Such geometry of the space grid fits well with the spatial resolution and keeps all features of the MFACE model.
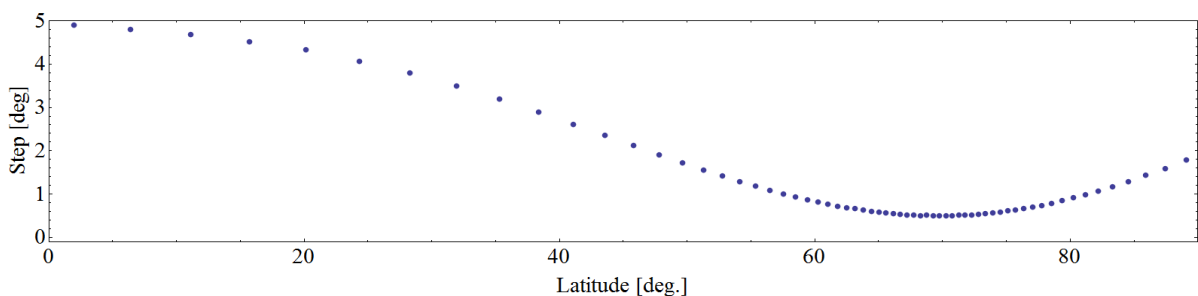
Figure 4.3. *The latitudinal profile of the space grid used in the UAM model.*

Figure 4.3 shows the variable step lengths in dependence of latitude for the Northern Hemisphere. A mirror profile of the space grid is valid for the Southern Hemisphere. This space grid describes well the auroral region in the latitude range from 60 (-60) deg to 80(-80) deg, which is the area of FACs and auroral precipitations.

4.3.2. The electric potential distribution
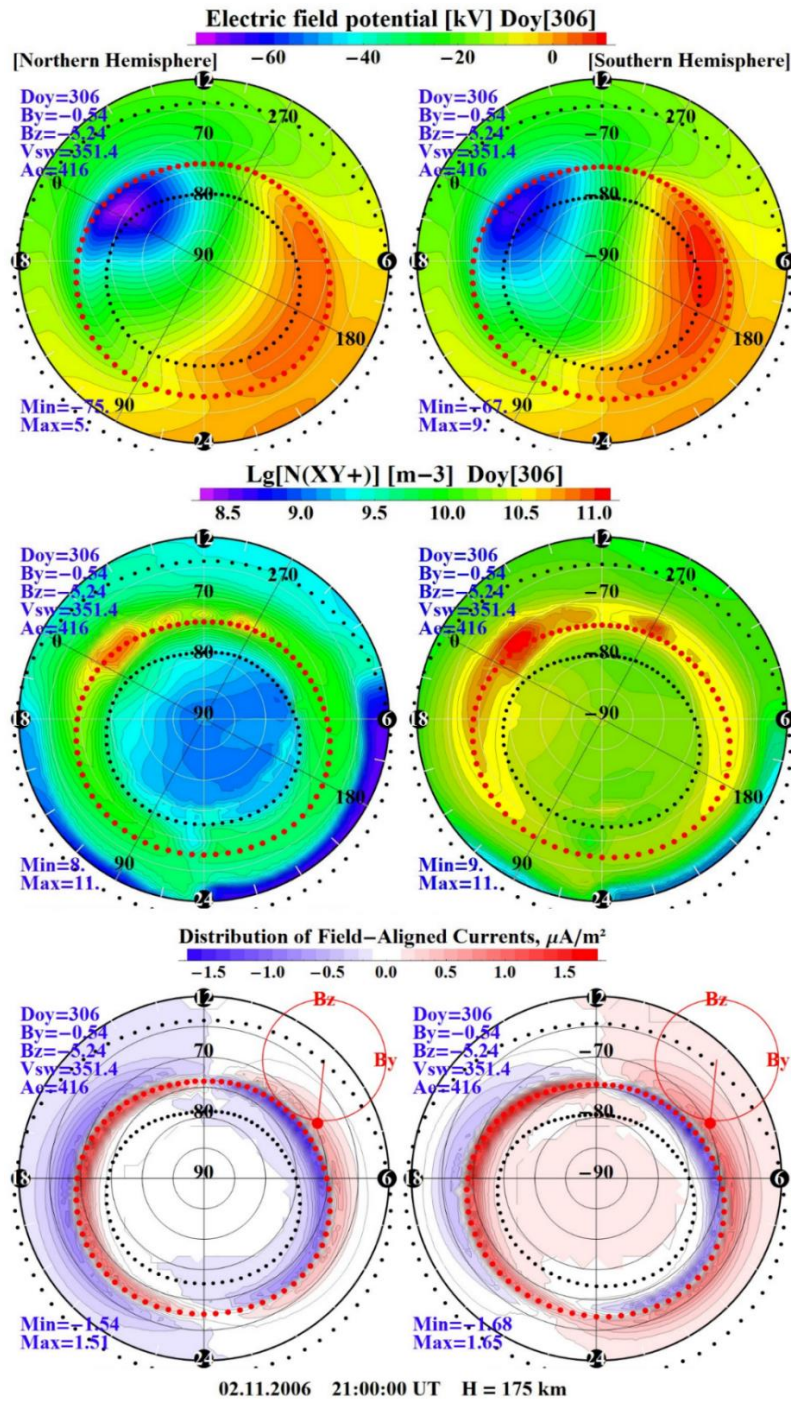
Figure 4.4. *An example of electric potential distribution obtained using the UAM model is shown in the upper panel. The logarithm of molecular ion distribution at 175 km altitude is presented in the middle panel. The distribution of the FACs calculated with the MFACE model is displayed in the bottom panel. The red dotted lines show the position of the ACC. The boundaries of the FACs are presented by black dotted lines. The input parameters for the MFACE model are: IMF B_Y = -0.54 nT; IMF B_Z = -5.24 nT; Solar wind velocity = 351.4 km/s; AE index = 416 nT.*

The upper panel of Figure 4.4 shows the distribution of the electric potential obtained by the UAM model with FACs calculated with the MFACE model. The distribution is calculated for a particular case with southward IMF (B_Z is -5.24 nT) and moderate magnetic activity (AE index is 416 nT). This case is part of the 11th time interval presented in Table 3.1.

The maxima and minima of the electric potential are clearly emphasized in both hemispheres and are located on the morning and evening sides, respectively. The evening cell is "round-shaped" and the morning cell is "crescent-shaped" in the Southern polar region. The situation is opposite in the Northern polar region (*cf. eg.,* ***Ruohoniemi et al. 2005***). The difference in the orientations of the electric field inside the polar cap is visible between the Southern and Northern Hemispheres (see Figure 4.4 upper panel). The electric field is perpendicular to the isolines of the electric potential. The asymmetry in the positions of the minimums and maximums between the hemispheres is also distinctive. Similar features of the electric potential variations are shown in ***Förster et al. 2009*** for negative B_Z and negative B_Y components.

4.3.3. The adaptations of the auroral precipitations

The energies of the precipitation fluxes as well as their local time distribution are defined by the empirical model of ***Hardy et al. [1985]***. The precipitation area is a region of higher conductivity and should be consistent with the distribution of FACs. The latitude distribution of the precipitations is adapted to the MFACE model. To achieve this, the position of the flux precipitation maximum along each meridian is fixed to the boundary between the FAC Regions 1 and 2 at the border between open and closed field lines. This boundary is located in the vicinity of the ACC. The precipitation area is restricted by the same boundaries as the FAC distribution. Such location of the precipitation provides a good agreement between the high conductivity areas and the distribution of the FAC.

The molecular ion's distribution is the direct result of the ionization due to the high-energy particle precipitation. The logarithm of the molecular ion density is shown in the middle panels of Figure 4.4. The precipitation area constitute the auroral oval, which is clearly seen in the figure. The concentration of ionized particles is different at both hemispheres. This effect takes place because of the seasonal difference. In other words, in the Southern Hemisphere is summer (polar day) and this implicates a significant additional ionization by the solar EUV. The opposite situation occurs in the Northern polar region (winter − polar night) where the auroral precipitations constitute the exclusive ionization source.

The empirical model of **Hardy et al. [1985]** does not contain any dependence on the IMF. The flux precipitation distributions used for the simulation runs are the same as these for the Southern and Northern polar regions. This is clearly seen in the figures. The position of the maximums are the same in both hemispheres. As a result, the effect of the FAC's asymmetry between the hemispheres becomes smaller. In the future, I plan to find or create a precipitation model with IMF dependence. Unfortunately, I do not have such a model now.

The bottom panel shows the distribution of the FAC calculated with the MFACE model. The ring structures of the Region 1 and 2 currents are clearly visible. The Region 0 currents are not pronounced. The seasonal difference in the FAC magnitudes can be distinguished between the Northern (winter) and Southern (summer) Hemispheres. This difference is approximatly 10%. In the winter hemisphere the current's magnitude is lower. At the first sight, the FAC distribution is ready to be used as input parameter for the UAM model. Closer considerations of the actual field line geometry leads to the conclusion that some further, smaller adaptations are required. This will be shown in the next subsection.

4.3.4. The boundary between open and closed field lines

The FAC patterns obtained from the MFACE have different spatial distributions for the Southern and Northern Polar Regions. The most significant problem involves how to distinguish the boundary between open and closed magnetic field lines. In this model realization, I consider the boundary between the Region 1 and Region 2 currents with zero current values as the position of the boundary between open and closed field lines (see Figures 4.1 and 4.2).
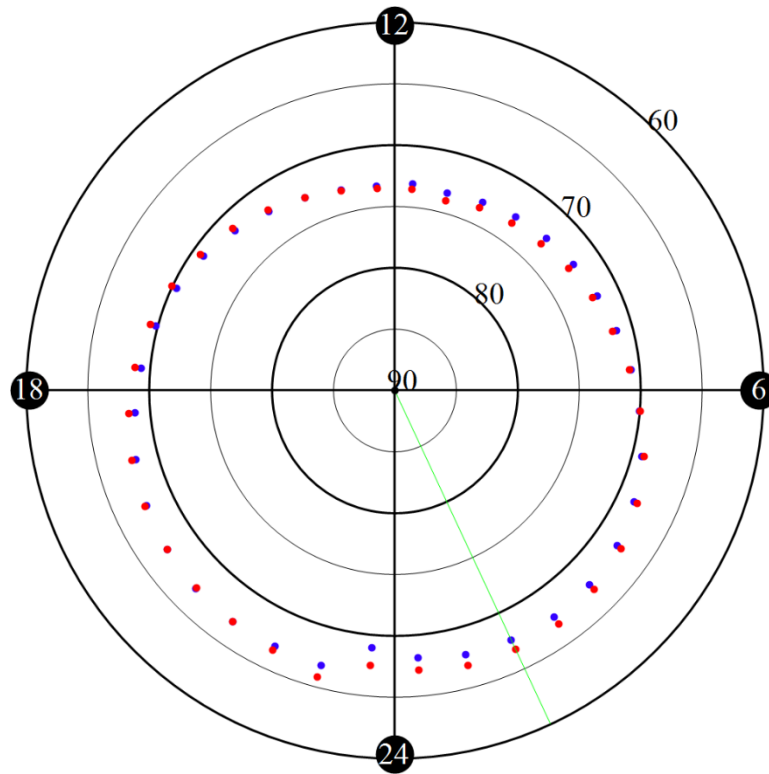
Figure 4.5. *The boundaries between the Region 1 and 2 currents for the Northern (blue) and Southern (red) Hemispheres. The green line shows 01:40:00 LT. The input parameters for the MFACE model are: B_Y = -0.54 nT; B_Z = -5.24 nT; Solar wind velocity = 351.4 km/s; AE index = 416 nT.*

In Figure 4.5, slightly different boundaries are found between the Northern and Southern Hemispheres. The equipotentiallity condition for the electric field modeling required that the boundary coincide for both hemispheres, i.e. they are the same geomagnetic field lines or are at the magnetically conjugated footpoints of the same field lines. For this purpose I needed to modify the distribution of the FAC. For each longitude, I estimated the latitude position of those boundary points for both hemispheres *(lat$_N$; lat$_S$)*. The mean latitude value *(lat$_N$+lat$_S$)/2* was then used as the common boundary latitude for the Southern and Northern Polar Regions. I shifted the profiles for each meridian by a value equal to: *lat$_N$ - (lat$_N$+lat$_S$)/2 {lat$_S$ - (lat$_N$+lat$_S$)/2}* for the Northern {Southern} Hemisphere. As a result, I obtained the FAC distribution with the same boundaries for both polar regions. The correction shifts of the current profiles along latitude are not significant; they are about ~1 deg or less.
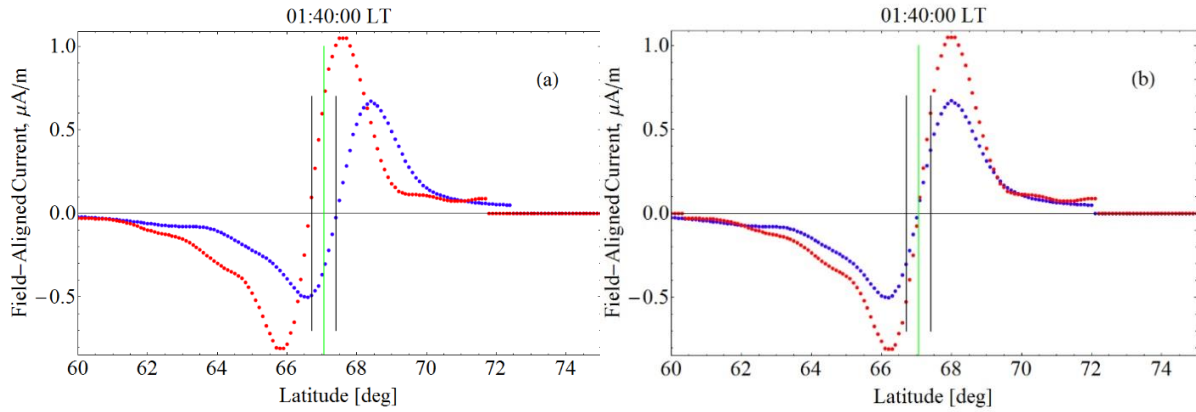
Figure 4.6. *An example of the longitudinal FAC profiles (01:40:00 LT) for the Northern (blue) and Southern (red) Hemispheres before (a) and after (b) correction. The input parameters for the MFACE model are: B_Y = -0.54 nT; B_Z = -5.24 nT; Solar wind velocity = 351.4 km/s; AE index = 416 nT.*

In Figure 4.6 (a) the distance between the black vertical lines illustrates the offset between the hemispheres (about ~ 0.7 deg). The modification result is presented in panel (b). The green vertical line shows the boundary between the Region 1 and 2 currents for the Northern and Southern polar regions after the correction. The field lines equatorward of this boundary are equipotential (closed) between the Northern and Southern Hemispheres. The field lines located poleward are not equipotential (the modeling Equation 1.26 is solving independently for the hemispheres).

Similar corrections are automatically performed for all other longitudes. Such correction helps to separate the Region 1 and 2 currents and keep the shape of the FAC profile.

4.3.5. The UT variations

In the present study I suppose that the magnetospheric generator is a voltage generator. The FAC system is assumed to generate the same cross polar potential for the Southern and Northern Hemispheres. The Earth rotation axis has a significant offset with the geomagnetic axis. As a result, the ionization of the polar region due to the solar EUV varies. This provides a variation in the conductivity of the high-latitudinal upper atmosphere. To fit the idea of the voltage generator, the system of the FAC should have some magnitude variation or the so called UT variation.

The seasonal dependence is included into the empirical MFACE, while the UT variation is not. I included the UT variations of the FAC in the similar way as it is described in Section 2.3.4 but with one modification, as represented in Section 3.5. The amplification coefficients are independent for the Northern and Southern polar regions. I used this assumption because

the FAC distributions are different for the hemispheres. An example of this adaptation is presented in Figure 4.7:
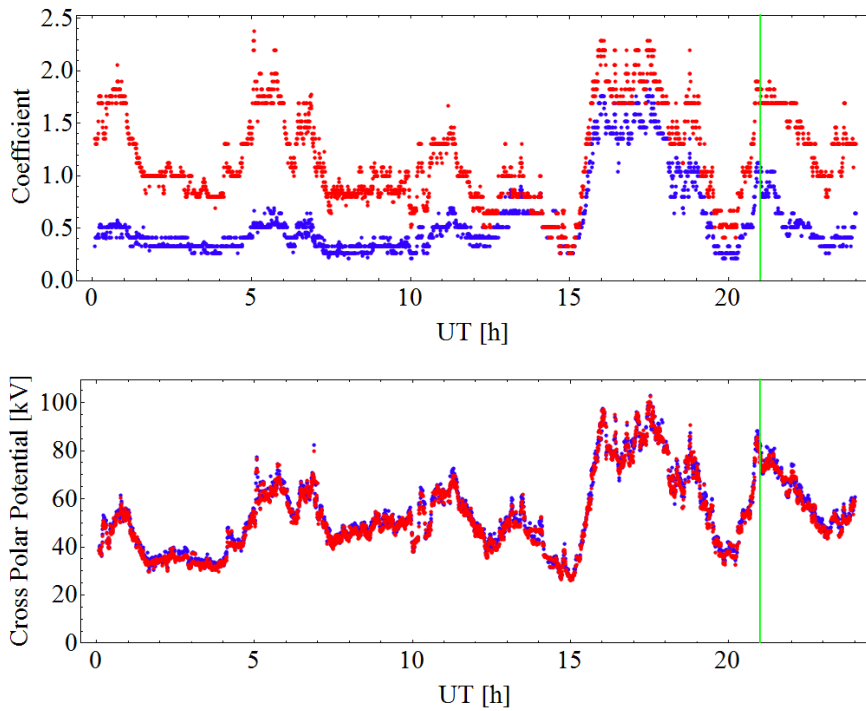
Figure 4.7. *An example of the UT variations of the coefficients (upper panel) and cross polar potential (bottom panel) for the 02.11.2006 (11th interval). Values related to the Northern and Southern polar regions are indicated by the blue color and the red color, respectively. The green vertical line represents the time moment 21:00:00 UT.*

The UT variation of the FAC amplifying factor for both hemispheres is shown in the upper panel of Figure 4.7. The difference in the magnitudes of FAC between the two hemispheres is significant (up to ~ factor 4) and clearly visible in the figure. The time-dependent coefficients for the example presented above, e.g. for one specific time moment 21:00:00 UT, are 1,04 and 1,69 for the Northern and Southern polar regions, respectively.

As a result, the UT variation is more significant than the seasonal variation. That is seen in Figures 4.4 (the FAC distribution with seasonal variation) and 4.8 (the FAC distribution with seasonal variation and UT variation). The example shows that the coefficient magnitudes have a strong relation to the variation of the cross polar cap potential. This calibration algorithm adapts the MFACE model for the UT variations as well as for the actual geomagnetic situation.

4.3.6. The FAC patterns after calibration
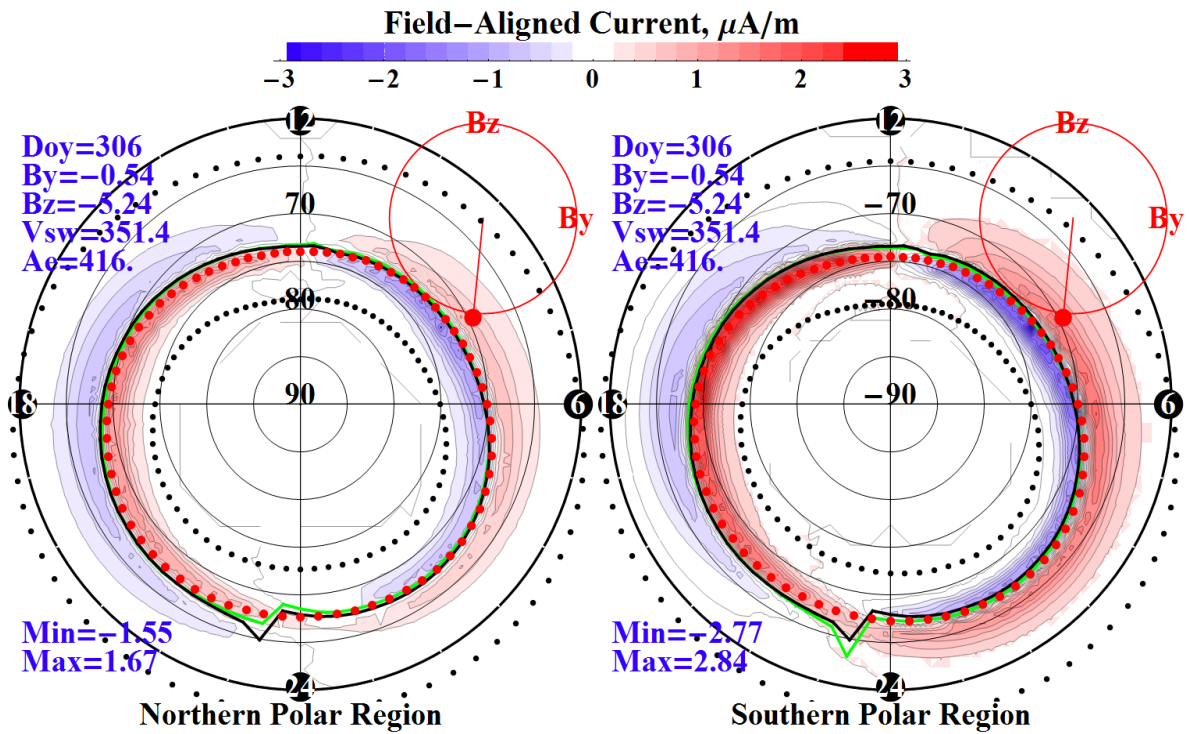
Figure 4.8. *The distribution of the FACs calculated with the MFACE model and adapted to the UAM model. The red dotted lines show the position of the ACC. Black dotted lines present the equatorward and poleward boundaries of the FACs. The time moment is 21:00:00 UT. The correction coefficients are 1,04 and 1,69 for the Northern and Southern polar regions respectively. The input parameters for the MFACE model are: B_Y = -0.54 nT; B_Z = -5.24 nT; Solar wind velocity = 351.4 km/s; AE index = 416 nT.*

The distribution of the FACs for the Northern and Southern polar regions after the adaptation procedure is drawn in Figure 4.8. The black line shows the boundary between the Region 1 and Region 2 currents. The green line presents the boundary before correction.

The latitudinal correction does not significantly change the shape of the FAC distribution. Usually, the shift of the current profile along a meridian is less than the latitudinal step of the space grid (0.5 deg.). The Region 1 and Region 2 currents constitute a continuous ring structure at those sectors. The most significant modification usually takes place at the noon and midnight sectors. Such a feature is clearly seen near the midnight at ~23 MLT (Harang discontinuity) in Figure 4.8. The maximal difference is about 0.7 deg. at that sector.

The correction due to the UT variation modifies (sometimes significantly) the magnitude of the FAC distribution but does not change the geometry. As seen in Figure 4.8, the magnitude for the Southern Hemisphere is significantly amplified (amplification coefficient is 1.69).

4.4. Modeling results

4.4.1. Thermospheric neutral wind

The system of the magnetospheric FAC and ionospheric neutral wind dynamo currents together with the tensor of the conductivity define the Earth electric field. This generator drives also the ion drift which transfers the energy to the neutral particles via collisions. The thermospheric neutral wind is the result of this MIT interaction. On the other hand, the thermospheric neutral wind is the origin of the system of the dynamo currents. The quality of the neutral wind distribution explicitly shows that the model, the UAM with MFACE, reproduces the MIT coupling system.

The UAM model provides a global thermospheric neutral wind distribution. To quantify the modeling results, I performed a comparison of the thermospheric neutral wind with an empirical model and the CHAMP satellite data.

4.4.1.1. Horizontal wind model 2007 (HWM07)

The HWM07 is a global empirical model of the horizontal thermospheric neutral wind fields. This model represents an improvement of the previous versions of the model (HWM87, HWM90 and HWM93) *[Hedin et al., 1988, 1991, 1996]*. The HWM07 model is constructed using the satellite, rocket and ground-based observations of the thermospheric neutral wind. The model provides the global horizontal thermospheric neutral wind distribution with dependence on the geomagnetic activity at the altitude range of 0-500 km *[Drob et al. 2008]*.

The thermospheric neutral wind obtained with the HWM07 model is used as reference data for this study. Below, I provide a comparison of the neutral wind calculated using the UAM and HWM07 models with the CHAMP satellite accelerometer measurements.

4.4.1.2. Thermospheric neutral wind data comparison

The accelerometer on board of the CHAMP satellite provides only the horizontal cross track component of the neutral wind (the vector projection on the perpendicular horizontal direction in the CHAMP satellite coordinate system). In addition, the satellite provides data only for one particular point in space for each time moment. Nevertheless, even such small information is sufficient to constrain the global distribution of the thermospheric winds and perform a comparison with the UAM model results.

The most interesting overflights for the neutral wind data comparison are the paths when the CHAMP satellite crosses the vortices areas (i.e. overflights in the dawn-dusk direction). Those overflights help us to understand accuracy of the UAM model when reproducing the

position of the convection cells as well as the magnitudes of the thermospheric neutral wind. An example of such polar overflights is presented in Figure 4.9:
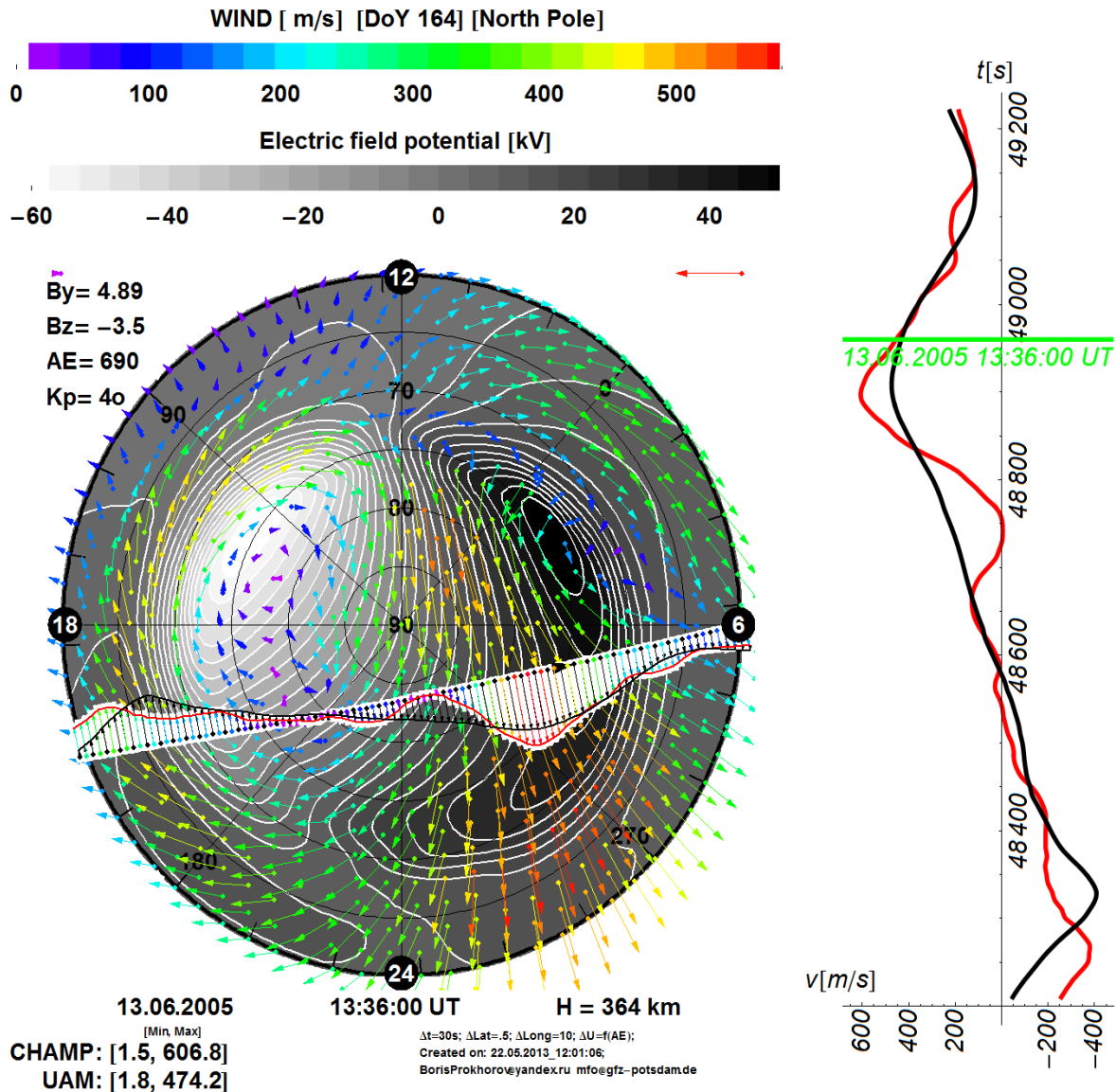
Figure 4.9. *An example of the comparison of the UAM model results with the CHAMP satellite accelerometer measurements for one flight over the Northern Hemisphere on 13th of June 2005. The graphic on the right shows the comparison of the cross-track neutral wind component measured by the CHAMP in the S/C coordinates (red line) with the corresponding model result (black line). The current position of the CHAMP satellite at the time moment (13:36:00 UT) is shown by the green line on the right graphic [**Prokhorov et al. 2014**].*

In Figure 4.9, the electric potential distribution is shown through the scale in the black & white background. The two vortices are clearly seen in the evening and morning sides. The vortex locations have a strong correlation with the positions of the electric potential minimum (dusk side) and maximum (dawn side). The strong noon – midnight stream is also clearly visible.

The CHAMP satellite overflight is indicated in Figure 4.9 by a straight dotted line across the polar region. The colored arrows represent the CHAMP cross track neural wind measurements. The black arrows show the corresponding neutral wind vector projections (Y-component in the satellite coordinate system) of the UAM model. The red and black lines bound the satellite observations and modelling data, respectively. The black arrow at the dotted line shows the flight direction and the satellite position at the current time moment (13:36:00 UT). The green line presents the actual CHAMP position on the additional graphic located on the right side.

The UAM model provides realistic distributions of the thermospheric wind data, as exemplified in Figure 4.9. The general meso-scale structures such as the position and size of the vortex areas coincide well with the CHAMP satellite observations. The neutral wind magnitudes also have good agreement with the satellite measurements.

The example shown above demonstrates the methodology of the data comparison which is suitable for detailed studies of any particular event. In the following figure, an alternative way of data presentation is introduced for the model data comparisons. A few examples will illustrate this by means of the UAM and HWM07 models in comparison with the CHAMP accelerometer measurements.
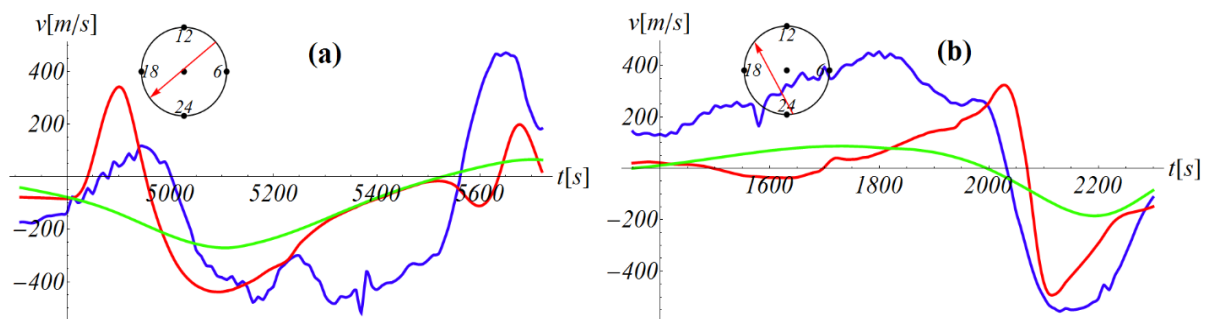
Figure 4.10. *Examples of two CHAMP paths over the polar regions. The left and right panels present the flight (a) over the Northern Hemisphere for 18 November 2002 and (b) Southern Hemisphere 14 April 2001, respectively. The cross track wind speed is shown for the UAM simulation (red), HWM07 (green), and CHAMP measurements (blue). The CHAMP path over the polar region is shown by the red arrow within the dial in the upper left side of each panel* [***Prokhorov et al. 2014***]*.*

The CHAMP satellite measurements show some smaller-scale fluctuations despite a regular meso-scale variation. Those fluctuations have a magnitude of about 50 m/s and are clearly visible in Figure 4.10. The vortices areas are well pronounced in the satellite observations and can be distinguished on the dawn and dusk sides (near 4950 s and 5650 s UT,

respectively) in the left panel. In the right panel the evening circulation cell is clearly seen in the satellite observation data near 2200 s UT.

The theoretical UAM model shows a good agreement with the CHAMP satellite accelerometer measurements. The UAM model presents a similar meso-scale structure of the thermospheric wind data as the CHAMP data. The amplitude value range and the vortices' positions agree well with the satellite data. Compared with the CHAMP data, the UAM model results do not have small-scale fluctuations.

The empirical HWM07 model wind component (green lines) reveals a very smooth variation of the thermospheric neutral wind data across the polar region. The variation range of the empirical model is significantly smaller than the variation of the satellite data (approximately two times smaller). The vortices areas are not distinguishable.

The thermospheric neutral wind distribution obtained with the new version of the theoretical UAM model reveals a realistic structure, which is presented in Figure 4.9. The meso-scale structure of the neutral wind calculated with the UAM model coincides well with the CHAMP accelerometer measurements. The theoretical model reproduces the vortices' areas better than the empirical HWM07 model. At the same time, the UAM model provides a more realistic variation range of the thermospheric wind data, which is clearly seen in Figure 4.10.

4.4.2. Neutral mass density

The neutral mass density plays also a significant role in the MIT dynamic coupling system. This parameter has strong relations with the thermospheric neutral winds which are responsible for the plasma motion in the upper atmosphere. On the other hand, the neutral mass density constitutes the background for the braking of charged particles (ion drag) and corresponding ionization ratios. All these define the tensor of the ionospheric conductivity.

The UAM model provides a global distribution of the neutral mass density. To quantify the modeling results, I perform a comparison of the neutral mass density wind with the empirical model and satellite data in the same style as the comparison of the thermospheric neutral wind data.

4.4.2.1. Naval Research Laboratory Mass Spectrometer and Incoherent Scatter Extended 2000 (NRLMSISE-00)

The global empirical NRLMSISE-00 model supplies the distributions of the density and temperature for the basic components of the neutral atmosphere (He, O, N_2, O_2, Ar, H, and N) in the altitude range from the ground level up to the exobase. The model is based on the Mass

Spectrometer and Incoherent Scatter measurements. The previous versions of the NRLMSISE-00 model are the MSIS-86 *[Hedin, 1987]* and MSISE-90 *[Hedin, 1991]*. The model has the following input parameters: the solar radio flux ($F_{10.7}$), the daily A_p and the 3-hourly a_p geomagnetic indices. *[Picone et al., 2002]*.

The distribution of the neutral mass density obtained with the empirical NRLMSISE-00 model is used as the reference data in this study. The comparison of the neutral mass density results obtained by the theoretical UAM and empirical NRLMSISE-00 models with the CHAMP accelerometer measurements is presented below.

4.4.2.2. Neutral mass density data comparison

Like the thermospheric neutral wind, the CHAMP satellite offers neutral mass density measurements for each time moment at the spacecraft position. I performd a data comparison between the data obtained by the models and the CHAMP satellite accelerometer data for the polar overflights. The logic is the same as described in Section *4.4.1.2*. The satellite altitude varies along the orbit and is significantly different for different years. The altitude range is 357-467 km (for the events presented in my investigation). Such variation in range facilitates the examination of the behavior of the UAM model at different altitudes. The most interesting overflights are the satellite paths via the cusp region. These overflights help us to understand the accuracy of the UAM model when reproducing the position of the cusp region and the density profile in this highly variable area. A few examples are presented in Figures 4.11 and 4.12.
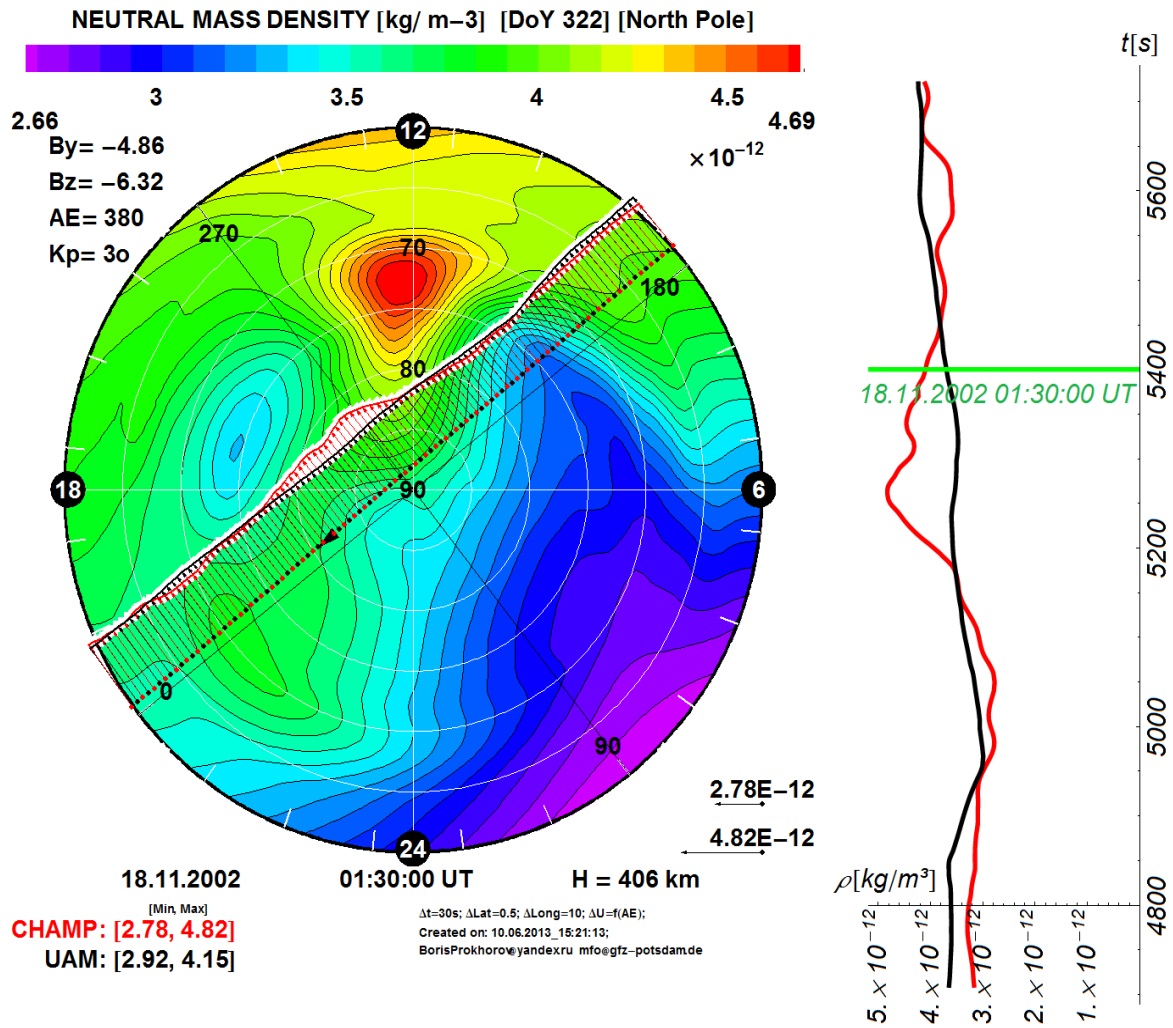
Figure 4.11. *Comparison of the UAM model result with the CHAMP satellite accelerometer measurements for one flight over the Northern Hemisphere for the 18th of November 2002. The graphic on the right shows the comparison of the neutral mass density measured by the CHAMP (red line) with the corresponding model result (black line). The current position of the CHAMP satellite at the time moment (01:30:00 UT as indicated by the arrow) is shown by the green line on the right graphic [**Prokhorov et al. 2014**].*

The comparison between the UAM model results and the CHAMP accelerometer measurements in Figure 4.11 is performed in the same style as shown for the thermospheric neutral wind data in Figure 4.9.

In Figure 4.11 it is clearly seen that the theoretical modeling results have a good agreement with the CHAMP satellite observations. The UAM model reproduces the neutral mass density values with nearly the same magnitudes as the CHAMP measurements along the whole polar overflight.

For the data comparison between the UAM and NRLMSISE-00 models, I used a simplified graphic style similar to that shown in Figure 4.10. A few examples are presented below:
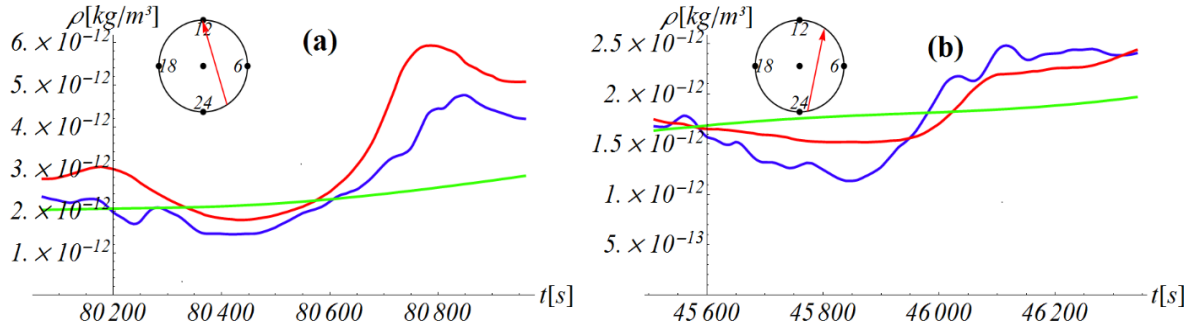
Figure 4.12. *Examples of two CHAMP paths over the polar regions. The left and right panels present the flight (a) over the Northern Hemisphere for 01 February 2003 and (b) Southern Hemisphere 10 December 2004, respectively. The neutral mass density is shown according to the UAM simulation (red), NRLMSISE-00 (green), and CHAMP measurements (blue). The CHAMP path over the polar region is shown by the red arrow within the dial in the upper left side of each panel [**Prokhorov et al. 2014**].*

The satellite accelerometer measurements of the neutral mass density has some small-scale fluctuations. These fluctuations are clearly visible in Figures 4.11 and 4.12. Together with small-scale fluctuations, the satellite data show some meso-scale structures, i.e. the sharp neutral mass density enhancements within the cusp region and broader depletion areas within the thermospheric neutral wind vortices.

The UAM model reproduces meso-scale structures similar to the CHAMP satellite observations as shown in Figure 4.12. The enhancement of the neutral mass density in the cusp region is well pronounced. The position and magnitudes of the density enhancement in the modeling results and CHAMP data has a good agreement as well as the whole neutral mass profiles.

The NRLMSISE-00 model provides in contrast to the satellite accelerometer measurements, a very smooth neutral mass density variation over the polar region. Meso-scale structures which are clearly seen in the satellite data are not visible. The empirical model reproduces only the approximate average values of the CHAMP profile.

The neutral mass density distribution calculated with the theoretical UAM model is realistic. One example is presented in Figure 4.11. The meso-scale structures of the neutral mass

densities obtained with the UAM model has good agreement with the CHAMP accelerometer observations. Together with it, the range of the UAM model density coincides with the satellite measurements. The empirical model provides very smooth data and does not reproduce the meso-scale structures.

4.5. Conclusion

The comparison of the neutral mass density and thermospheric wind calculated by the UAM model with the correspondent CHAMP accelerometer measurements shows a good agreement of the theoretical model with the satellite data. On the other hand, the comparison with the global empirical models such as the thermospheric wind model (HWM07) and the atmosphere density model (NRLMSISE00) shows that the UAM model reproduces the meso-scale structures of the upper atmosphere more realistically.

In this chapter I have described the method to adapt the MFACE model to the UAM model and I have shown some modeling results. At a further step, I am going to perform a statistical study which helps us to quantify the improvement of the modeling performance.

In the next chapter I will present such a statistical study - where the results of the UAM model with different FACs (MFACE, Papitashvily and Iijima-Potemra) are compared with the global empirical models (HWM07 and NRLMSISE-00) and the CHAMP accelerometer measurements in a statistical way. The satellite observations are used as reference data. I will carry out this statistical study using the classical statistical theory. I use mathematical expectation to define the offset between models and the standard deviation to quantify the variation range.

5. Statistical study

5.1. Introduction

This chapter summarizes the previous investigation results of the high-latitude Magnetosphere – Ionosphere – Thermosphere (MIT) dynamic system in ***Förster et al., 2011b, 2012; Namgaladze et al., 2013; Prokhorov et al., 2014.*** In there stadies, the researchers successfully improved the global, self-consistent, time-dependent Upper Atmosphere Model (UAM) [***Namgaladze et al., 1995, 1996b; Volkov et al., 1996; Hall et al., 1997***] by including the dependence on the Interplanetary Magnetic Field (IMF).

In this part of my thesis, I performed a statistical comparison of the UAM model with the different FAC distributions. The following FAC models were used as input parameter for the UAM model:

1. The empirical FAC model of ***Iijima and Potemra [1976]***. This classical model is based on the Triad satellite magnetometer data (see Chapter 2).

2. The empirical FAC model of ***Papitashvili et al. [2002]***. This IMF-dependent model is based on the magnetic field observations from the satellites Magsat and Ørsted (see Chapter 3).

3. The high resolution empirical FAC model of ***He et al. [2012]***. This model with the dependence on the IMF is based on fluxgate magnetometer measurements onboard the CHAMP satellite (see Chapter 4).

I modelled the MIT dynamic system for 11 different intervals (see Table 3.1) these represent various conditions with respect to seasons, solar wind velocity, geomagnetic activity and orientations of the IMF. The UAM model configurations with different FAC systems were run with the same initial conditions and on the same spatial grid. The simulation results obtained with the UAM model were compared with the global empirical models for the thermospheric wind (HWM07 ***[Drob et al. 2008])*** and neutral atmospheric density, temperature and composition (NRLMSISE00 ***[Picone et al., 2002])*** and the CHAMP satellite accelerometer measurements.

The comparison was performed in a statistical way for the thermospheric neutral wind and neutral mass density. For those parameters, I calculated and analyzed the standard deviation and mathematical expectation for the difference between the model results and the CHAMP satellite observation data. The mathematical expectation shows the offset between simulation results and measurements. The standard deviation provides the information about the variation range. The empirical models were used as etalons for the statistical comparison.

5.2. Method

The differences between the modelled data and the satellite measurements were used as basic parameter for the statistical analyses. In this study, I suppose that differences have a normal (Gaussian) distribution and the classical statistical theory therefore applies. The mathematical expectation and the standard deviation for differences were calculated to perform a statistic analysis of the agreement between the modeling and the CHAMP observation data. The first parameter Δ (mathematical expectation) represents the offset between the data sets – the systematical difference. The second parameter σ (standard deviation) shows the variation around the average value:

$$\Delta = \frac{1}{n} \sum_{i=1}^{n} \delta_i \, , \qquad\qquad (5.1)$$

$$\sigma = \sqrt{\frac{1}{n} \sum_{i=1}^{n} (\delta_i - \Delta)^2} \, , \qquad\qquad (5.2)$$

where Δ is the mathematical expectation; σ is the standard deviation; δ_i is the difference in the point "i"; and n is a number of points.

The magnitude of the wind velocity depends on the geomagnetic activity and has no strong dependence on altitude, at least in the CHAMP altitude range. The satellite accelerometer provided only the horizontal cross track wind speed component relative to the bulk flow with respect to the satellite. This value significantly depends on the angle between the satellite cross-track and wind bulk flow direction. This means that the measured wind speed V is a projection of the actual horizontal wind speed vector for each data point. It is a scalar value in the range $\pm|V|$. The angle is different in every point and because of it the cross-track wind measurements are more or less random values. I used the following formula to define the difference between the model thermospheric wind data and the observation values:

$$\delta_i = m_i - o_i \, , \qquad\qquad (5.3)$$

where δ_i - is the difference in the point and m_i and o_i are the modeling and the observation value of the cross-track wind component, respectively.

The neutral mass density depends significantly on the altitude due to the logarithmic scale of its height dependence. The CHAMP satellite altitude variation is about ±10 km during one orbit around the Earth. Such altitude variation corresponds approximately to a two time difference in the neutral density data (see Section 3.4.2.4).

In this investigation, I studied several events for different years and the satellite altitudes. The altitude range for all intervals in Table 3.1 is 357-467 km. This altitude variation corresponds to more than a 20 time difference in the neutral density data, therefore the absolute difference cannot be used in this statistical study.

I used the ratio between the difference of the modeling data and the observation values over the observation values to avoid this altitude dependence for the comparison:

$$
\delta_i = \left| \begin{array}{l} \dfrac{m_i}{o_i} - 1, \text{ for } m_i > o_i \\[2ex] 1 - \dfrac{o_i}{m_i}, \text{ for } m_i \leq o_i \end{array} \right. ,
\tag{5.4}
$$

where δ_i is the relative difference in the point and m_i and o_i are the modeling and observation value, respectively.

5.3. A statistical comparison for the thermospheric neutral wind data

The simulated thermospheric neutral wind and neutral mass density data were compared with the CHAMP satellite accelerometer measurements and the well known empirical models HWM07 (for the wind data) and NRLMSISE-00 (for the density data). Such comparison quantifies the modeling prediction. At the same time, the comparison with the satellite data helps us to determine how realistic the UAM modelt can reproduce the MIT dynamic system with the various FAC distributions. The distributions of the differences for the thermospheric neutral wind data are shown below.
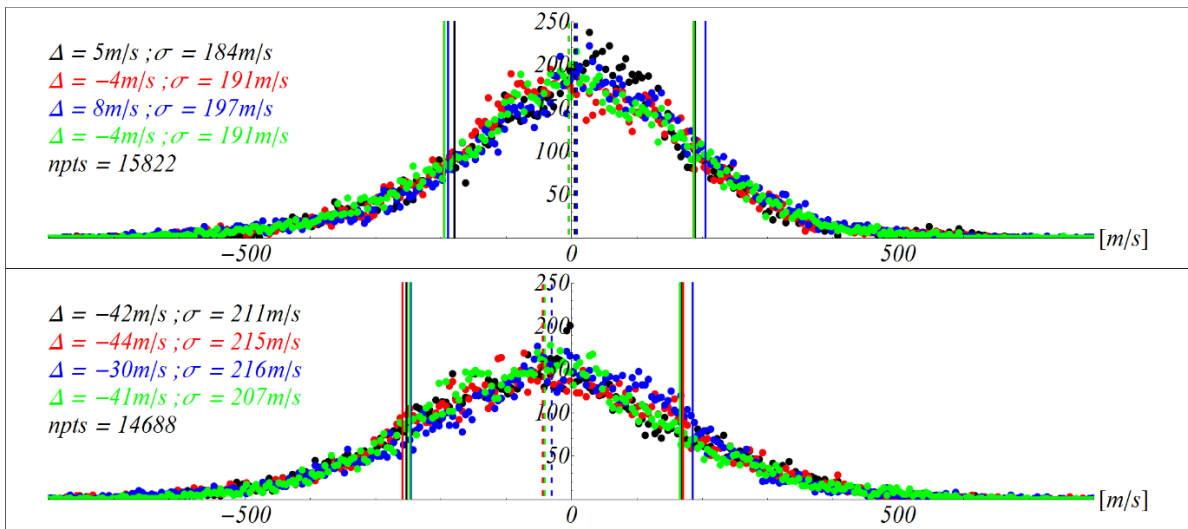
Figure 5.1. *The distributions of the differences between various models and the CHAMP measurements for the Northern (upper panel) and Southern (bottom panel) polar regions. The differences for the empirical HWM07 model (black), the UAM model using MFACE (red), the PM (blue), and the IPM (green). The difference data are divided into intervals and integrated. The interval size is 5 m/s.*

In Figure 5.1 the differences between the satellite accelerometer measurements and the modeling data fit to a normal (Gaussian) distribution. All models show similar statistical parameters for both polar regions. For the Northern polar region, the mathematical expectations and standard deviations are about 0 m/s and 190 m/s, respectively. The mathematical expectations and standard deviations for the Southern polar region are about - 40 m/s and 210 m/s, respectively. The difference between the hemispheres is clearly visible (the models have a better agreement with the CHAMP data in the Northern Hemisphere).

The data point amount (15822 and 14688 for the Northern and Southern polar regions, respectively) is large enough to perform a statistical study. The difference for the standard deviations between the hemispheres is about 10%. This was possibly due to the difference in

the offsets between the geomagnetic and geodetic coordinate systems for the Southern and Northern Hemispheres. The UAM model uses a dipole magnetic field. The (ideal) dipole coordinate system has by definition the same offset between the geomagnetic and geodetic poles for both polar regions. The real situation is slightly different. The offset between the geomagnetic and geodetic poles for the Southern Hemisphere is about two times larger than the offset for the Northern Hemisphere. This provides an additional variation (instability) of the driving forces (see *Förster et. al. 2008*).

The negative mathematical expectation for the Southern Hemisphere means, according to Formulas 5.1 and 5.3, that the models reproduce smaller neutral wind values than the CHAMP measurements. Such features could appear because the model does not so well reproduce the Southern polar region.
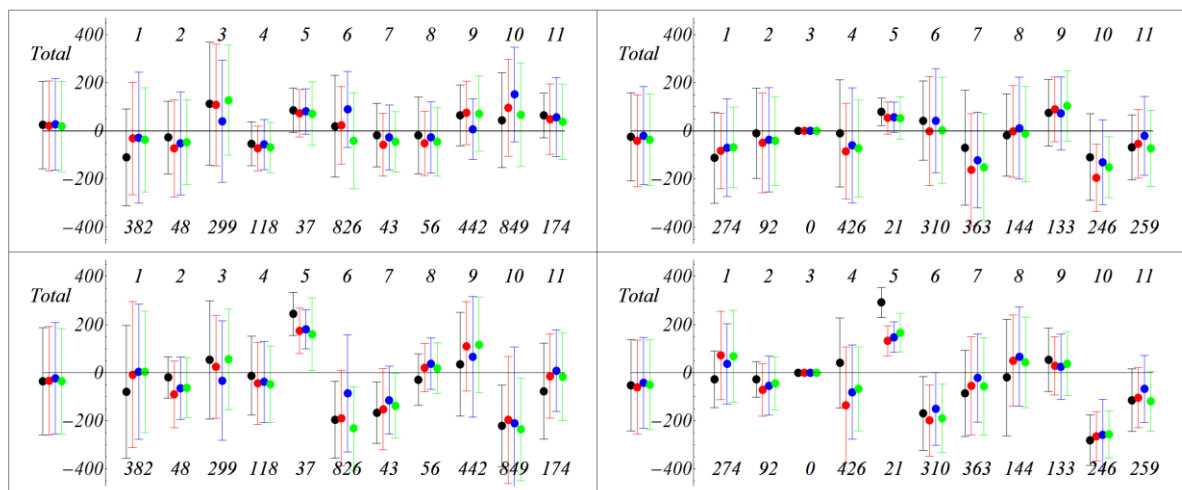
Figure 5.2. *The mathematical expectation (dots) ± standard deviation for all intervals of the Northern (upper panels) and Southern (bottom panels) polar regions and for both stable (left panels) and unstable (right panels) IMF conditions. The statistical parameters for the empirical HWM07 model (black), the UAM model using MFACE (red), the PM (blue), and the IPM (green). The average value of the AE index is mentioned at the bottom of each panel. Units are m/s.*

In Figure 5.2 the compilation of the results for each individual interval reveals that the values of the mathematical expectation and standard deviation can be significantly different for the different intervals. On the other hand, the various models applied show mostly very similar results for each individual interval. The mathematical expectations have similar values with the same sign. The magnitudes of the standard deviations have some correlation with geomagnetic activities (average value of the AE index). The range of variations is larger during geomagnetically disturbed time intervals. The detailed information is given in Table 5.1.
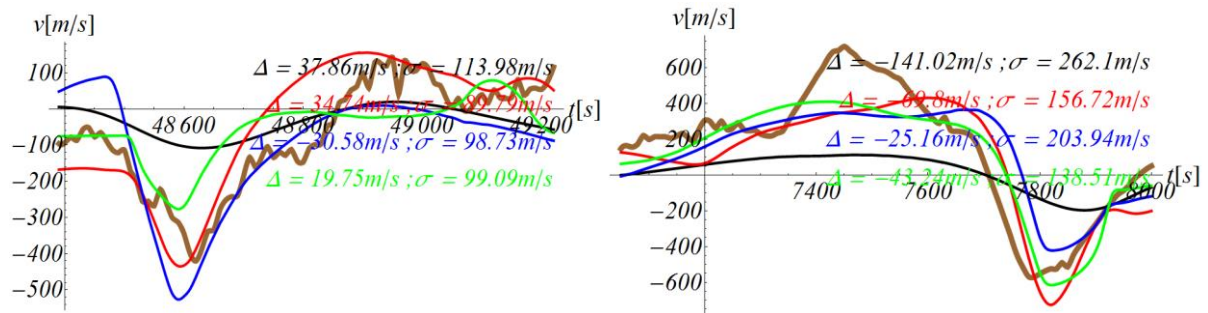
Date	Northern Hemisphere				Southern Hemisphere			
	Stable		Unstable		Stable		Unstable	
	Δ±σ, m/s	ntps	Δ±σ, m/s	ntps	Δ±σ, m/s	ntps	Δ±σ, m/s	ntps
14_ 04_ 2001	-110±201 -32±234 -29±272 -38±216	666	-112±189 -84±157 -70±203 -69±168	756	-80±276 -8±304 4±281 3±252	654	-27±118 72±184 36±167 68±191	732
25_ 05_ 2002	-28±150 -73±202 -52±214 -47±176	660	-10±188 -50±207 -37±217 -42±185	744	-19±86 -90±139 -65±130 -62±125	744	-28±74 -71±109 -54±122 -44±111	642
18_ 11_ 2002	112±256 107±253 40±254 128±228	1428	No Data	0	54±246 24±213 -33±248 56±209	840	No Data	0
01_ 02_ 2003	-54±92 -73±93 -57±104 -69±104	840	-11±223 -84±199 -61±239 -73±202	570	-12±164 -45±171 -38±168 -48±159	774	40±187 -135±242 -81±196 -67±175	642
23_ 10_ 2003	86±92 74±99 80±94 72±132	1296	79±57 54±67 57±63 53±88	186	244±90 174±94 180±81 160±152	1200	292±62 133±62 148±63 167±81	168
30_ 08_ 2004	20±211 23±161 89±158 -41±199	822	43±164 -1±226 42±216 2±221	660	-196±160 -188±198 -86±244 -231±173	822	-169±153 -199±148 -150±151 -189±142	558
13_ 09_ 2004	-18±132 -57±130 -27±135 -46±126	1314	-70±239 -162±234 -121±199 -151±223	186	-166±128 -152±168 -114±141 -137±134	1200	-86±179 -55±204 -22±183 -56±201	180
06_ 10_ 2004	-19±159 -52±134 -27±148 -46±142	426	-18±171 -2±191 12±212 -13±198	960	-28±107 21±100 38±107 19±105	534	-20±242 51±190 67±206 43±188	858
10_ 12_ 2004	64±127 75±132 7±126 72±157	642	75±139 90±135 72±152 103±146	756	36±215 110±186 66±251 116±198	732	54±132 28±121 25±136 38±133	642
13_ 06_ 2005	45±197 96±201 151±197 68±215	870	-109±180 -195±140 -130±176 -151±127	540	-221±169 -196±264 -210±317 -235±213	864	-280±105 -264±102 -258±147 -256±98	528
02_ 11_ 2006	64±93 48±146 57±164 37±157	492	-69±134 -53±143 -21±164 -73±159	1008	-76±200 -14±175 8±169 -16±183	480	-114±130 -104±124 -67±139 -119±124	894
Total	24±182 21±187 26±190 18±188	**9456**	-25±183 -41±191 -20±204 -36±190	**6366**	-36±223 -34±226 -23±232 -35±219	**8844**	-52±190 -60±195 -42±188 -50±186	**5844**

Table 5.1. *The mathematical expectations and standard deviations for the thermospheric neutral wind data. Statistical parameters of the empirical HWM07 model (black), the UAM model with the MFACE (red), the PM (blue) and the IPM (green).*

In Table 5.1 all models reproduce quite similar results. The total value of the mathematical expectation is negative and about - 25 m/s on average. This value is not so significant, especially if one takes into account the accuracy of the CHAMP satellite accelerometer measurements, which is about ± 50 m/s. The CHAMP accuracy has very complicated dependence on the satellite position and it can be more than 50 m/s. *[Doornbos et al., 2010]*

Statistically, the simulation results of the thermospheric neutral wind data obtained with the UAM model are very similar for all models. A few examples of the data comparison are

presented in Figure 5.3. Such direct comparisons help us to understand the quality of the simulation results.

Figure 5.3. Examples of two CHAMP paths over the Northern and Southern polar regions. The left and right panels present the flight over the Northern Hemisphere for 10 December 2004 and Southern Hemisphere for 14 April 2001, respectively. The colored lines refer to: the CHAMP satellite cross track wind accelerometer measurements (brown); the simulation results obtained with the HWM07 model (black), the UAM model using the MFACE (red), the PM (blue), and the IPM (green).

In Figure 5.3, the small-scale fluctuations of the CHAMP accelerometer wind measurements are clearly visible in both panels. They are about ±50 m/s (during some polar overflight they are about ±100 m/s and even more). The satellite data and theoretical simulation results clearly show the areas of neutral wind vorticity cell as broader region of significant change of the wind component. The minimum wind values in these two examples are supposed to be the closed approaches to the respective vortex areas. All variants of the UAM model reproduce slightly different variations along the orbit trace, but with a similar position of the vortex. In the left panel, the position of the evening side vortex area is near 48600s UT. In the right panel, the circulation cell is clearly seen near 7800 s UT.

The global empirical HWM07 model shows a very smooth variation. It provides data with a significantly smaller magnitude range than the data obtained with the theoretical simulation results and the satellite measurements. The variance amplitude is more than three times smaller. The vortices areas are very shallow and their positions are barely identifiable.

Statistically, all models reproduce the CHAMP accelerometer measurements quite well with a similar mathematical expectation and standard deviation. Evidently, the UAM model reproduces the CHAMP data profile better than HWM07 model. The vortices' positions and magnitudes range of the theoretical simulations agree better with the satellite observations, while the empirical model reproduces only an average (smoothed) value of the CHAMP measurements.

5.4. Statistical comparison for the neutral mass density data

Another important parameter of the upper atmosphere presented in my study is the neutral mass density. The statistical analysis of the UAM and the NRLMSISE-00 models data and the CHAMP satellite accelerometer measurements of the neutral mass density was performed in the same manner as the analisis for the thermospheric neutral wind data. The results of the data comparison are presented below.
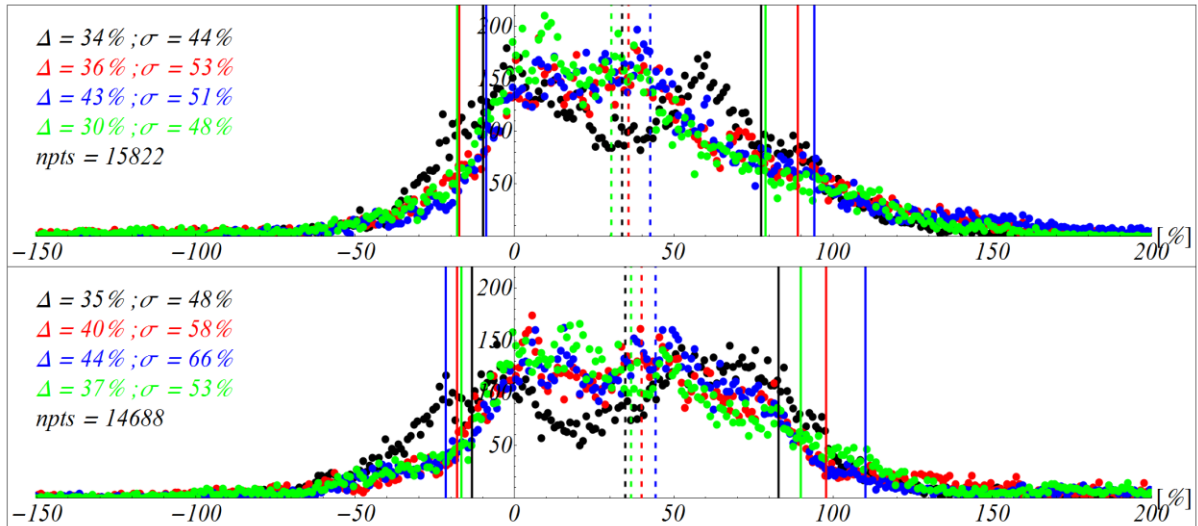
Figure 5.4. *The distributions of the differences between the models and the CHAMP measurements for the Northern (upper panel) and Southern (bottom panel) polar regions. Differences are shown for the empirical NRLMSISE-00 model (black), the UAM model using the MFACE (red), the PM (blue), and the IPM (green). The difference data are divided into intervals and integrated. The interval size is 2 %.*

As shown in Figure 5.4, all models represent a similar mathematical expectation and standard deviation for the Northern and Southern polar regions. The mathematical expectations are about 37% and the standard deviations are about 50 %.

The agreement between the model results and the satellite data are different for the Northern and Southern Hemispheres. The variation range for the Southern polar region is slightly larger than that for the Northern polar region (difference of a few %). This is a similar effect as seen in the thermospheric neutral wind data (see Figure 5.1). A probable origin of this effect was suggested above (see Section 5.3).

The significant offset of the average density values (mathematical expectation) between the modeling data and the satellite measurements is clearly visible. This means, according to Formulas 5.2 and 5.4, that the models reproduce larger neutral mass density values than do the

CHAMP measurements. Such an offset confirms the results of ***Doornbos, et al. [2010]*** which reveal that the CHAMP accelerometer neutral mass density measurements have a systematic difference to the NRLMSISE-00 model of about 15-25% (the observations show smaller values than the empirical model).
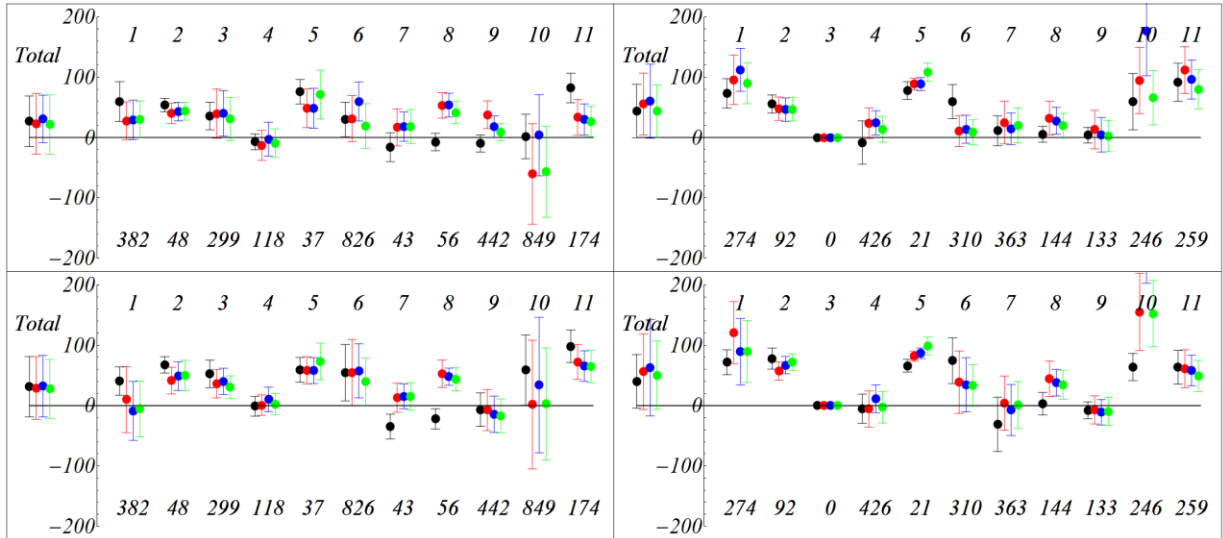
Figure 5.5. *The mathematical expectation (dots) ± standard deviation for all intervals in the Northern (upper panels) and Southern (bottom panels) polar regions and for both stable (left panels) and unstable (right panels) IMF conditions. The various colors represent the statistical parameters for the empirical NRLMSISE-00 model (black), the UAM model with the MFACE (red), the PM (blue) and the IPM (green). The average value of the AE index is mentioned at the bottom of each panels. Units are %.*

In Figure 5.5, the simulation results show a similar behavior. The dependence on the geomagnetic activity is not as obvious as in the case of the wind data (see Figure 5.2). The intervals could be divided into two groups: with a mathematical expectation near zero % (4, 7, 8, 9 and 10) and others (1, 2, 3, 5, 6 and 11). Such separation helps to explain the two maximums in Figure 5.4 which are quite obvious in the results from, for example, the NRLMSISE-00 model data (first maximum near 0, second near 70). The other models have similar profiles.

The statistical analyses of the UAM and the NRLMSISE-00 model data and the CHAMP neutral mass density measurements were carried out in the same manner as done for the thermospheric wind data. The results of the comparison are given in Table 5.2 below:

Date	Northern Hemisphere				Southern Hemisphere			
	Stable		Unstable		Stable		Unstable	
	Δ±σ, %	ntps	Δ±σ, %	ntps	Δ±σ, %	ntps	Δ±σ, %	ntps
14_ 04_ 2001	60±33 28±32 29±33 30±30	666	73±24 96±41 112±36 90±34	756	41±23 10±55 -9±49 -6±46	654	72±21 121±51 89±55 90±51	732
25_ 05_ 2002	54±11 40±17 43±15 44±15	660	56±15 48±19 46±20 47±20	744	68±13 41±22 49±24 50±25	744	78±18 57±15 67±14 72±14	642
18_ 11_ 2002	36±23 40±41 40±38 31±35	1428	No Data	0	53±23 36±23 40±22 31±19	840	No Data	0
01_ 02_ 2003	-7±13 -13±25 -3±28 -9±24	840	-8±36 24±25 24±20 14±22	570	-1±16 1±17 10±20 2±18	774	-5±24 -6±30 12±23 -3±26	642
23_ 10_ 2003	76±20 49±32 48±33 71±40	1296	78±15 89±10 89±11 108±15	186	59±20 58±22 58±22 73±30	1200	66±10 82±8 87±9 99±15	168
30_ 08_ 2004	30±29 31±38 60±32 19±37	822	59±28 11±26 14±23 9±21	660	54±47 55±55 58±45 40±39	822	74±38 39±52 35±45 33±34	558
13_ 09_ 2004	-16±24 17±31 18±24 18±28	1314	11±25 25±35 14±26 20±29	186	-35±20 13±24 15±21 15±23	1200	-31±45 4±45 -7±42 1±39	180
06_ 10_ 2004	-8±14 53±21 54±20 41±19	426	5±13 32±28 28±22 20±20	960	-22±17 53±23 48±14 44±19	534	3±19 44±29 38±22 35±24	858
10_ 12_ 2004	-10±14 38±23 18±18 9±14	642	4±13 13±32 5±29 2±26	756	-7±28 -8±34 -14±30 -17±28	732	-8±14 -7±23 -11±21 -10±23	642
13_ 06_ 2005	2±37 -60±83 4±67 -57±76	870	60±47 94±55 177±74 66±45	540	59±58 2±107 34±112 3±93	864	64±22 155±64 267±64 152±55	528
02_ 11_ 2006	82±25 33±30 30±26 27±25	492	92±32 112±39 96±32 80±32	1008	98±27 72±29 65±26 65±27	480	63±28 61±31 58±25 49±26	894
Total	27±42 22±50 31±39 22±49	**9456**	44±44 56±51 60±61 44±44	**6366**	31±50 29±52 32±51 28±49	**8844**	40±44 56±62 63±80 50±57	**5844**

Table 5.2. *The mathematical expectations and standard deviations for the thermospheric neutral wind data. The statistical parameters of the empirical NRLMSISE-00 model (black), the UAM model with the MFACE (red), the PM (blue), and the IPM (green).*

The data reveal a systematical offset. All models are producing values of the neutral mass density, which are larger than those obtained from the satellite observation by ~30%. The theoretical and empirical models show a different mathematical expectation and standard deviation from event to event but in general the behavior of the models is more or less the same. Models have smaller offsets for intervals with "stable" IMF orientations than for intervals with "unstable" IMF, in line with the case with wind data provided in Table 5.1. The difference between offsets and deviations for both hemispheres is about the same, with a slightly larger diference in the case for the Southern Hemisphere.

The total offset for the UAM model is ~ 25% (~55% for unstable cases) and the standard deviation is ~ 50%. Nonetheless, the deviation for single paths is smaller than the overall total. Single path's offsets are significantly different for various intervals. As a result, I have an artificial addition for the global standard deviation. This is clearly seen in Table 5.2 in the column for the Northern Hemisphere. The deviations for the NRLMSISE-00 model – for separate time intervals (days) are in the range of 11% - 37% while the total value amounts to 42%.
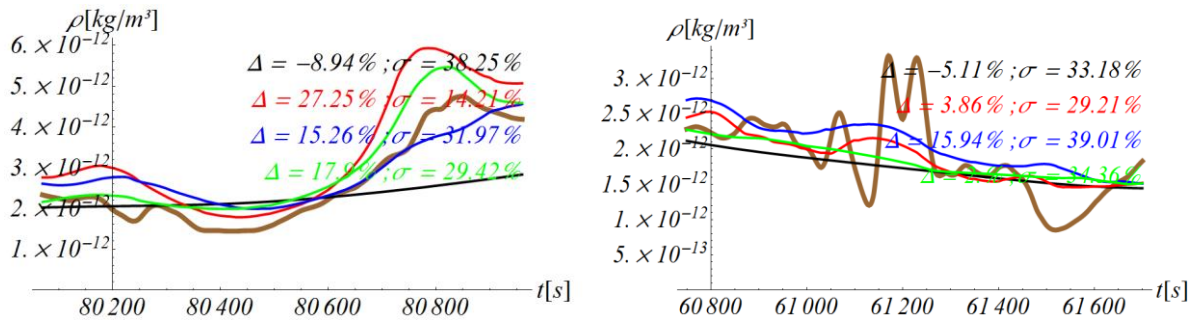
Figure 5.6. *Examples of two CHAMP paths over the polar regions. The left and right panels present the flight over the Northern (left panel) and Southern (right panel) Hemisphere for 1 February 2003. The colored lines means: the CHAMP cross-track wind accelerometer measurements (brown); the simulation results obtained with the NRLMSISE-00 model (black), the UAM model with the MFACE (red), the PM (blue), and the IPM (green).*

Figure 5.6. provides two examples of direct comparisons of neutral mass densities between the CHAMP observations and the models results for the polar cap areas. This way it might be easier to understand the real meanings of the values listed in Table 5.2.

The empirical model provides a very smooth neutral mass density variation along the orbit. All variants of the UAM model also have smooth profiles but they follow the observed variations to a certain degree. The theoretical model reproduces better satellite observations comparing to the NRLMSISE-00 model. In contrast to the visual appearance as exemplified in Figure 5.6, the statistical parameters of the empirical model (see Table 5.2) are similar or even better in some cases.

Like in the case with the thermospheric neutral wind data, the CHAMP accelerometer neutral mass density measurements contain significant fluctuations. Such fluctuations are clearly visible in the right panel of Figure 5.6. They are one of the sources of enhanced standard deviation values.

5.5. *The coordinate systems differences*

The problem lies in the difference in the coordinate systems of the UAM model versus satellite observations. The CHAMP satellite observations are provided in a geodetic coordinate system while in the UAM model the spherical geomagnetic and geomagnetic dipole coordinate systems are addlied. The satellite data as well as the simulation results should be presented in the same coordinate system for comparison. It is simple only at first sight, but the problem is more complex as I will illustrate in the exampling case (see Figure 5.7).

Processes in the upper atmosphere at high latitudes have a strong relation to geomagnetic coordinates. For example, the spatial distribution of the electric field is defined by the geometry of the magnetic field lines. The UAM model describes these processes in a simplified manner using an "ideal" dipole geometry. The CHAMP performs measurements in a real geomagnetic field. To study the MIT system, one should know the satellite position in an appropriate magnetic coordinate system. Ideally, one should refer to the real geomagnetic field configuration. It is common practice for high-latitude observations as, for example, with the SuperDARN radar network *[Ruohoniemi and Baker 1998]* to use the so-called Altitude Adjusted Corrected Geomagnetic (AACGM) coordinate system *[Baker et. al. 1989]*. I implemented it because it provides the best approximation of the real geomagnetic coordinate system. The AACGM has a more complicated structure than the "ideal" coordinate system, which is used in the UAM model. The difference is significant especially for the high-latitude region.
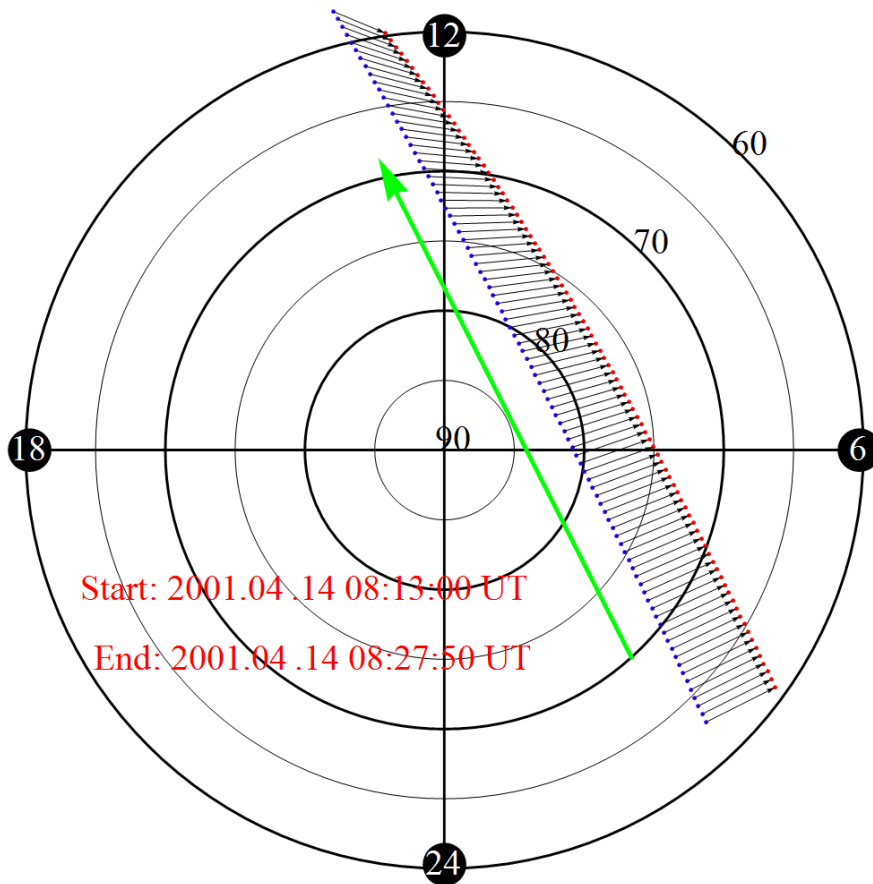
Figure 5.7. *An example of difference in coordinate transformation is shown in the figure above. It illustrates one CHAMP flight over the polar region (Northern Hemisphere). The blue dots show the direct transformation of satellite positions from the geodetic coordinate system to the geomagnetic coordinates (which are used in the UAM). The red dots represent the CHAMP path in the AACGM coordinate system (i.e. "real" geomagnetic coordinate system). The black arrows illustrate the offset between the coordinate systems. The green arrow shows the flight direction.*

Using the AACGM coordinate system helps us to link the satellite measurements with processes in the upper atmosphere and the magnetosphere. The difference between AACGM ("real") and the coordinate system of the UAM model ("ideal") is the source for an uncertainty during the comparison of modeling results with the satellite measurements.

In the future, I plan to improve the UAM model using the more realistic geomagnetic field and a correspondently coordinate system for the architecture. It will then reduce the uncertainty for data comparisons. However, the improvment of this model requires some more efforts and is thus beyond the scope of the present work.

5.6. Conclusion

All variants of the UAM model show the statistical results that are similar to the empirical HWM2007 and NRLMSISE00 model results. That is clearly seen from the thermospheric neutral wind data (see Figure 5.1) and the neutral mass density results (see Figure 5.4). Statistical parameters (standard deviation and mathematical expectation) are more or less the same for all models in general.

The statistical results are slightly different for various geomagnetic situations (see Figures 5.2 and 5.5). At the same time, the behavior of all models are relatively close to each other.

On the other hand, all variants of the UAM model reproduce the meso-scale structures of the polar area better than the empirical models. That is clearly visible in Figures 5.3 and 5.6 in which the direct comparisons between the modeling data and satellite measurements of the separate polar overflights are presented.

There is a significant difference between the CHAMP position in the UAM model coordinate system and the satellite position in the real Earth magnetic coordinate system (see Section 5.5 and Figure 5.7). Additionally, the CHAMP measurements contain some small-scale fluctuations (see for example Figure 5.6 a).

Taking into account all the facts described above, I conclude that statistically all variants of the UAM model have good agreement with the CHAMP satellite accelerometer measurements. The UAM model shows the similar statistical results as the empirical models. This is true also for the direct comparison: the same meso-scale structures as seen in the satellite observations. All variants can in principle be used for space weather prediction tasks, depending on the purpose of the simulation.

Summary

In my thesis, I investigated the dynamics of the coupled Magnetosphere – Ionosphere – Thermosphere (MIT) system with respect to the inner and outer influences. The study was performed using the Upper Atmosphere Model (UAM) (see Chapter 1). The particular attention of my work with the UAM model was centered on the high-latitudinal electrodynamics, e.g., by including the Interplanetary Magnetic Field (IMF) dependence of the external drivers.

In Chapters 2, 3 and 4 I described the evolution of the electric potential block development with respect to the strength and orientation of the IMF. I performed this development in three stages.

At the first stage (see Chapter 2), the IMF dependence was included into the UAM model by using the modified (with respect to the B_Y component of the IMF) pre-calculated electric field potential patterns (see Section 2.4.4). However, such a method supersedes the self-consistent calculation of the electric field in the modelling scheme. The electric field patterns are pre-calculated by means of the UAM model (standard version without the IMF dependence). I modified the pre-calculated electric field distributions with regard to the IMF dependence. The obtained result was used in the UAM model as input parameter. In my study, I tested this approach with various simulations of the time interval of October 28, 2003, 00-24 UT. The UAM model with modified electric field distributions (see Figures 2.13) provided a significant improvement in the agreement between the model prediction and the satellite measurements (see Figure 2.14).

At the second stage (see Chapter 3), the IMF dependence was included into the UAM model by using the Field Aligned Current (FAC) patterns obtained with the empirical IMF dependent FAC model of *Papitashvili et al. [2002]* (PM). Those FAC distributions were adapted with respect to the auroral precipitation area (see Section 3.4) and used as input parameters. At the same time, I used new assumptions (see Section 3.2) for the solution of the Poisson's equation (Equation 1.26). Such assumptions allowed me to obtain an appropriate relationship for the IMF orientation in order to incorporate the asymmetry of the electric field distribution between the Northern and Southern Hemispheres (see Figure 3.8). Here (in contrast with the first stage), the IMF dependent electric field distribution was calculated self-consistently as part of the UAM model.

At the third stage (see Chapter 4), I integrated the empirical high-resolution IMF dependent FAC model of *He et al. [2012]* (MFACE) into the UAM model. The MFACE model is advantageous in that it defines a two-dimensional magnetospheric FAC distribution in

dependence on various parameters of the solar wind (see Section 4.2). In the previous versions of the UAM model, the magnetospheric FAC system was defined along the inner and outer boundary lines of the auroral area. Additionally, the MFACE model was used to define the position of the auroral precipitation area (see Section 4.3.3). This version of the UAM model (with MFACE) with the assumption described in Section 4.3.4 allowed me to obtain the IMF dependent electric field distribution during the model run.

To verify the model prediction quality of the coupled MIT system, I tested the UAM model variants for various time intervals, which represent different seasons, geomagnetic and solar wind/IMF conditions (see Table 3.1). The obtained simulation results were compared with the CHAllenging Minisatellite Payload (CHAMP) observations (see Figures 3.9, 3.10, 3.12, 4.9, and 4.11) as well as with the global empirical Horizontal Wind Model 2007 (HWM07) and Naval Research Laboratory Mass Spectrometer and Incoherent Scatter Extended 2000 model (NRLMSISE00) (see Figures 4.10, 4.12, 5.3, and 5.6).

At the same time, I performed a statistical comparison of the thermospheric neutral wind and neutral mass density results (see Chapter 5). The IMF dependent versions of the UAM model show statistical results similar to those obtaned with the standard version of the UAM and the empirical HWM07 and NRLMSISE00 model results (see Tables 5.1 and 5.2). However, all variants of the UAM model reproduce the observed meso-scale structures of the polar area better than the empirical models (see Figures 5.3 and 5.6).

Various possible applications of the different UAM model variants are proposed as the followings:

The UAM with pre-calculated electric field potential patterns can be used for the modelling of the Earth's environment with specific geomagnetic conditions. With this method, any other physically realistic electric field can be used as input parameter during the run of the UAM model.

The combination of the UAM with the PM model presents a wider range of probable applications. For example, it can be used for the simulation of MIT dynamic coupling with respect to the IMF variation. At the same time, through this method which was used for the adaptation of the PM model to the UAM any other FAC distribution can be used as an input parameter for the UAM model. This variant, like the standatd variant (with empirical model of *Iijima and Potemra [1976]* (IPM)), can be realized on a rough spatial grid.

The configuration with the MFACE model provides an opportunity to use a high-resolution system of the FAC as input parameter for the UAM model. This variant can be used

for the investigation of particular events with a focus on high latitude physical processes. The UAM model with that FAC system needs a dense latitudinal spatial grid (with step less than 0.5 deg). That is necessary to keep the spatial features of the MFACE model.

At the further step of the development of the UAM model with respect to the simulation of the MIT dynamic coupled system, I would suggest the inclusion of a more realistic magnetic field geometry and IMF dependent auroral precipitation distributions. The more realistic magnetic field describes better the geometry of the high-latitudinal areas and helps to reduce such effect as, for example, the uncertainty in the comparison of the data for the model and the data from the measurements (see Section 5.5). The precipitation fluxes define the auroral areas with higher conductivity (see Section 1.7). An IMF dependent auroral precipitation distribution allows to obtain more realistic electric field distribution and, therefore, describes the high-latitudinal electrodynamics better. However, these tasks are beyond the scope of the present study and should be envisaged in further work with the UAM model.

References

Baker, K. B., and S. Wing (1989), A new magnetic coordinate system for conjugate studies at high latitudes, J. Geophys. Res., 94(a7), p. 9139, doi:10.1029/JA094iA07p09139.

Bilitza, D.: International Reference Ionosphere 2000, Radio Sci., 36(2), 261–275, 2001.

Brunelli, B. E., A. A. Namgaladze (1988), Fizika ionosfery. Nauka, Moscow (in Russian)

Doornbos, E., J. van den IJssel, H. Lühr, M. Förster and G. Koppenwallner (2010), Neutral density and crosswind determination from arbitrarily oriented multiaxis accelerometers on satellites. Journal of Spacecraft and Rockets, 47(4), 580-589, doi:10.2514/1.48114

Drob, D. P., J. T. Emmert, G. Crowley, J. M. Picone, G. G. Shepherd, W. Skinner, P. Hays, R. J. Niciejewski, M. Larsen, C. Y. She, J. W. Meriwether, G. Hernandez, M. J. Jarvis, D. P. Sipler, C. A. Tepley, M. S. O'Brien, J. R. Bowman, Q. Wu, Y. Murayama, S. Kawamura, I. M. Reid, and R. A. Vincent (2008), An empirical model of the Earth's horizontal wind fields: HWM07. J. Geophys. Res., Vol. 113, A12304, doi:10.1029/2008JA013668.

Eastwood, J. P. (2008), The science of space weather, Phil. Trans. R. Soc. A366, 4489–4500, doi:10.1098/rsta.2008.0161.

Förster, M.,Lühr, H., Reigber, C., Konig, R., Namgaladze, A. A., and Yurik, R. Y. (1999) The CHAMP satellite and its space weather monitoring capability, in: Proceedings of the 14th ESA Symposium on European Rocket and Balloon Programmes and Related Research, Noordwijk, Netherland, SP–437, 255–259

Förster, M., S. Rentz, W. Köhler, H. Liu, and S. E. Haaland (2008), IMF dependence of high-latitude thermospheric wind pattern derived from CHAMP cross-track measurements. Ann Geophys 26(N. 6):1581–1595

Förster, M., Y. I. Feldstein, S. E. Haaland, L. A. Dremukhina, L. I. Gromova, and A. E. Levitin (2009), Magnetospheric convection from cluster EDI measurements compared with the ground-based ionospheric convection model IZMEM. Ann Geophys 27, 3077–3087, doi:10.5194/angeo-27-3077-2009.

Förster, M., S. E. Haaland, and E. Doornbos (2011a), Thermospheric vorticity at high geomagnetic latitudes from CHAMP data and its IMF dependence. Ann. Geophys., 29, 181-186, doi:10.5194/angeo-29-181-2011.

Förster, M., A. A. Namgaladze, E. N. Doronina and B. E. Prokhorov (2011b), High-latitude thermospheric winds: Satellite data and model calculations. Khimicheskaya Fizika, Vol. 30, No. 5, 88–96, doi:10.1134/S1990793111030043.

Förster, M., B. E. Prokhorov, A. A. Namgaladze, and M. Holschneider (2012), Numerical modeling of solar wind influences on the dynamics of the high-latitude upper atmosphere. Adv. Radio Sci., 10, 299–312, doi:10.5194/ars-10-299-2012.

Haaland, S. E., G. Paschmann, M. Förster, J. M. Quinn, R. B. Torbert, C. E. McIlwain, H. Vaith, P. A. Puhl-Quinn, and C. A. Kletzing (2007), High-latitude plasma convection from cluster EDI measurements: method and IMF-dependence. Ann Geophys 25(N. 1):239–253

Hall, C. M., A. Brekke, O. V. Martynenko, and A. A. Namgaladze (1997), EISCAT measurements and model calculations of the turbulent energy dissipation in the high-latitude mesosphere. In: Abstracts of the VIII International EISCAT Workshop, Leicester, p.6.

Hardy, D. A., M. S. Gussenhoven, and E. Holeman (1985), A statistical model of auroral electron precipitation. J Geophys Res 90:4229–4248

He, M., J. Vogt, H. Lühr, E. Sorbalo, A. Blagau, G. Le, and G. Lu (2012), A high-resolution model of field-aligned currents through empirical orthogonal functions analysis (MFACE). Geophys. Res. Lett., Vol. 39, L18105, doi:10.1029/2012GL053168.

Hedin, A. E. (1987), MSIS-86 thermospheric model, J. Geophys. Res., 92, 4649–4662, doi:10.1029/JA092iA05p04649.

Hedin, A. E., N. W. Spencer, and T. L. Killeen (1988), Empirical global model of upper thermosphere winds based on Atmosphere and Dynamics Explorer satellite data, J. Geophys. Res., 93, 9959– 9978, doi:10.1029/JA093iA09p09959.

Hedin, A. E., et al. (1991), Revised global model of thermospheric winds using satellite and ground-based observations, J. Geophys. Res., 96, 7657–7688, doi:10.1029/91JA00251.

Hedin, A. E. (1991), Extension of the MSIS thermosphere model into the middle and lower atmosphere, J. Geophys. Res., 96, 1159–1172, doi:10.1029/90JA02125.

Hedin, A. E., et al. (1996), Empirical wind model for the upper, middle and lower atmosphere, J. Atmos. Terr. Phys., 58, 1421–1447, doi:10.1016/0021-9169(95)00122-0.

Iijima, T., and T. A. Potemra (1976), The amplitude distribution of field-aligned currents at northern high latitudes observed by Triad. J Geophys Res 81:2165–2174

Ivanov-Kholodny, G. S., and A. A. Nusinov (1987), Korotkovolnovoe izluchenie Solntza i ego vozdeistvie na verchnyuu atmospheru i ionospheru. Issledovaniya cosmicheskogo prostranstva (Investigations of Outer Space), vol 26. VINITI Press, Moscow (in Russian).

Klimenko, V. V., M. V. Klimenko, and V. V. Bryukhanov (2006), Numerical modeling of the electric field and zonal current in the Earth's ionosphere – statement of the problem and test calculations, Matem. Mod., 2006, Volume 18, Number 3, 77–92 (in Russian).

Liu, H., H. Lühr, and S. Watanabe (2007), Climatology of the equatorial thermospheric mass density anomaly, J. Geophys. Res., 112, A05305, doi:10.1029/2006JA012199.

Namgaladze, A. A., Yu. N. Korenkov, V. V. Klimenko, I. V. Karpov, F. S. Bessarab, V. A. Surotkin, T. A. Glushchenko, and N. M. Naumova (1988), Global model of the thermosphere-ionosphere-protonosphere system. Pure and Applied Geophysics. Vol. 127, No. 2/3, 219-254, doi:10.1007/BF00879812.

Namgaladze, A. A., Yu. N. Korenkov, V. V. Klimenko, I. V. Karpov, F. S. Bessarab, V. A. Surotkin, T. A. Glushchenko, and N. M. Naumova (1990), Global numerical model of the thermosphere, ionosphere, and protonosphere of the Earth. Geomagn. Aeronomy, Vol. 30, 612-619 (in Russian).

Namgaladze, A. A., Yu. N. Korenkov, V. V. Klimenko, I. V. Karpov, V. A. Surotkin, and N. M. Naumova (1991), Numerical modeling of the thermosphere-ionosphere-protonosphere system. J. Atmos. Terr. Phys., Vol. 53, No. 11/12, 1113-1124, doi:10.1016/0021-9169(91)90060-K.

Namgaladze, A. A., Yu. N. Korenkov, V. V. Klimenko, I. V. Karpov, V. A. Surotkin, F. S. Bessarab, and V. M. Smertin (1994), Numerical modelling of the global coupling processes in the near-earth space environment. COSPAR Coll. Ser., Vol. 5, 807-811.

Namgaladze, A. A., O. V. Martynenko, and A. N. Namgaladze (1995), Numerical simulation of substorm ionospheric variations observed by EISCAT by the use of the self-consistent ionosphere-thermosphere model including electric field calculations. In: Abstracts of the VII International EISCAT Workshop, Cargese, p.114.

Namgaladze, A. A., O. V. Martynenko, and A. N. Namgaladze (1995b), Global model of the upper atmosphere with variable latitudinal steps of numerical integration. In: Abstract of the IUGG XXI General Assembly, Boulder, GAB41F-6, B150, and (1996), Geomagn. Aeron. 36, 89–95 (in Russian).

Namgaladze, A. A., M. Förster, B. E. Prokhorov, and O. V. Zolotov (2013), Electromagnetic Drivers in the Upper Atmosphere: Observations and Modeling. Springer Netherlands, pp 165-219, doi:10.1007/978-94-007-2914-8_4.

Papitashvili, V. O., F. Christiansen, and T. Neubert (2002), A new model of field-aligned currents derived from high-precision satellite magnetic field data. Geophys. Res. Letters, Vol. 29, No. 14, 1683, doi:10.1029/2001GL014207.

Picone, J. M., A. E. Hedin, D. P. Drob, and A. C. Aikin (2002), NRLMSISE-00 empirical model of the atmosphere: Statistical comparisons and scientific issues J. Geophys. Res. A 107, 1468, doi:10.1029/2002JA009430.

Prokhorov, B. E., M. Förster, M. He, A. A. Namgaladze, and M. Holschneider (2014), Using MFACE as input in the UAM to specify the MIT dynamics, J. Geophys. Res., 119, 8, p. 6704-6714. doi:10.1002/2014JA019981

Ruohoniemi, J. M., and K. B. Baker (1998) Large-scale imaging of high-latitude convection with Super Dual Auroral Radar Network HF radar observations, J. Geophys. Res., 103, A9, p. 20797–20811. doi: 10.1029/98JA01288

Ruohoniemi, J. M., and R. A. Greenwald (2005) Dependencies of high-latitude plasma convection: Consideration of interplanetary magnetic field, seasonal, and universal time factors in statistical patterns, J. Geophys. Res., 110, 9204, doi:10.1029/2004JA010815.

Reigber, C., H. Lühr, and P. Schwintzer (2002), CHAMP mission status, Adv. Space Res., Vol. 30, 129–134.

Shim, J. S., M. Kuznetsova, L. Rastätter, D. Bilitza, M. Butala, M. Codrescu, B. A. Emery, B. Foster, T. J. Fuller-Rowell, J. Huba, A. J. Mannucci, X. Pi, A. Ridley, L. Scherliess, R. W. Schunk, J. J. Sojka, P. Stephens, D. C. Thompson, D. Weimer, L. Zhu, and E. Sutton (2012), CEDAR Electrodynamics Thermosphere Ionosphere (ETI) Challenge for systematic assessment of ionosphere/thermosphere models: Electron density, neutral density, NmF2, and hmF2 using space based observations. Space weather, vol. 10, S10004, doi:10.1029/2012SW000851,.

Volkov, M. A., and A. A. Namgaladze (1996), Model calculations of the field-aligned currents and electric fields during the substorm expansion phase. Geomagn. Aeronomy, Vol. 36, 438-444. (in Russian).

Acknowledgment